Feasibility studies of a polarized positron source based on the bremsstrahlung of polarized electrons

Jonathan Dumas

UNIVERSITÉ DE GRENOBLE

THÈSE

Pour obtenir le grade de

DOCTEUR DE L'UNIVERSITÉ DE GRENOBLE

Spécialité : **Physique Subatomique & Astroparticules**

Arrêté ministériel : 7 août 2006

Présentée par

Jonathan DUMAS

Thèse dirigée par **Eric Voutier** et
codirigée par **Joseph Grames**

préparée au sein du **Laboratoire de Physique Subatomique et de Cosmologie / Jefferson Lab**
dans **l'École Doctorale de Physique de Grenoble**

Etudes de la faisabilité d'une source de positrons polarisée basée sur le bremsstrahlung d'un faisceau d'électrons polarisé

Thèse soutenue publiquement le **22 Septembre 2011**,
devant le jury composé de :

Mr, Jean-Marie, DE CONTO
Professeur à l'Université Joseph Fourier, Président
Mr, Arne, FREYBERGER
Physicien au Thomas Jefferson National Accelerator Facility, Rapporteur
Mr, Joseph, GRAMES
Physicien au Thomas Jefferson National Accelerator Facility, Membre
Mme, Egle, TOMASI GUSTAFSSON
Physicienne à l'Institut de Physique Nucléaire d'Orsay, Membre
Mr, Alessandro, VARIOLA
Physicien au Laboratoire de l'Accélérateur Linéaire, Rapporteur
Mr, Eric, VOUTIER
Physicien au Laboratoire Physique Subatomique Cosmologie, Membre

Acknowledgements

First, I would like to thank my advisors, Eric Voutier and Joe Grames, it always has been a pleasure and privilege to learn from their knowledge. They relentlessly kept me on track for getting this thesis done.

I am thankful to the PEPPo team for making the experiment possible.

I would like to thank the Grenoble, Geneva, JLab gangs and everyone with a couch I crashed on, it wouldn't have been as fun without them.

Finally, I am grateful to my family for its unconditional support.

Résumé

Les communautés de la physique nucléaire et des hautes énergies ont montré un intérêt croissant pour les faisceaux de positrons intenses et hautement polarisés. Des photons polarisés durs peuvent produire des positrons dans le champ atomique par création de paire, l'électron et le positron ainsi produits portent une partie de la polarisation de la particule initiale. Les récentes avancées dans le domaine des sources d'électrons à courants intenses (1 mA) et hautement polarisés au Jefferson Lab offrent la perspective de créer des positrons polarisés à partir d'électrons de faible énergie. Cette thèse se propose de discuter les transferts de polarisation aux positrons dans la perspective d'une optimisation du design d'une source de positron polarisée. L'expérience PEPPo, visant à mesurer la polarisation de positrons par un faisceau d'électrons de basse énergie ($<$10MeV) mais de basse intensité est discutée. Une démonstration concluante de cette technique fournirait une méthode alternative de produire des positrons polarisés de basse énergie et des informations utiles pour optimiser le design d'une source dans la gamme d'énergie inférieure au GeV.

Abstract

The nuclear and high-energy physics communities have shown a growing interest in the availability of high current, highly-polarized positron beams. A sufficiently energetic polarized photon or lepton incident on a target may generate, via bremsstrahlung and pair creation within a solid target foil, electron-positron pairs that should carry some fraction of the initial polarization. Recent advances in high current (> 1 mA) spin polarized electron sources at Jefferson Lab offer the perspective of creating polarized positrons from a low energy electron beam. This thesis discusses polarization transfer from electrons to positrons in the perspective of the design optimization of a polarized positron source. The PEPPo experiment, aiming at a measurement of the positron polarization from a low energy (< 10 MeV) highly spin polarized electron beam is discussed. A successful demonstration of this technique would provide an alternative scheme for the production of low energy polarized positrons and useful information for the optimization of the design of polarized positron sources in the sub-GeV energy range.

Contents

Introduction

In 1928, Paul Dirac proposed from mathematical intuition that matter and in particular electrons could have a mirror image of themselves [1]. Based on the binomial equation of relativistic mechanics, establishing the equivalence between the electron mass m and its total energy E

$$E^2 = m^2c^4 + p^2c^2 \tag{1}$$

where p is the electron momentum and c the speed of light, Dirac noticed that only one of the two mathematical solutions was considered to be physically possible. The idea of electron energies with quantities greater than mc^2 or lower than $-mc^2$ led to the prediction of positrons. In practice, the energy is always positive, a negative energy state electron is not observable. However, it suggests that in the Dirac sea where vacuum is represented as an infinite number of negative energy state electrons, a defection or a vacancy can be interpreted as a hole in the negative energy electron field. This electron-size hole could be observable, acting like any positive energy state electron, with the same mass and properties except for its charge. This establishes a first connection between the mathematical negative energies interpretation and the positrons.

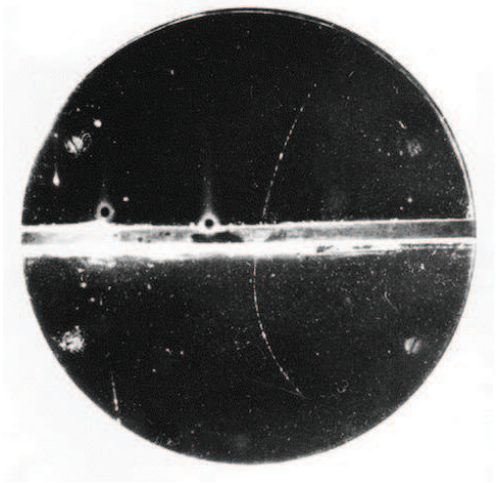

Figure 1: Cloud chamber photograph of the first positron identified by C.D. Anderson [2]. The particle curvature, more accentuated on the upper half of the picture indicating a lower energy, suggests that the positron must have come from below.

The identification of positrons were found by Carl Anderson in 1932 [2], studying the cosmic radiation passing through a cloud chamber and a lead plate. The tracks

left on photographic plates are showing curvatures due to a magnetic field. The tracks correspond to particles with the electron mass except that the directions reveal positive charges.

In addition to the important role positrons play in material science or medical scanning technology, they also serve a critical parameter in nuclear or high energy physics experiments. The resultant asymmetry of successively colliding both electrons and positrons can be used to disentangle their interaction with matter. Information on their energy, kinematics and quantum states both before and after their interaction precisely describe the physics of interest, yet depend also on the sign of their charge.

Another critical parameter is the polarization of the electrons or positrons, corresponding to the spin alignment of the particles forming the beam. By using polarized electrons and polarized positrons experiments may simultaneously explore both dependence on lepton charge and spin. Leptons may achieve a high degrees of polarization ($> 90\%$) via the Sokolov-Ternov effect [3]. Spontaneous emission of synchrotron radiation preferentially precesses the spin parallel/anti-parallel to the bending dipole field. However for this to be effective the beam must have a long time to self-polarize as is possible in a storage ring. This of course is prohibitive when the integrated bending field (storage time) is simply too small as found in a high energy linear collider or accelerator. Ideally a spin polarized source is desired. In the case of the electron accelerators the predominant method used is based upon the optical pumping and photoemission of electron from III-V semiconductor gallium arsenide (GaAs) using circularly polarized laser light. The first optical pumping electron source for accelerators was used at SLAC (1975) [4] where the polarization was limited to $\sim 35\%$, using a bulk GaAs semiconductor. The application of a layer of an activated GaAs doped with Phosphorus (strained GaAs) makes a perturbation in the crystalline symmetry allowing the circular polarization of the laser light to extract only electrons spin-aligned representing a theoretical polarization of 100%. In practice though, with a single layer of strained GaAs, polarizations of 75% are achieved because of the depolarization of the electrons due to the multiple scattering in the semiconductor before extraction, the deeper the electrons come from in the GaAs the higher the depolarization. Recent advances in photocathodes made polarizations of 85% possible thanks to the so-called "superlattice" GaAs which consists of alternating layers of GaAs and GaAsP, limiting the effects of the depolarization in the GaAs semiconductor.

Positron beams with high polarization are similarly desired. This has been the recent topic of extensive research and experiments in the context of the International Linear Collider. The successful measurements of highly polarized positrons ($> 80\%$) have been produced using unpolarized electron beams of very high energy ($>$ tenths of GeV). This thesis proposes a novel scheme to produce positrons with a similarly high degree of polarization by using polarized electrons beam of low energy < 10 MeV. The feasibility of this scheme depends upon measurement of the polarization transfer from the polarized electron beam to the resulting positrons. This is the subject of this thesis.

In chapter one, the motivations why polarized positrons constitute a valid interest for nuclear and accelerator physics at JLab are described. The second chapter reviews the elementary processes for polarized positron production and how it can

be applied for an actual source suitable for an accelerator. The simulations for a conceptual design of a possible experiment based on the available instruments are shown in the third chapter. In the last chapter will be presented the developement and the construction of the polarimeter intended for the characterization of the positrons produced in the proposed Polarized Electrons for Polarized Positrons (PEPPo) project.

Chapter 1

Polarized positrons at JLab

1 Introduction

Polarized and unpolarized positron beams are complementary and essential tools for the understanding of numerous physics phenomena ranging from high energy physics to solid state physics (see ref. [5] for an overview). In the context of the hadronic physics program worked out at the Jefferson Laboratory (JLab), the comparison between electron and positron scattering is not only an additional source of information but also a mandatory step for an unambiguous extraction of the physics quantities of interest. Particularly, the accurate investigation of the partonic structure of nucleons and nuclei require both high energy polarized positron and polarized electron beams. The production of polarized positrons has been explored both via the weak and the electromagnetic interactions.

The natural decay of some radio-isotopes, such as $^{22}\mathrm{Na} \rightarrow {}^{22}\mathrm{Ne}{+}e^{+}{+}\nu_e$, generate positrons with polarization as large as 40 % [6], consequently to the parity non-conservation of the β^{+}-decay. The emitted positron flux is however not well-suited for transmission in accelerating cavities.

At accelerator facilities, a common method used is pair production via the conversion of photons into $e^{-}e^{+}$ pairs within the nuclear field of a nucleus (Fig. 1.1). The photon energy must be larger than the rest mass of the pair, 1.022 MeV. A conversion target with a high atomic number Z is generally preferred to increase the electromagnetic shower generation.
Unpolarized positrons like electrons will self-polarize in a storage ring due to the Sokolov-Ternov effect [3]. The interactions of leptons with a dipole field result, via the emission of synchrotron radiation, in asymmetrical alignement of spin parallel or anti-parallel to the magnetic field. The polarization builds up over time t to reach the limit $P_{max}(1 - e^{-t/\tau})$ where P_{max} is the equilibrium polarization (92.24 % assuming no depolarization effects) derived from quantum electrodynamics [7], and τ is the polarization build-up time. It depends on the positron energy through the Lorentz factor γ and the ring bending radius R,

$$\tau^{-1} = \left(\frac{5\sqrt{3}}{8} \frac{\hbar r_e}{m_e} \right) \frac{\gamma^5}{R^3}\,, \tag{1.1}$$

where $\hbar$ is the Planck constant, r_e and m_e are respectively the classical radius and rest mass of the electron.

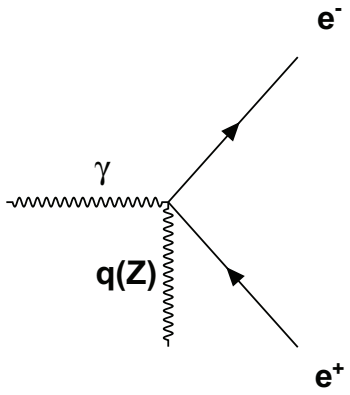

Figure 1.1: Feynman diagram for the pair creation process: a gamma ray interacts with a virtual photon of the nuclear Coulomb field.

Self-polarization is a slow process, lasting several minutes up to hours (Tab. 1.1). Moreover it suggests the construction of a large scale storage ring. In the Continuous Electron Beam Accelerator Facility (CEBAF), a typical bending radius of the dipoles is 30 meters, based on the electron beam sections including these dipoles (Arcs), requires a ring with a circumference of 560 meters. A 6 GeV positron beam would have a build up time of 6 minutes. Alternatively, one may transfer polarization from photons to positrons [8], the challenge being the production of an intense flux of sufficiently energetic photons with a high degree of circular polarization.

Ring	**Energy (GeV)**	**Circumference (m)**	**R (m)**	τ **(min)**
CESR [9]	5.30	768.4	88.00	268
HERA [10, 11]	27.5	6336	608.1	23.5
LEP [12]	45	26670	3096	265

Table 1.1: characteristics of some storage rings.

This chapter reviews some of the physics cases that motivated the present work as part of a broad nuclear physics program achievable at JLab [5]. Two experimentally demonstrated methods for polarized positron production are described and the new method proposed in this thesis will be discussed in the next chapters.

2 Physics motivations

2.1 Electron elastic scattering

2.1.1 Nucleon electromagnetic form factors

The elastic scattering of an electron beam off a proton target is the most simple process for the study of the internal structure of the proton. In the reaction $e(k) + P(p) \rightarrow e(k') + P(p')$, shown in Fig. 1.2, the squared four-momentum transfer of the virtual photon $q^2 = (k - k')^2 = (p' - p)^2$ characterizes the transverse size of the

probed internal region of the proton. The vertex γP is described by the electric (G_E) and magnetic (G_M) form factors, function of the momentum transfer Q^2 only. The electromagnetic form factors are consequently depending only on q^2. Within a non-relativistic approach, these quantities can be interpreted as the Fourier transforms of the charge and magnetization densities of the proton [13].

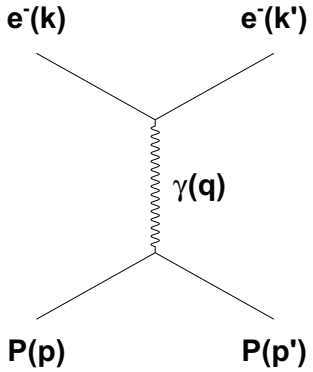

Figure 1.2: Lowest order (QED) diagram of the elastic eP reaction; the initial and final electron mometum four-vectors are k and k', respectively, and p and p' for the proton; the four-momentum transfer to the photon is q.

In the Born approximation (one photon exchange), the scattering amplitude $\mathcal{M}$ is defined by the interaction of the electromagnetic ($J^{\nu,e}$) and hadronic ($J^{\mu,P}$) currents as

$$\mathcal{M} = \underbrace{\overline{u}(k')e\gamma^{\mu}u(k)}_{J^{\nu,e}} \frac{eg_{\mu\nu}}{q^2} \underbrace{\overline{u}(p')\left[G_M\gamma^{\mu} + \frac{G_E - G_M}{2M(1+\tau)}(p+p')^{\mu}\right]u(p)}_{J^{\mu,P}} \tag{1.2}$$

where u is the electron spinor, $2g^{\mu\nu} = \{\gamma^{\mu}, \gamma^{\nu}\}$ is the Minkowski metric tensor, M is the proton mass, and $\tau = -q^2/4M^2$. The proton electromagnetic form factors can be experimentally measured through different observables that are expressed in terms of the scattering amplitude (Eq. 1.2).

2.1.2 Experimental observables

The electromagnetic form factors G_M and G_E can be obtained from unpolarized and polarized experimental observables.

For unpolarized beam and target, the form factors are extracted from the unpolarized cross section following the so-called Rosenbluth separation. For a given range of energy, the cross section for the unpolarized elastic process, first derived by M.N. Rosenbluth [14], is function of the four-momentum transfer and the electron scattering angle (θ_e), and energy (E,$E\prime$)

$$\frac{d\sigma}{d\Omega_e} = kf_{rec}\left(\frac{d\sigma}{d\Omega_e}\right)_{Mott}\sigma_R = kf_{rec}\left(\frac{d\sigma}{d\Omega_e}\right)_{Mott}\left[G_M^2 + \frac{\epsilon}{\tau}G_E^2\right] \tag{1.3}$$

where $k = 1/\left[\epsilon\tau(1+\tau)\right]$ is a kinematical factor, $f_{rec} = E'/E$ is the recoil correction factor, and

$$\epsilon = \left[1 + 2(1+\tau)\tan^2(\theta_e/2)\right]^{-1} \tag{1.4}$$

is the longitudinal polarization degree of the virtual photon. The Mott cross section $(d\sigma/d\Omega)_{Mott}$ represents the elastic electron scattering off a point-like particle, and the reduced cross section σ_R is the quantity of interest which contains the internal structure of the nucleon. The form factors are separated taking advantage of the linear ϵ-dependence of σ_R: the magnetic form fator is measured at large scattering angles ($\theta_e \sim 180°$) where G_M dominates σ_R, and the electric form factor is extracted from a measurement at small scattering angles ($\theta_e \sim 0°$) keeping τ (or q^2) constant for a variation of the beam energy.

The polarization transfer from the electron beam to the recoil proton in the reaction $\vec{e}p \to e\vec{p}$ offers an alternative determination of the electric form factor [15, 16]. In this process, the transverse polarization in the reaction plane (P_t) and longitudinal (P_l) polarization of the recoil proton are given by

$$P_t = -\frac{P_b}{\sigma_R}\sqrt{\frac{2\epsilon(1-\epsilon)}{\tau}}\,G_E G_M \tag{1.5}$$

$$P_l = \frac{P_b}{\sigma_R}\sqrt{1-\epsilon^2}\,G_M^2 \tag{1.6}$$

where P_b is the electron beam polarization. The ratio of the polarization component yields a unique determination of the form factors ratio

$$\frac{G_E}{G_M} = -\sqrt{\frac{\tau(1+\epsilon)}{2\epsilon}}\,\frac{P_t}{P_l} \tag{1.7}$$

which, combined with the simultaneous measurement of the reduced cross section, allows for a new separation of the electromagnetic form factors.

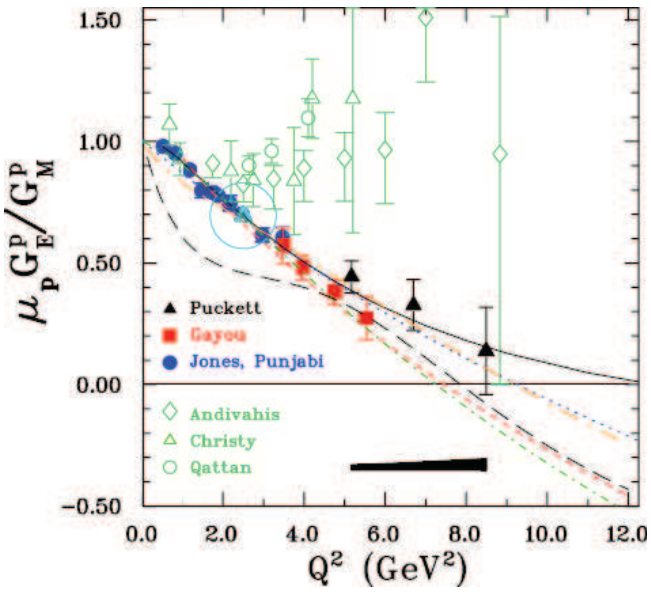

Figure 1.3: Most recent experimental data on the electromagnetic form factor ratio as measured from polarization transfer (in blue, black and red) [17–19] and Rosenbluth separation (in green) [20–22] experiments (from Ref. [19]).

This ratio has been extensively studied using the methods described previously, the Rosenbluth separation gives access to the squared ratio, therefore the relative

sign of the form factors remains unknown, as opposed to the polarization method. The most recent data are shown on Fig. 1.3 where a striking discrepancy between the two techniques is revealed and has been confirmed over the past years. These disagreements generated controversy and it was suggested that they may originate from higher order mechanisms beyond the Born approximation. The exchange of two photons in the *ep* reaction was shown to possibly reconcile, at least partly, the Rosenbluth separation and the polarization transfer techniques [24].

Indeed, the 2γ-exchange process brings corrections to the form factors and to the experimental observables. The internal structure of the proton is no longer represented by two but five form factors

$$\widetilde{G}_M = -e_b G_M + \delta\widetilde{G}_M \tag{1.8}$$
$$\widetilde{G}_E = -e_b G_E + \delta\widetilde{G}_E \tag{1.9}$$
$$\widetilde{F}_3 = \delta\widetilde{F}_3 \tag{1.10}$$

where e_b stands for the sign of the lepton beam charge. The modified experimental observables given by [24]

$$\sigma_R = G_M^2 + \frac{\epsilon}{\tau}G_E^2 - 2e_b\, G_M\, \Re\Big[\delta\widetilde{G}_{M,1}\Big] - 2e_b\, \frac{\epsilon}{\tau}G_E\, \Re\Big[\delta\widetilde{G}_{E,1}\Big] \tag{1.11}$$
$$P_t = -\frac{P_b}{\sigma_R}\sqrt{\frac{2\epsilon(1-\epsilon)}{\tau}}\left(G_E G_M - e_b\, G_E \Re[\delta\widetilde{G}_M] - e_b\, G_M \Re\left[\delta\widetilde{G}_{E,1}\right]\right) \tag{1.12}$$
$$P_l = \frac{P_b}{\sigma_R}\sqrt{1-\epsilon^2}\left(G_M^2 - 2e_b\, G_M \Re\left[\delta\widetilde{G}_{M,2}\right]\right) \tag{1.13}$$

with

$$\delta\widetilde{G}_{M,1} = \delta\widetilde{G}_M + \epsilon\frac{\nu}{M^2}\widetilde{F}_3 \tag{1.14}$$
$$\delta\widetilde{G}_{E,1} = \delta\widetilde{G}_E + \frac{\nu}{M^2}\widetilde{F}_3 \tag{1.15}$$
$$\delta\widetilde{G}_{M,2} = \delta\widetilde{G}_M + \frac{\epsilon}{1+\epsilon}\,\frac{\nu}{M^2}\widetilde{F}_3 \tag{1.16}$$
$$\nu = \frac{p+p'}{2}.\frac{k+k'}{2}\,. \tag{1.17}$$

The real part of the form factors can be extracted from 3 T-odd or 5 T-even observables with polarized electrons at the cost of long measurements [25]. The individual determination of the Born terms and the 2γ-exchange corrections requires a set of five different measurements. Polarized electrons and polarized positrons provide six independent observables (σ_R, P_T, P_L) which allow for a complete model independent extraction of these quantities.

2.2 Deeply virtual Compton scattering

2.2.1 Generalized parton distributions

Quantum chromodynamics (QCD) describe the quark and gluon dynamics inside partonic matter. The electromagnetic form factors studied in elastic scattering give information about the electric and magnetic distributions of the nucleons, however

the inner structure is not resolved. Generalized parton distributions (GPDs) [26–29] link these distributions with the inner content of the nucleons. They represent a multi-dimensional generalization of the usual parton distributions measured in deep inelastic scattering (DIS). GPDs can be interpreted [30,31], at any given scale controlled by $1/q^2$, as the distribution in the transverse plane of partons carrying a given longitudinal momentum fraction x of the nucleon momentum†. They parametrize the partonic structure of the nucleon in terms of correlations between quarks, antiquarks and gluons, and therefore contain information about the dynamics of this system.

2.2.2 Experimental observables

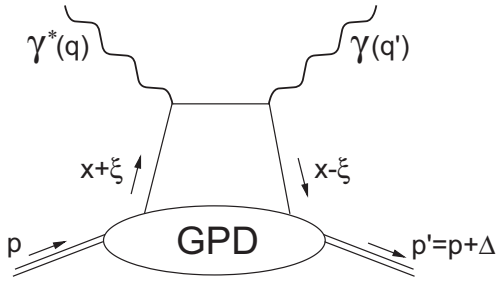

Figure 1.4: Lowest order (QCD) amplitude, the so-called handbag diagram, for the virtual Compton process ($\gamma^* p \rightarrow \gamma p$); the momentum four-vectors of the incident and scattered photon are q and q', and p and p' for the proton, respectively; the four-momentum transfer to the nucleon is Δ=$(p'-p)$=$(q-q')$.

GPDs are accessed via Compton form factors measured in deeply virtual Compton scattering (DVCS) experiments within the specific kinematic region (Bjorken regime) where the interaction takes place with point-like constituents. The DVCS reaction ($\gamma^* p \rightarrow \gamma p$), where virtual photons are produced by a lepton beam, is the simplest exclusive process (fig. 1.4) for the determination of GPDs.

The production of photons from electrons ($ep \rightarrow ep\gamma$) is described by two main amplitudes (Fig. 1.5):

- the Bethe-Heitler process (BH) in which the real photon is created by the electron before or after the interaction with the nucleon
- the DVCS process where the absorption of the virtual photon by a quark is followed quasi-instantaneously by the emission of a real photon.

These processes cannot be distinguished; furthermore their interference (INT) contributes to the cross section

$$\sigma(ep \rightarrow ep\gamma) = \sigma_{BH} + \sigma_{DVCS} + P_b \widetilde{\sigma}_{DVCS} + e_b \sigma_{INT} + P_b e_b \widetilde{\sigma}_{INT} \qquad (1.18)$$

where the σ ($\widetilde{\sigma}$)'s are even (odd) functions of the out-of-plane angle between the leptonic (initial and final electron) and hadronic planes (recoil proton and real photon). The BH cross section is calculable in QED from the electromagnetic form factors.

†Here, longitudinal and transverse are defined with respect to the direction of the virtual photon.

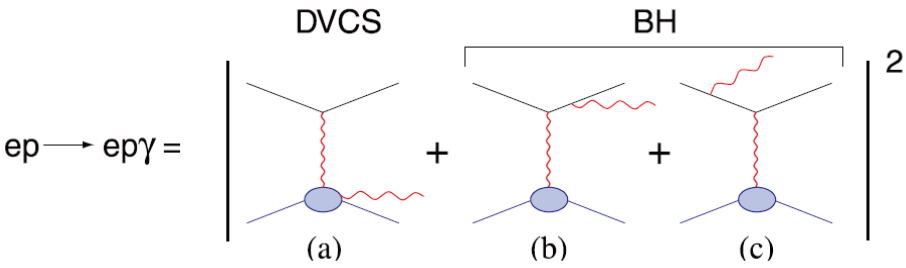

Figure 1.5: DVCS (a) and BH contributions (b and c) to $ep \to ep\gamma$.

The pure DVCS and interference contributions contain the information of interest, particularly σ_{INT} ($\widetilde{\sigma}_{INT}$) which is proportional to the real (imaginary) part of the interference amplitude. σ_{INT} ($\widetilde{\sigma}_{INT}$ depends linearly on GPDs. Knowledge of the full set of the unknown amplitudes participating in the cross section is required to separate the different GPDs [33, 34]. The observables accessible to a (un)polarized electron beam are

$$\sigma^0(e^-) = \sigma_{BH} + \sigma_{DVCS} - \sigma_{INT} \quad (1.19)$$

$$\sigma^+(e^-) - \sigma^-(e^-) = 2P_b\,\widetilde{\sigma}_{DVCS} - 2P_b\,\widetilde{\sigma}_{INT} \quad (1.20)$$

where the upper index denotes the polarization state of the beam. Separating further the DVCS and INT contributions requires additional measurements at different beam energies within a Rosenbluth like procedure [35], which is however known to be limited from the elastic electron scattering case (see previous section). The unique determination of each single contribution to the reaction cross section is obtained from the combination of polarized electron and polarized positron measurements following

$$2\,\sigma_{BH} + 2\,\sigma_{DVCS} = \sigma^0(e^+) + \sigma^0(e^-) \quad (1.21)$$

$$2\,\sigma_{INT} = \sigma^0(e^+) - \sigma^0(e^-) \quad (1.22)$$

$$4P_b\,\widetilde{\sigma}_{DVCS} = \left[\sigma^+(e^+) - \sigma^-(e^+)\right] + \left[\sigma^+(e^-) - \sigma^-(e^-)\right] \quad (1.23)$$

$$4P_b\,\widetilde{\sigma}_{INT} = \left[\sigma^+(e^+) - \sigma^+(e^-)\right] - \left[\sigma^-(e^+) - \sigma^-(e^-)\right]\,. \quad (1.24)$$

Similarly to electron elastic scattering, the separation of the four unknown amplitudes contributing to the photon electroproduction process requires four independent observables that are uniquely obtained from polarized electron and polarized positron measurements.

3 Polarized positron production

Apart from radioactive sources which are not considered here, polarized positron sources rely on the production of polarized photons with energies above the e^-e^+ pair creation threshold (1.022 MeV). This section describes two different schemes for photon production, developed in the context of the International Linear Collider (ILC) project. Both have been recently demonstrated in dedicated experiments.

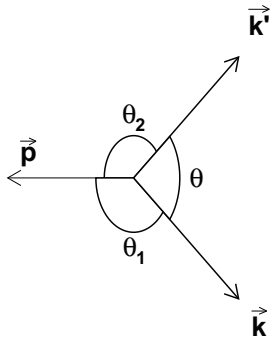

Figure 1.6: Compton scattering reaction where θ_1 and θ_2 are respectively, the photon incident angle and scattering angle in the electron frame (supported by $\vec{p}$).

3.1 Backward Compton scattering

3.1.1 Principle of operation

Photons can be completely right (R) or left-handed (L) circularly polarized, but are however not energetic enough to create e^+e^- pairs. The scattering of photons (Fig. 1.6) with energy k_0 off a high energy E electron beam (Lorentz factor $\gamma \gg 1$) brings the missing piece to make energetic γ-rays and conserves some of the laser photon circular polarization [36]. In this Compton process, the scattered photon energy becomes

$$k' = k_0 \frac{(1 - \beta\cos(\theta_1))}{(1 - \beta\cos(\theta_2)) + (k_0/E)(1 - \cos(\theta))} \tag{1.25}$$

with β the electron velocity in units of the speed of light (c) and the electron mass (m). k' is maximized for a head on collision $\theta_1 \simeq 180°$ and forward scattering angles $\theta_2 \simeq 0°$. Neglecting the very weak dependence upon θ_1 in these conditions, the Compton edge corresponding to the maximum energy is given by

$$k_{max} = E\frac{z}{1+z} \tag{1.26}$$

where the reduced energy variable is

$$z = 4\,\frac{Ek_0}{m^2c^4}\,. \tag{1.27}$$

Accordingly, the production of γ-rays above the pair production threshold ($2m$) from a 1 eV laser scattering off of an electron beam with energies larger than 280 MeV (Fig. 1.7).

The spectral shape of the photons produced in a Compton scattering process may be written [37]

$$\frac{d\sigma}{dk} = \frac{2\pi r_e^2 a}{k_{max}}\,\left[\chi + 1 + \cos^2(\alpha)\right] \tag{1.28}$$

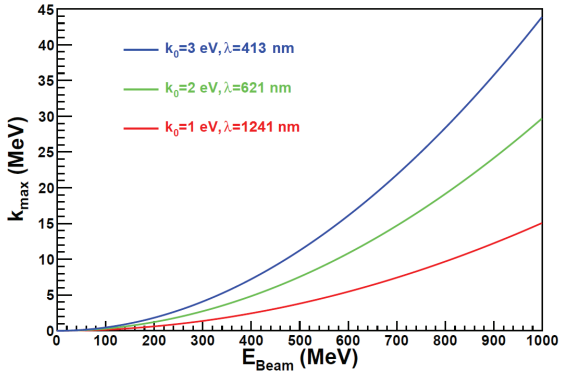

Figure 1.7: Compton edge (k_{max}) as a function of the electron beam energy (E_{beam}) considering common laser light.

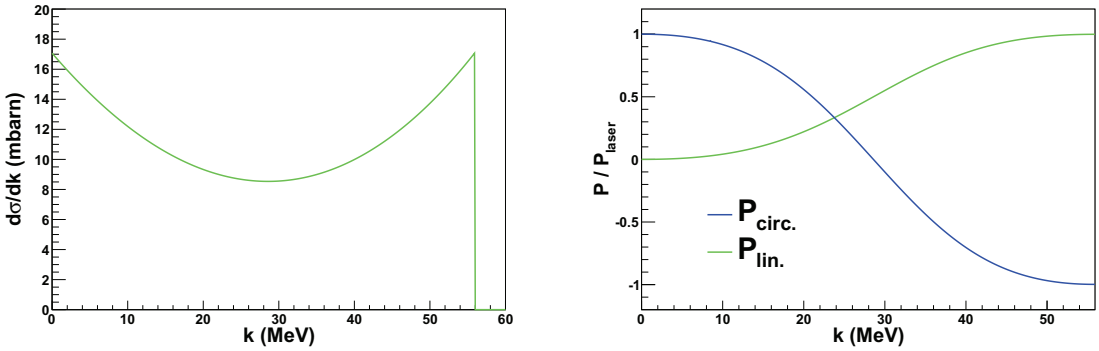

Figure 1.8: Differential Compton scattering cross section (left), Circular $P_{circ.}$ and linear $P_{lin.}$ polarization (right) of γ-rays produced by a 532 nm laser wavelength scattering off 1.28 GeV electrons as a function of the γ-ray energy (k).

where r_e is the classical electron radius, with the following parameters

$$a = \frac{1}{1+z}, \qquad \rho = \frac{k}{k_{max}}, \qquad \chi = \frac{\rho^2(1-a^2)}{1-\rho(1-a)}, \quad \cos(\alpha) = \frac{1-\rho(1+a)}{1-\rho(1-a)}. \tag{1.29}$$

The circular (P_{circ}/P_{laser}) and linear (P_{lin}/P_{laser}) polarization transfer degrees write

$$\frac{P_{circ}}{P_{laser}} = \frac{(2+\chi)\,\cos(\alpha)}{(\chi+1+\cos^2(\alpha))} \tag{1.30}$$

$$\frac{P_{lin}}{P_{laser}} = \frac{(1-cos(\alpha))^2}{2\,(\chi+1+cos^2(\alpha))}\,. \tag{1.31}$$

The differential Compton cross section (Eq. 1.28) and the polarization transfers (Eq. 1.30 and 1.31) are represented in Fig. 1.11 for a 532 nm laser wavelength and a 1.28 GeV electron beam as used for a KEK-ATF experiment [38]: the photon energy distribution shows that large polarization transfers, both circular and linear, are most likely obtained at high photon energies.

3.1.2 The KEK-ATF experiment

Parameters	Laser photons	Electron beam
Energy	2.33 eV	1.28 GeV
Particles/bunch	avg. 1.25×10^{18}	1.8×10^{10}
Bunch length	110 ps	31 ps

Table 1.2: Laser and electron beam characteristics of the KEK-ATF experiment [40].

An experiment [38] at the KEK-ATF facility was conducted to demonstrate the positron performances of the Compton back-scattering method. γ-rays were produced from the head-on collision of a circularly polarized laser with ultra-relativistic electrons (see Tab. 1.2 for parameters) over a 4 m long straight section (Fig. 1.9). A multi-mirror system allows to remove the sensitive equipment from the direct view of the electron beam, and insures a good transmission of the produced γ-rays [39]. γ-rays up to 56 MeV were obtained and an integrated flux of 2×10^7 photon/bunch flux with a bunch length of 31 ps was reported [40].

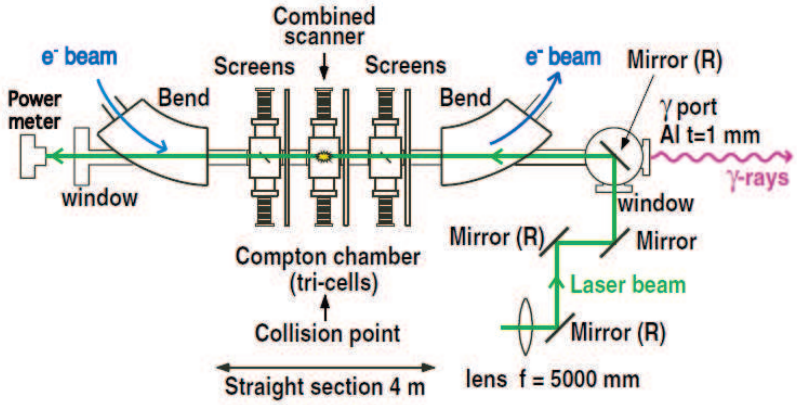

Figure 1.9: Experimental setup for the production of polarized γ-rays from Ref. [40].

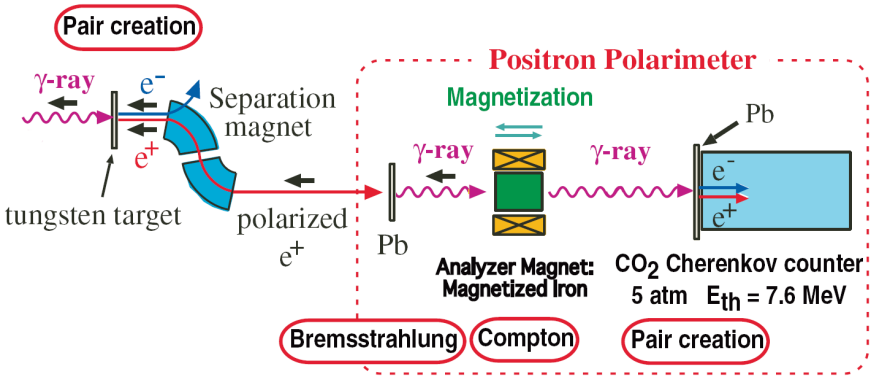

Figure 1.10: Polarized positron production and analysis line of the KEK-ATF demonstration experiment from Ref. [40].

A 1 mm thick tungsten foil was used to convert γ to e^+e^-, with a large energy spectra ranging from rest particles up to the photon maximum energy $(k - 2m)$.

Positrons with a mean energy of 36 MeV were selected with a magnetic channel and analyzed using a Compton transmission polarimeter (Fig. 1.10). A longitudinal polarization degree of 73±15±19 % was reported, where the first error due to statistics and the second one due to systematics.

3.2 Helical undulator

3.2.1 Principle of operation

Synchrotron radiation produced by charged particles bending in undulator magnets is an interesting tool to obtain γ-rays. Considering a magnetic section composed of transverse fields for which $\int B_\perp dz = 0$, an electron beam oscillates around its natural path defined in absence of magnetic field. This allows electrons to progress forward and produce photons at each oscillation. A helical undulator can be seen as such a magnet including a great number of periods (λ_u) of alternating transverse fields. The photons with energy k are emitted along the electron motion within a cone of angle $\theta \approx 1/\gamma$ where γ is the Lorentz boost of the electron beam. The field strength is characterized by the K factor

$$K = \frac{eB_0\lambda_u}{2\pi mc^2} \approx 0.934\, B_\perp \lambda_u [\mathrm{T}\cdot\mathrm{cm}]\,. \tag{1.32}$$

Three different cases can be distinguished:

- $K < 1$, the undulator works as a relativistic antenna and emits mainly one photon wavelength $\lambda_n{=}2\pi\hbar c/k_n{=}n\lambda_u(1+K^2)/(8\pi^2\hbar^2c^2\gamma^2)$, with harmonic number $n = 1$ and some higher order harmonics (n>1);

- $K \approx 1$, a larger number of harmonics becomes apparent, corresponding to different photon wavelengths;

- $K \gg 1$, the photon spectrum is close to synchrotron radiation.

In the last case, for N periods of the undulator, the brilliance of the produced photon beam is $2N$ larger than for a dipole magnet. In the other cases, the gain can be even larger and improve the brilliance by a factor N^2, corresponding to a narrowing wavelength spectrum. It is interesting to make K even smaller, in order to obtain a well defined photon beam, by making λ_u small while keeping B_0 high. The photon wavelength spectrum of a helical undulator is given by [41]

$$\frac{dN}{dk}[\frac{1}{m.MeV}] = \frac{10^6e^3}{4\pi\epsilon_0c^2\hbar^2}\times\frac{K^2}{\gamma^2}\sum_{n=1}^{\infty}\left[J_n'^2(x_n)+\left(\frac{\alpha_n}{K}-\frac{n}{x_n}\right)^2 J_n^2(x_n)\right]\Theta(\alpha_n^2), \tag{1.33}$$

where ϵ_0 is the vacuum permittivity, $\hbar$ the Planck constant, n is the number of harmonics considered, $J_n(x), J_n'(x)$ are the Bessel functions, $\Theta(x)$ is the Heaviside function, and

$$\alpha_n^2 = \frac{n}{r} - 1 - K^2, \quad x_n = 2Kr\alpha_n \;\; and \;\; r = \frac{\lambda_u}{2\gamma^2\lambda}\,. \tag{1.34}$$

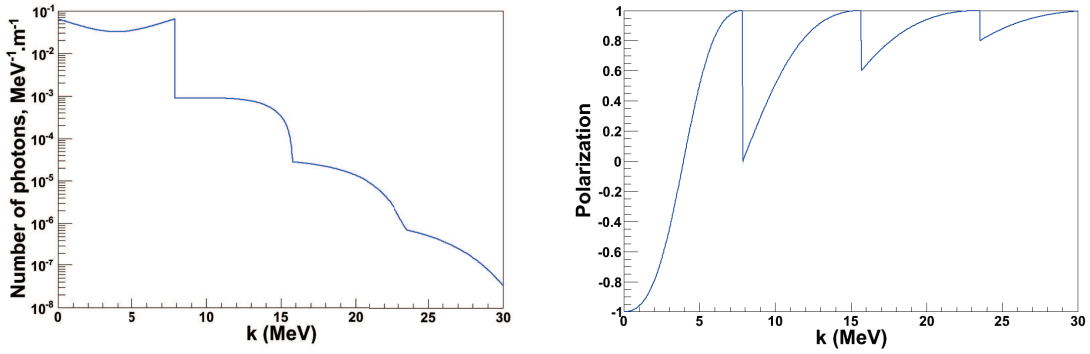

Figure 1.11: Calculated energy evolution of the density of the number of photons created per beam electron (left) and of the longitudinal polarization of the undulator radiation (right) for the E166 experiment.

The polarization of the γ-rays produced by a helical undulator can be obtained from the ideal case at $\theta = 0°$ emission angle. In the dipole approximation, the circular polarization degree of the first 2 harmonics is given by [42]

$$P_n = \frac{2s_n - 1}{1 - 2s_n + 2s_n^2} \tag{1.35}$$

where $s_n = k/k_n$ is the photon energy k normalized by the maximum energy k_n of the harmonic number n.

3.2.2 The E166 experiment at SLAC

Parameter	$B_\perp$ (T)	λ_u (cm)	K	k_1 (MeV)	N_γ (per e^-)
Value	0.7166	0.2540	0.17	7.89	0.35

Table 1.3: Properties of the E166 helical undulator [46].

The E166 experiment [46] at the Stanford Linear Accelerator Center (SLAC) was designed to demonstrate the efficient production of polarized positrons from circularly polarized photons produced by a helical undulator, in the perspective of the ILC project. The polarized γ-rays were generated from a 46.6 GeV electron beam travelling through a 1 m long helical undulator (see Tab. 1.3 for specifications). The density and the polarization spectra of the produced photons are shown on Fig. 1.11. As expected from the design parameters of the undulator, first harmonic photons are most likely to be produced and higher order harmonics are strongly reduced to a small and almost negligible parasitic contribution. The polarization approaches unity at the first harmonic energy and beyond, but consequently to the energy distribution the average polarization of the photons is about 50 % [46].

Positrons were produced from the interaction of the γ-rays in a 0.81 mm tungsten alloy target, and were analyzed in a specific diagnostic line (Fig. 1.12). This line consists of a focusing solenoid lens followed by a dipole pair that separate positrons

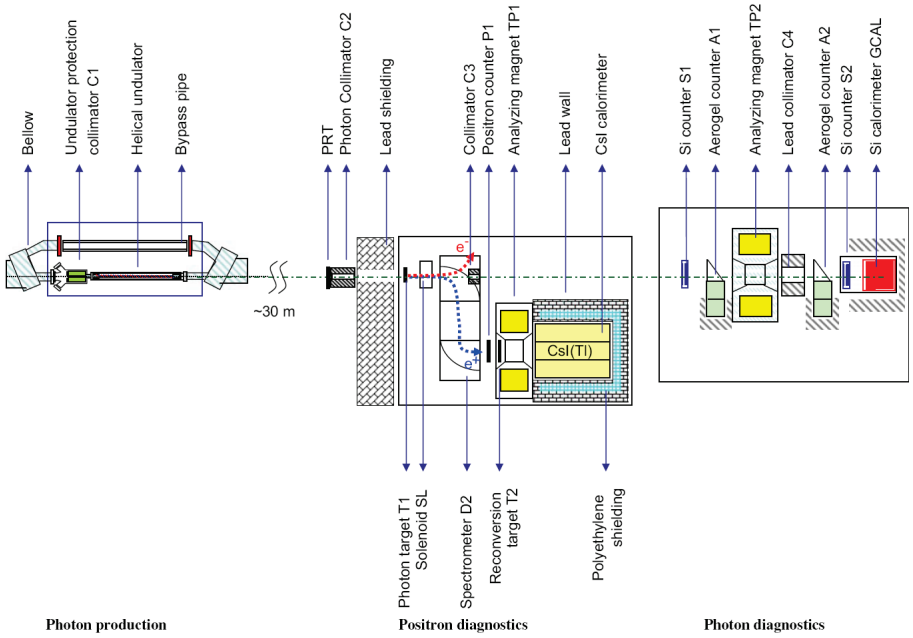

Figure 1.12: Schematic E166 experiment layout from Ref. [46].

from the initial beam and select a tunable energy slice of the positron spectra. The positron polarization is further measured with a Compton transmission polarimeter. These main parts of the diagnostic line will be specifically detailed in the next chapters, as the basic components of a future experiment proposed in this thesis to demonstrate a new polarized positron production technique. Polarizations as large as 80 % were reported (Fig. 1.13) since 8 MeV photons are fully polarized, demonstrating the helical undulator technique.

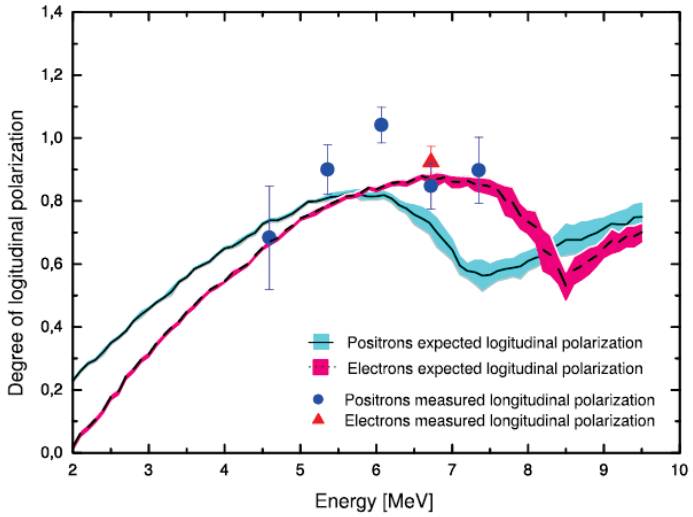

Figure 1.13: Measured electron and positron polarization spectra in the E166 demonstration experiment of the helical undulator scheme from Ref. [49].

4 Conclusion

The nuclear physics program at JLab would benefit from a polarized positron beam. The CEBAF accelerator is comprised of two linacs in which the electron beam goes 5 times thanks to recirculating arcs (Fig. 1.14). The polarity of all magnets in the

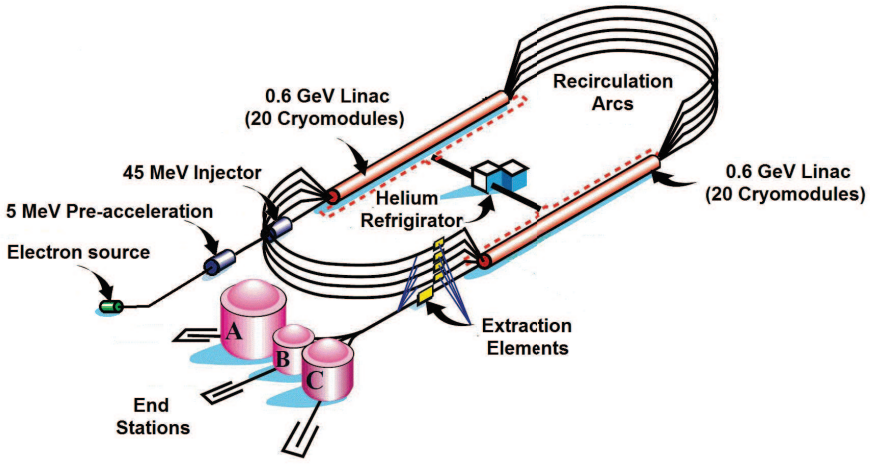

Figure 1.14: Representation of the CEBAF accelerator.

arcs currently set for an electron beam has to be flipped in order to drive a possible positron beam into the linacs. This prevents the use of both electrons and positrons at the same time in the accelerator. The existing or demonstrated technologies to produce positrons involve $\sim GeV$ electron beams for tens of MeV positrons. One pass through the first linac is possible since it does not require the arcs and can accelerate electrons up to 0.6 GeV. In the same conditions, except for the electron beam energy, γ-rays and positrons of 12.58 MeV could be produced theoretically with the Compton back scattering technique. However it is not realistic to consider the helical undulator method for CEBAF as a 17 GeV electron beam is necessary to produce 1.022 MeV photons. The positrons from Compton back scattering at the MeV level can be collected into a beam. The construction of a linac long tunnel would be required to take back these positrons where MeV electrons are usually running in the machine so that it can be accelerated like the electron beam would be, going through the 5 recirculation arcs and reach the nominal 6 GeV energy. Polarized positrons with energy comparable to the electron beam at the CEBAF injector ($\sim$MeV) would allow the very same injector to accelerate positrons into CEBAF and would not require a linac long tunnel construction. Bremsstrahlung photons created in a target by a polarized electron beam are circularly polarized, and according to the same process involved in the other schemes, would transfer their polarization to positrons. This new production technique is the main focus of this thesis. The expected performances of such a scheme, the design and the construction of the corresponding demonstration experiment are described in the next chapters.

Chapter 2

Bremsstrahlung positron source

1 Introduction

As elementary processes of electromagnetic physics, the bremsstrahlung and pair production reactions have been investigated by numerous authors (see Ref. [50, 51] for a review). The study of polarization phenomena in these processes is however limited to a small number of calculations, from the earlier work of H. Olsen and L. Maximon [8] to the most recent one of E. Kuraev and collaborators [52]. Although the very first calculations did set the physics ground for a polarized electron based polarized positron source, it is only in a recent past that the bremsstrahlung of polarized electrons was investigated in this direction [53, 54], though never pursued.

Electrons, and more generally any charged particles, traversing a material loose energy by radiation and collision. In a collision process, the energy release transforms into atom excitation and ionization, leading to the emission of secondary electrons or photons; this represents the main contribution to target heating effects. The interaction between the electromagnetic fields of the incoming electron and of the target nucleus, and to a lesser extent of the atomic electrons, is the main source of radiation leading to the creation of secondary photons which energy varies up to the primary electron energy. The interaction of these photons with the nucleus is the origin of the positrons of interest evolving as the electromagnetic shower develops in the material.

This chapter reviews the main components and parameters for the operation of a polarized positron source and develops an optimization scheme based on the figure-of-merit. The theoretical description of the main elementary electromagnetic processes involved in the production of positrons is also discussed, with a particular emphasis on the polarization transfer at low energy.

2 Elementary processes

2.1 Bremsstrahlung

2.1.1 Unpolarized cross section

As the essential mechanism for the production of high energy photons, the bremsstrahlung process is a text-book reaction widely investigated theoretically and ex-

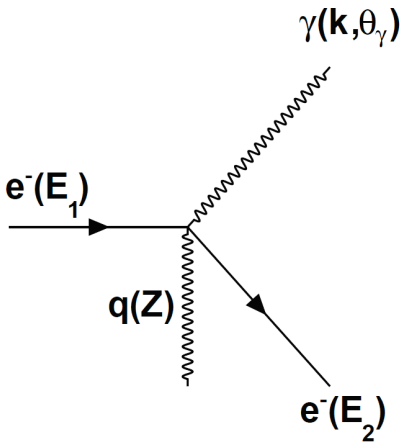

Figure 2.1: Feynman diagram for the electron bremsstrahlung off a nucleus with electrical charge Z; the initial electron, with total energy E_1, radiates a photon with an energy k at an angle θ_γ and changes the total energy for E_2.

perimentally [55] . Two types of reactions can be considered: the electron-electron and the electron-nucleus bremsstrahlungs. The contribution of the former process to the total electron radiation being small, only the electron-nucleus bremsstrahlung (Fig. 2.1) is considered further. The expression of the bremsstrahlung cross section is derived from the transition matrix element between the initial and final states of the reaction. This matrix involves the interaction Hamiltonian and the wave functions of an electron in a screened nuclear Coulomb field. Because the wave functions must be represented as an infinite series [57], the Dirac equation cannot be solved [58]. This situation led to different approximations and procedures wether the Schrödinger or Dirac form of the Hamiltonian, or a truncated series were used.

Calculations of the bremsstrahlung cross section have been developed for different conditions and regions of applicability [50] such as relativistic or non-relativistic regimees, small or large angles, neglecting or considering Coulomb corrections and/or screening effects... The evaluation presented here, using the Furry-Sommerfeld-Maue wave functions [58, 59] including Coulomb corrections and screening effects (important at relativistic energies), is relevant to accelerator energies. The energy validity range constrains the initial electron energy E_1, the final electron energy E_2 and the photon $k{=}E_1 - E_2$ energy to be much larger than the electron mass at rest ($E_1, E_2, k \gg 1$, where energies are expressed in units of the electron mass). The angular range of applicability is given by the condition $u < 1/E_1$, where $\vec{u}$ is the vector of the initial electron/positron momentum $\vec{p_1}$ perpendicular to the photon direction $\vec{k}$, $u = |\vec{u}| \approx p_1\theta_\gamma$ in the small angle limit. The accuracy of the cross section is estimated to be of the order of $\alpha^2 Z^2 \ln(E_1)/E_1$ [58], being 6 % at 10 MeV or 1 % at 100 MeV for a tungsten nucleus ($Z{=}74$). The corresponding expression is given by

$$\frac{d^2\sigma}{dk d\xi} = 2\alpha Z^2 r_e^2 \frac{1}{k\,E_1^2}\left[(E_1^2+E_2^2)(3+2\Gamma) - 2E_1E_2(1+4u^2\xi^2\Gamma)\right] \qquad (2.1)$$

where α is the fine structure constant, r_e is the electron classical radius, and Γ

comprises the Coulomb and screening corrections

$$\Gamma = \mathcal{F}\left(\frac{\delta}{\xi}\right) - \ln(\delta) - 2 - f(Z)\,. \tag{2.2}$$

The Coulomb correction $f(Z)$ is parametrized as [59]

$$f(Z) = a^2 \sum_{n=1}^{\infty} \frac{1}{n(n^2+a^2)} \tag{2.3}$$

where $a = \alpha Z$, and the screening effects are represented by the function $\mathcal{F}(\delta/\xi)$ depending on the angle parameter $\xi{=}1/(1+u^2)$ and the energy parameter $\delta = k/2E_1E_2$.

Δ	$-\mathcal{F}(\frac{\delta}{\xi})$	Δ	$-\mathcal{F}(\frac{\delta}{\xi})$
0.5	0.0145	40	2.001
1	0.0490	45	2.114
2	0.14	50	2.216
4	0.3312	60	2.393
8	0.6758	70	2.545
15	1.126	80	2.676
20	1.367	90	2.793
25	1.564	100	2.897
30	1.731	120	3.078
35	1.875		

Table 2.1: Screening effects in the intermediate regime parametrized according to the parameter $\Delta{=}(6Z^{-1/3}/121)(\xi/\delta)$.

The Born approximation screening correction is [8]

$$\mathcal{F}\left(\frac{\delta}{\xi}\right) = \int_{(\delta/\xi)}^{\infty} \left([1-F(q)]^2 - 1\right) \frac{q^2 - (\delta^2/\xi^2)}{q^3}\, dq \tag{2.4}$$

where $F(q)$ is the atom form factor and q is the momentum transferred to the nucleus. Within the Thomas-Fermi model of the atom, the form factor can be written

$$\frac{1-F(q)}{q^2} = \sum_{i=1}^{3} \frac{\alpha_i}{\beta_i^2 + q^2} \tag{2.5}$$

with $\beta_i{=}(Z^{1/3}/121)b_i$ and $b_1{=}6.0$, $b_2{=}1.2$, $b_3{=}0.3$. The final expression after analytical integration becomes

$$\mathcal{F}\left(\frac{\delta}{\xi}\right) = -\frac{1}{2}\sum_{i=1}^{3} \alpha_i^2 \ln(1+B_i) + \sum_{i=1}^{3}\sum_{j=1}^{3} \alpha_i\alpha_j \left[\frac{1+B_j}{B_i - B_j} \ln(1+B_j) + \frac{1}{2}\right] \tag{2.6}$$

with $B_i{=}(\beta_i\xi/\delta)^2$ and $\alpha_1{=}0.1$, $\alpha_2{=}0.55$, $\alpha_3{=}0.35$. The screening effects are minimum for large δ values and maximum when $\beta_i\xi/\delta \gg 1$. In the later case, eq. 2.6 reduces to

$$\mathcal{F}\left(\frac{\delta}{\xi}\right) = \ln\left(\frac{111\, Z^{-1/3}\xi}{\delta}\right)\,. \tag{2.7}$$

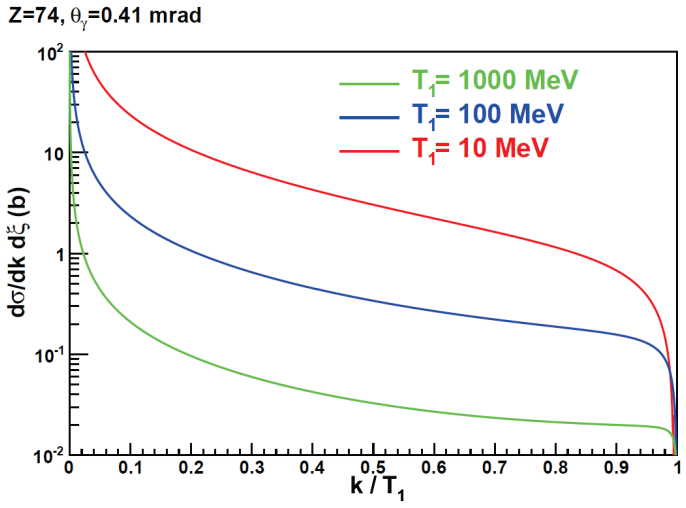

Figure 2.2: Bremsstrahlung differential cross section off a tungsten nucleus for different electron kinetic energies.

Tab. 2.1.1 is giving numerical values for the intermediate regime following eq. 2.6.

The doubly differential bremsstrahlung cross section for different initial electron kinetic energies is represented on Fig. 2.2 as a function of the dimensionless photon reduced energy. A typical dominance of low frequencies resulting from the $1/k$ dependence is observed, as well as the increase of the cross section with electron energies at a fixed absolute photon energy. These calculations are reliable for intermediate, high, and even small energies except for the high frequency part of the spectra, when the final electron is almost at rest. This is a known feature partly connected to the strength of the Coulomb corrections for heavy nuclei. Over the years, corrections have been developed [60] which rely on the finite cross sections experimentally measured but were implemented only for the energy differential cross sections.

2.1.2 Polarization transfer

The polarization transfer from an electron to a photon can be parametrized [61] within the Stokes formalism in terms of a matrix relation referenced with respect to the interaction plane (Fig. 2.3)

$$\begin{pmatrix} I \\ P_1 \\ P_2 \\ P_3 \end{pmatrix} = T^{\gamma}_{Brem.} \begin{pmatrix} 1 \\ S_1 \\ S_2 \\ S_3 \end{pmatrix} \tag{2.8}$$

where I represents the cross section, S_i are the polarization components of the electron, and P_i are the polarization components of the photon, according to

S_1 : transverse polarization in the plane of interaction along the x-axis;

S_2 : polarization component perpendicular to the interaction plane (y-axis);

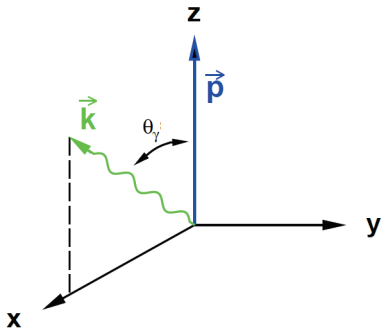

Figure 2.3: Interaction plane (xz) of the bremsstrahlung reaction built from the incoming electron and the produced photon.

S_3 : longitudinal polarization along the z-axis;

P_1 : linear polarization with respect to x- and y-axis;

P_2 : linear polarization with respect to the axis oriented at $45°$ to the right of the x- and y-axis;

P_3 : right circular polarization.

$T^{\gamma}_{Brem.}$ is the bremsstrahlung interaction matrix

$$T^{\gamma}_{Brem.} = \begin{pmatrix} I_0 & 0 & 0 & 0 \\ D & 0 & 0 & 0 \\ 0 & 0 & 0 & 0 \\ 0 & T & 0 & L \end{pmatrix} \tag{2.9}$$

with

$$\begin{aligned} I_0 &= (E_1^2 + E_2^2)(3 + 2\Gamma) - 2E_1E_2(1 + 4u^2\xi^2\Gamma) && (2.10)\\ D &= 8E_1E_2u^2\xi^2\Gamma/I_0 && (2.11)\\ T &= -4kE_2\xi(1 - 2\xi)u\Gamma/I_0 && (2.12)\\ L &= k[(E_1 + E_2)(3 + 2\Gamma) - 2E_2(1 + 4u^2\xi^2\Gamma)]/I_0\,. && (2.13) \end{aligned}$$

Therefore the photon polarization components for the bremsstrahlung process is

$$\begin{pmatrix} P_1 \\ P_2 \\ P_3 \end{pmatrix} = \begin{pmatrix} D \\ 0 \\ S_1T + S_3L \end{pmatrix}. \tag{2.14}$$

The previous relation shows particularly that the bremsstrahlung reaction yields a linearly polarized photon beam independently of the initial electron beam polarization, and that a circularly polarized photon beam can be obtained from a transversely or a longitudinally polarized electron beam. The process is also insensitive to the perpendicular polarization. These features are currently used at electron

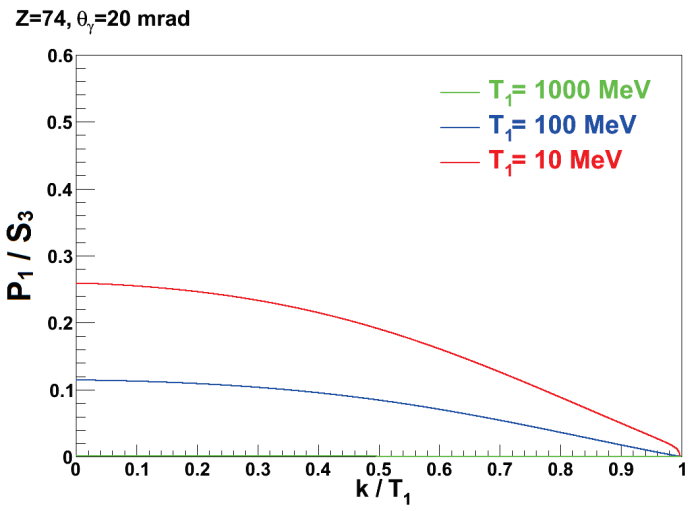

Figure 2.4: Photon linear polarization at a scattering angle of 20 mrad for different initial electron energies.

facilities to produce polarized photon beams, the tagged photon beam of JLab [62] being the most recent example.

This description of the photon polarization observables, following the initial work of Ref. [8] (referred to as OM in the following) including effects of the nuclear field screening and corrections to the Born approximation, is still the reference calculation implemented in the GEANT4 simulation package [63,64]. Fig. 2.4 shows the photon linear polarization at a fixed scattering angle for different electron beam energies: the maximum polarization degree is obtained at low frequencies $k/(T_1 - 2)$. This is opposite to the photon circular polarization which is maximum at high frequencies, the most efficient polarization transfer corresponding to a longitudinal initial polarization (Fig. 2.5). Similarly to the unpolarized cross section, these polarization transfers are restricted to relativistic energies and small scattering angles. The accuracy of these results is degraded below 50 MeV, and it should be noticed that an unphysical behavior ($P_3/S_3 > 1$) occurs at the end-point even within the prescribed validity region. Nevertheless, the circular polarization appears essentially universal.

Within the same formalism, the polarization of the remaining electron after emitting a bremsstrahlung photon is deduced from the interaction matrix $T^e_{Brem.}$ describing depolarization effects [65]

$$T^e_{Brem.} = \begin{pmatrix} I_0 & 0 & 0 & 0 \\ 0 & G & 0 & E \\ 0 & 0 & G & 0 \\ 0 & F & 0 & G+H \end{pmatrix} \tag{2.15}$$

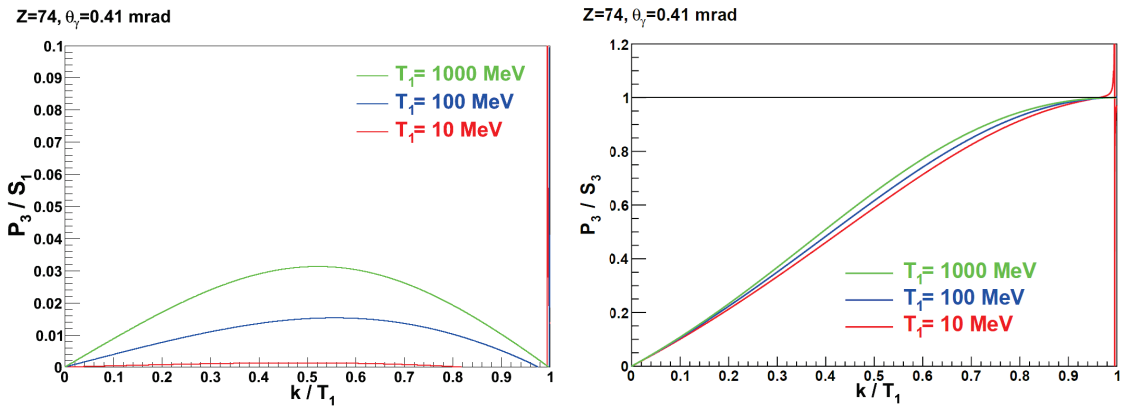

Figure 2.5: Photon circular polarization from transversely (left) and longitudinally (right) polarized electrons at a fixed scattering angle of 0.41 mrad and different electron beam energies.

where

$$E = 4k\xi E_1 u(2\xi - 1)\Gamma/I_0 \tag{2.16}$$
$$F = 4k\xi E_2 u(2\xi - 1)\Gamma/I_0 \tag{2.17}$$
$$G = 4kE_1E_2\left[1 + \Gamma - 2u^2\xi^2\Gamma\right]/I_0 \tag{2.18}$$
$$H = k^2\left[1 + 8\Gamma(\xi - 0.5)^2\right]/I_0 \tag{2.19}$$

leading to the final electron polarization components

$$\begin{pmatrix} S_1' \\ S_2' \\ S_3' \end{pmatrix} = \begin{pmatrix} S_1G + S_3E \\ S_2G \\ S_1F + S_3(G+H) \end{pmatrix}. \tag{2.20}$$

The remaining electron polarization after interaction is in a way complementary to the photon polarization (Fig. 2.6): the electron polarization is high when the polarization transfer is small, and conversely. Similarly to polarization transfers, an unphysical region ($S_3'/S_3 < -1$) at small electron energies is observed, reciprocally to the features of polarization transfers at photon high frequencies.

2.1.3 Singularities in bremsstrahlung

Polarized observables in the bremsstrahlung process calculated following the OM prescription have been shown above full polarization in some regions of the energy spectra. These singularities originate mathematically from the zero crossing of the differential cross section represented in fig. 2.2 which is proportionnal to the I_0 parameter defined by eq. 2.10 and involved in the polarization transfer calculations. Depending on the kinematical factors involved, they express with more or less strength in the different polarization observables. This feature, leading to negative cross section, is better known as the end-point or tip problem and was identified as too large Coulomb corrections for heavy nuclei. This violation of positivity constraints is nevertheless an inherent feature of OM calculations implementing Coulomb corrections at the cross section level instead of the reaction amplitude level [66]. Neglecting these corrections allow to regularize the calculations but do

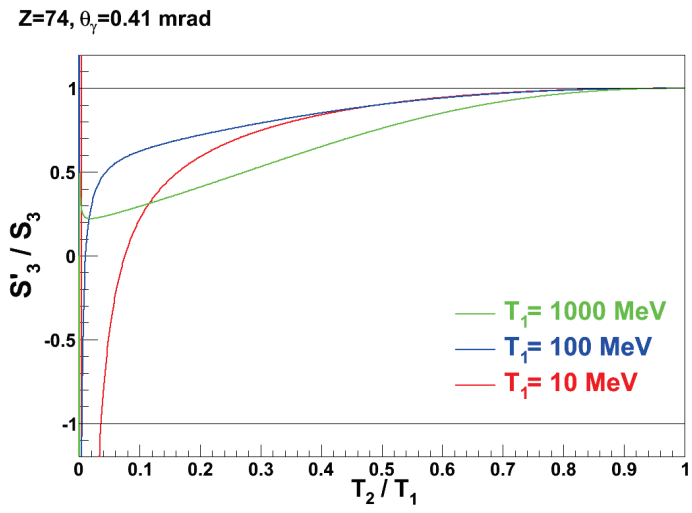

Figure 2.6: Electron polarization after the bremsstrahlung interaction of longitudinally polarized electrons, for different initial beam energies and at a fixed photon emission angle.

not prevent yet from unphysical results at the tip region, which then appear as a violation of unitarity constraints (polarization transfers larger than 1).

2.2 Pair creation

2.2.1 Unpolarized cross section

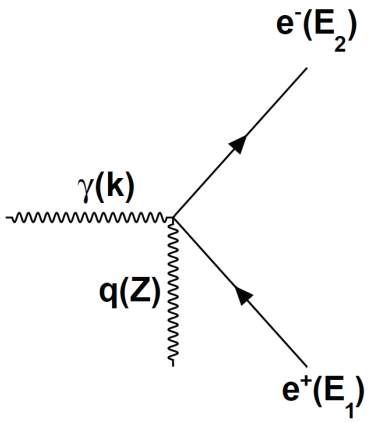

Figure 2.7: Feynman diagram for pair-creation off a nucleus with electrical charge Z; the interaction between an incoming photon of energy k and the nuclear field represented by a virtual photon of momentum q creates a positron with total energy E_1 at an emission angle θ_e, and an electron with total energy E_2.

The pair creation and bremsstrahlung reactions are reciprocal processes, as can be seen from the comparison between Fig. 2.1 and Fig. 2.7. This inverse nature translates into symmetry properties which allow to derive the physics observables of pair creation from the bremsstrahlung ones via the simple substitution $E_2 \rightarrow$

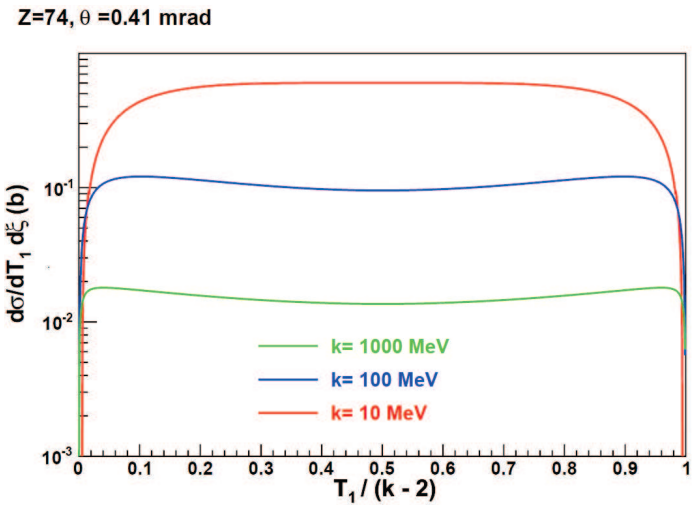

Figure 2.8: Differential cross section of the pair creation reaction off a tungsten nucleus, at three different photon energies and a fixed electron emission angle.

$-E_2$. This follows from energy conservation which is given by $E_1 = k + E_2$ for bremsstrahlung, and $k = E_1 + E_2$ for pair creation.

The cross section for the pair creation reaction, differential in energy and angle can be written [8]

$$\frac{d^2\sigma}{dE_1 d\xi} = 2\alpha Z^2 r_e^2 \frac{1}{k^3}\left[(E_1^2 + E_2^2)(3 + 2\Gamma) + 2E_1E_2(1 + 4u^2\xi^2\Gamma)\right] \tag{2.21}$$

where the different factors are defined similarly to bremsstrahlung. As a direct consequence of the production of two identical particles from a massless photon, the cross section is essentially flat over the energy phase space (Fig. 2.8). The validity range of this description is limited to intermediate and high energies, following the same restrictions as bremsstrahlung. Nevertheless, the cross section suffers from the same singular features as bremsstrahlung which is shown at the low and high energy ends of the spectra, when one particle from the pair is at rest.

2.2.2 Polarization transfer

The polarization transfer from photon to electron/positron can be expressed within the Stokes formalism, following the same substitution procedure as for the unpolarized cross section [61]. The interaction matrix of the pair creation process is the transpose of the bremsstrahlung ones (eq. 2.9), reflecting the inverse nature of the processes. In the interaction plane supported by the incoming photon and the electron/positron (Fig. 2.9), the interaction matrix is given by

$$T^e_{Pair.} = \begin{pmatrix} 1 & D & 0 & 0 \\ 0 & 0 & 0 & T \\ 0 & 0 & 0 & 0 \\ 0 & 0 & 0 & L \end{pmatrix} \tag{2.22}$$

with

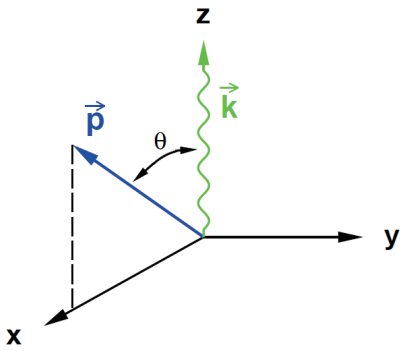

Figure 2.9: Interaction plane (xz) of the pair creation reaction built from the incoming photon and the produced electron/positron.

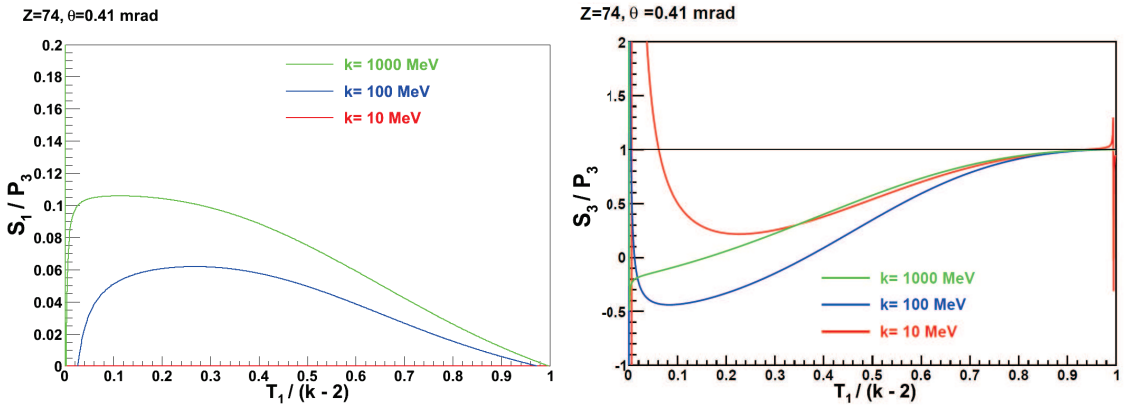

Figure 2.10: Polarization transfer components to the electron/positron from a circularly polarized photon at different energies and a fixed emission angle: transverse component (left) and longitudinal component (right).

$$I_0 = (E_1^2 + E_2^2)(3 + 2\Gamma) + 2E_1E_2(1 + 4u^2\xi^2\Gamma) \quad (2.23)$$

$$D = -8E_1E_2u^2\xi^2\Gamma/I_0 \quad (2.24)$$

$$T = 4kE_2\xi(1 - 2\xi)\Gamma u/I_0 \quad (2.25)$$

$$L = k[(E_1 - E_2)(3 + 2\Gamma) + 2E_2(1 + 4u^2\xi^2\Gamma)]/I_0 \quad (2.26)$$

leading to the polarization of the created electron or positron

$$\begin{pmatrix} S_1 \\ S_2 \\ S_3 \end{pmatrix} = \begin{pmatrix} P_3T \\ 0 \\ P_3L \end{pmatrix} . \quad (2.27)$$

This expression shows that only circularly polarized photons create a polarized e^+e^- pair. The resulting polarization has transverse and longitudinal components, the latter dominating in most cases (Fig. 2.10). The longitudinal polarization transfer is similar in shape to the circular polarization transfer but spans a larger range

of values between -1 and +1. Singular behaviors in the validity domain of these calculations are also observed at both ends of the spectra but with a more prominent expression than for the bremsstrahlung.

2.2.3 Singularities in pair creation

The mathematical origin of the singularities observed in the polarization transfer for the pair creation process is, as in the bremsstrahlung case, the zero crossing of the unpolarized cross section. However, their physics understanding remains mysterious: neglecting Coulomb corrections or screening effects do not regularize the calculations (Fig. 2.11), while affecting the magnitude of the polarization transfer. It is even more dramatic at low energy (<4 MeV) where the polarization transfer violates unitarity constraints over the whole phase space, though such energies are out of the prescribed validity range of OM calculations. One should look for other physics origins to expect regularizing these calculations.

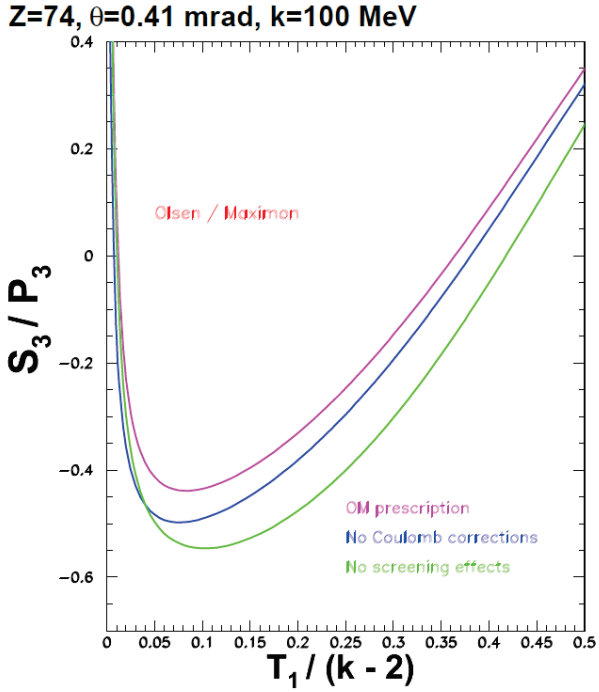

Figure 2.11: Longitudinal polarization transfer for different calculation prescriptions at fixed photon energy and emission angle. The lower half of the electron/positron energy phase space is emphasized.

3 Revisiting bremsstrahlung and pair creation processes

3.1 Electron mass effects

The specific unphysical features of OM calculations did motivate a novel approach developed by E. Kuraev and collaborators [52] (referred to as KBST in the follow-

ing). This very recent work takes advantage of the most modern techniques to reformulate in the infinite momentum frame the matrix element of the bremstrahlung and pair creation reactions. The differential cross sections and polarization observables are rederived within this framework in the Born approximation, considering screening effects and specifically taking into account the effects of finite electron mass. Coulomb corrections are only considered for the angle integrated cross sections. The polarization observable results are discussed below with respect to the issues reported in the previous section.

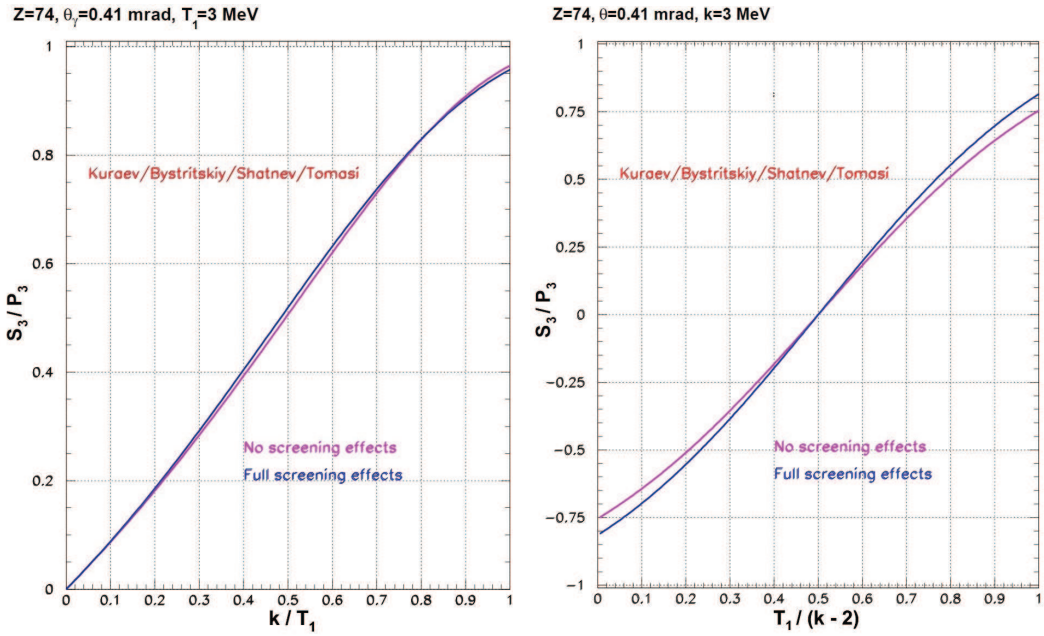

Figure 2.12: Photon circular polarization in the bremsstrahlung of longitudinally polarized electrons (left) and electron/positron longitudinal polarization in the pair materialization of circularly polarized photons (right), according to the KBST approach [52] for the extreme cases, full or no screening; displayed curves correspond to low energy incoming particles and a fixed emission angle.

The circular polarization of the bremstrahlung photons produced by a fully longitudinally polarized electron beam of 3 MeV total energy is represented on Fig. 2.12 (left) for a fixed photon angle, together with the longitudinal polarization of positrons produced by a circularly polarized photon beam of 3 MeV (right) at a similar positron angle. The KBST calculations do not exhibit any of the singular problems reported for OM calculations and the comparison between the two extreme cases (none and full) show a moderate and mastered effect of screening. It should be noticed that in this energy range, the complete transfer of the initial polarization is not predicted. Furthermore, the polarization transfer for the pair creation process possesses the very remarkable feature of a kinematical symmetry ($S_3/P_3 = 0.75$ for $T_1/(k-2) = 0$ and $S_3/P_3 = -0.75$ for $T_1/(k-2) = 1$. It is indeed quite natural to expect such a symmetry in a process where two particles with same mass and spin are produced and it appears surprising that the lack of symmetry of previous calculations was never questioned.
The OM and KBST calculations for the bremsstrahlung process are compared on

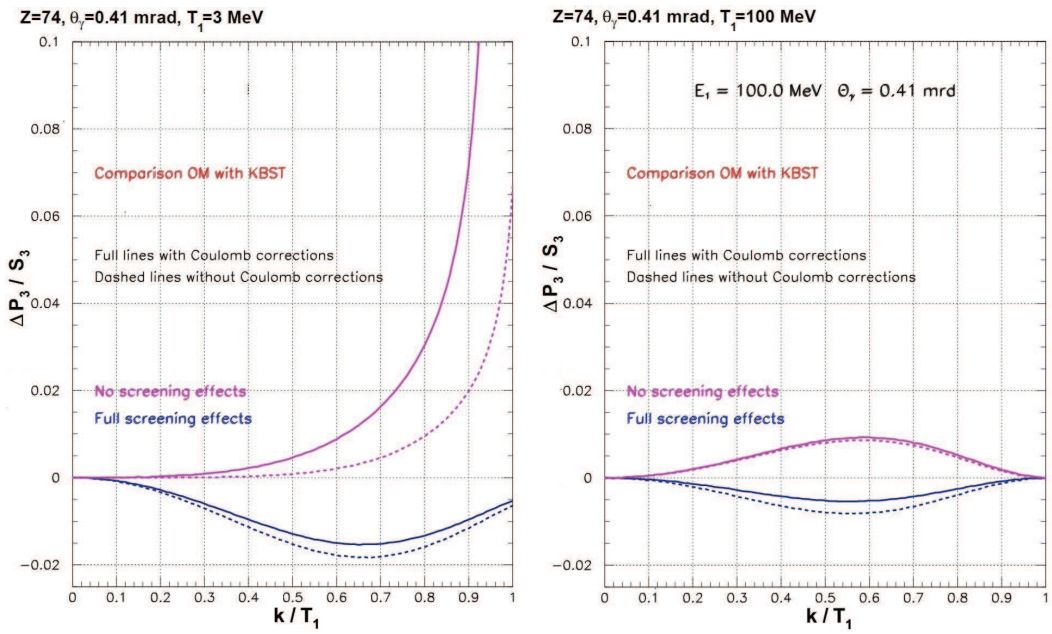

Figure 2.13: Comparison between OM and KBST calculations (ΔP_3 refers to P_3 calculated with OM minus P_3 calculated with KBST) for the bremstrahlung process at low (left) and high (right) energies, and for different physics hypothesis.

Fig. 2.13 for two different beam energies, distinguishing different screening hypothesis and the effect of Coulomb corrections. In terms of physics content, KBST calculations are strictly comparable to OM calculations in absence of Coulomb corrections (dashed lines). At low energy, the difference between these calculations is most striking in the end-point region of the bremsstrahlung and when screening is neglected, consequently to the unphysical behavior of OM calculations in this region of the phase space. In presence of a fully screened nuclear field, Coulomb corrections are less important and the difference between OM and KBST are reasonably small. For a relativistic beam, the calculations are numerically very close to each other.

The same comparison is shown on Fig. 2.14 for the pair creation process. Similarly, the calculations neglecting screening lead to very large differences because of the unphysical behavior of OM results. However, in contrast to the bremsstrahlung process, the full screening calculations show very large differences both at low and high energy. This is a direct consequence of the lack of kinematical symmetry in OM calculations.

Beyond the topical issue of Coulomb corrections, the main physics output of this comparison is that because of taking into account the finite mass of the electron, KBST calculations are able to provide consistent results for both the bremsstrahlung and pair creation processes with no constraint on the energy of the particles involved in the process. This statement is further supported by noticing that OM calculations become unphysical in kinematical regions where the electron mass is physically important: when the initial electron gives all of its kinetic energy to the photon (bremstrahlung); when one particle of the e^+e^- pair is produced at rest and also at low photon energy (pair creation). Even if bremsstrahlung and pair creation are reciprocal processes, some of the OM approximations valid for the bremsstrahlung

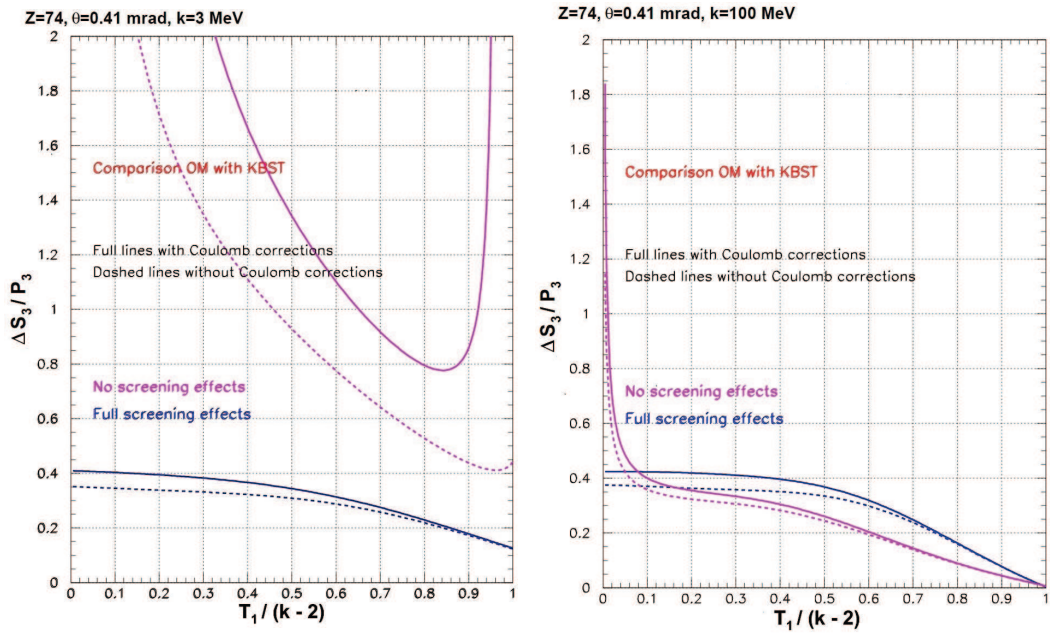

Figure 2.14: Comparison between OM and KBST calculations for the pair creation process at low (left) and high (right) energies, and for different physics hypothesis.

reaction cannot be just exported to the pair creation process.

3.2 Emipirical regularization

The simulation work presented in this thesis was developed prior to the publication of KBST calculations which were initiated by the physics problems encountered with the GEANT4 package where OM calculations were implemented. In the temporary absence of a better calculation an empirical approach was adopted in order to regularize OM polarization observables [67]. It relies on the observation that high energy bremsstrahlung and pair creation suffer from a strong nuclear screening almost over

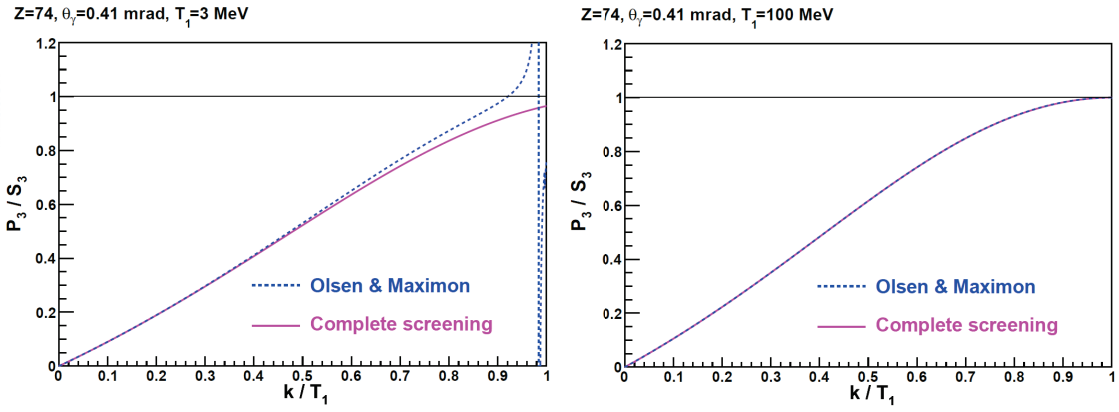

Figure 2.15: Effects of the regularization on the photon circular polarization in the bremsstrahlung of longitudinally polarized electrons at low (left) and high (right) initial energies.

the whole phase space. Therefore the prescription of a full screening was imposed for the calculation of polarization observables.
The consequences of this empirical regularization is displayed on Fig. 2.15 and Fig. 2.16: the full screening prescription provide a physical (i.e. non singular nor larger than unity) description of the polarization transfer at low energy and a good description at high energy. The depolarization of bremsstrahlung electrons is also corrected by the full screening prescription (Fig. 2.17).

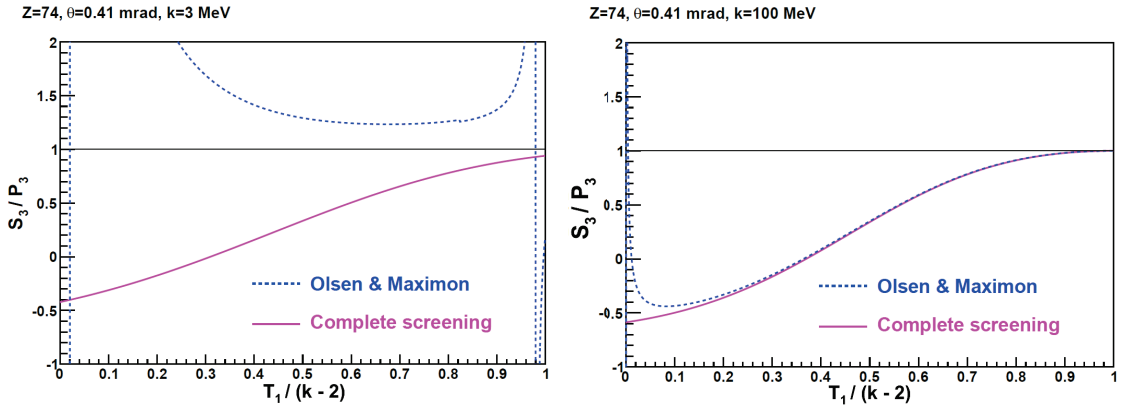

Figure 2.16: Effects of the hot fit regularization on the elctron/positron longitudinal polarization in the pair materialization of circularly polarized photons at low (left) and high (right) initial energies.

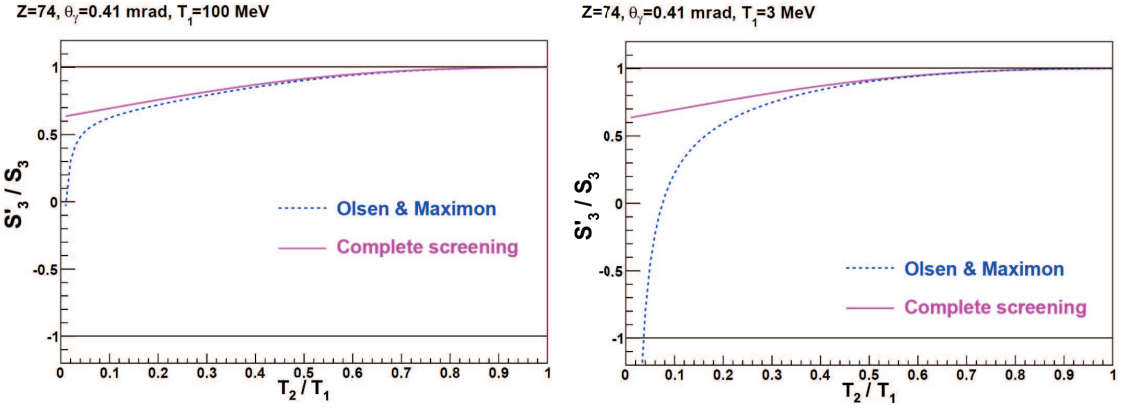

Figure 2.17: Effects of the hot fit regularization on the depolarization of longitudinal electrons in bremsstrahlung at low (left) and high (right) initial energies.

The simulation results discussed in this manuscript were obtained with the regularized OM calculations. Substituting KBST calculations to them is not expected to lead to major effects for the bremsstrahlung but might have a significant impact on the low energy part of the e^+e^- pair spectra.

4 Bremsstrahlung positron source concept

Within an amorphous target, leptons at the MeV energy scale can interact via bremsstrahlung, ionization, Coulomb/multiple scattering and additionally annihilation for positrons. At the same energy scale, photons interact with a material via photoelectric effect, Compton scattering and pair creation. All these processes are sensitive to the polarization, leading to a distortion of the polar distribution and the anisotropy of the azimuthal distribution of secondary particles. The initial polarization of primary and secondary particles is also affected by depolarization effects from successive interactions. At high energy, the emission angles of secondary particles are quite small in low Z elements and the electromagnetic shower develops in the direction of the incident particle. For higher Z materials, this assumption remains valid for the more energetic particles. The target thickness also contributes to the angular spread of secondaries from the increase of multiple scattering of primaries increasing the lateral spread of secondaries, and the increase of energy loss of secondaries reducing the same quantity.

Taking advantage of the work of the E166 Collaboration who implements in GEANT4 the polarization features of these different electromagnetic processes [64], simulations were worked out in order to conceptually optimize a bremsstrahlung positron source for an ideal polarized electron beam with properties (Tab. 2.2) similar to the injector beam of CEBAF. The quantities of interest are the momentum distribution of the positron yield, polarization, and figure-of-merit as they emerge off a production target constituting of tungsten.

Electron energy	< 100 MeV
Electron longitudinal polarization	85 %
Fractional energy spread	± 1 %
Beam transverse size (RMS)	0.5 mm

Table 2.2: Characteristics of the ideal electron beam used for GEANT4 simulations.

4.1 Production efficiency

The positron yield is the quantity of interest for unpolarized positron sources where one would like to achieve the largest positron beam intensity corresponding to the most probable positron momentum. The yield essentially depends on the incoming electron energy and the target material and thickness. The positron momentum distribution is dominated by the bremsstrahlung energy distribution of photons and is limited to $\sqrt{T_1^2 - 1}$, consequently to the pair creation threshold energy. The positron momentum distribution, integrated over emission angles, for 10 MeV electrons at perpendicular incidence on a 100 μm tungsten target is represented on Fig. 2.18: the forward distribution peaks at low momentum (1.4 MeV/c) and the forward region is much more populated than the backward ones. This asymmetric behavior is expected to be even more prominent with increasing energy and less sensitive to the target thickness, as a consequence of the Lorentz boost of incoming particles.

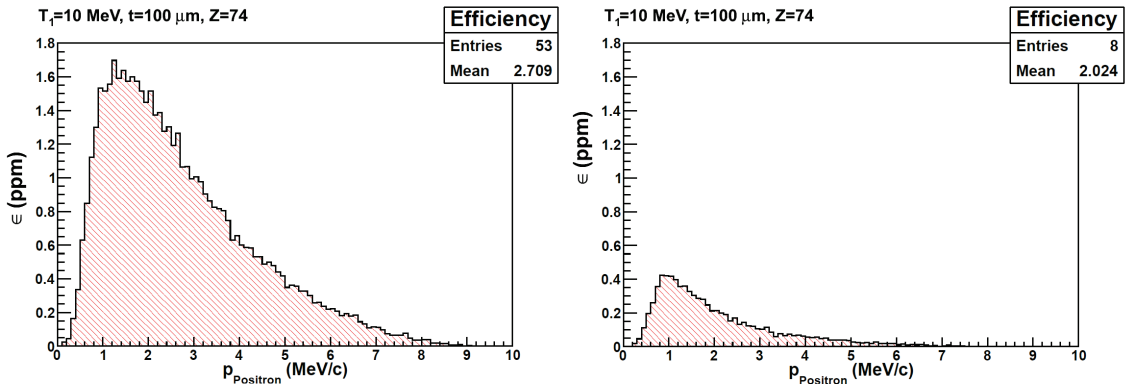

Figure 2.18: Forward (left) and backward (right) angle integrated momentum distribution of positrons created by a 10 MeV electron beam impinging on a 100 μm tungsten target.

The parameters characterizing an unpolarized positron source are consequently the maximum positron yield or production efficiency, and the positron momentum at that maximum.

4.2 Polarization

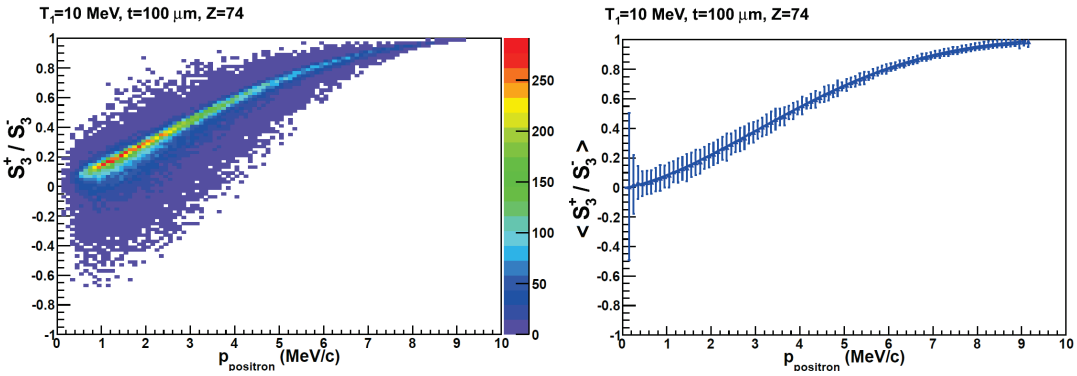

Figure 2.19: Distribution of the longitudinal polarization component of forward positrons from 10 MeV longitudinally polarized electrons off a 100 μm tungsten target (left) and average polarization distribution (right) as a function of the positron momentum.

The positron polarization is obviously a driving parameter of a polarized positron source. The distribution of the longitudinal polarization component of positrons created by a 10 MeV longitudinally polarized electron beam at perpendicular incidence on a 100 μm tungsten target (fig. 2.19 left) exhibits several features. When passing through the target, primary electrons lose energy via inelastic scattering while keeping a high polarization degree: this results in a reduction of the maximum photon energy and consequently of the maximum positron energy with a high polarization degree. This combines with the pair creation from secondaries having lower energies but still significant polarization. The upper bound of the polarization phase space reflects this phenomenon while the lower bound corresponds to the intitial electron beam energy. For thick target the entire phase space above the lower bound is

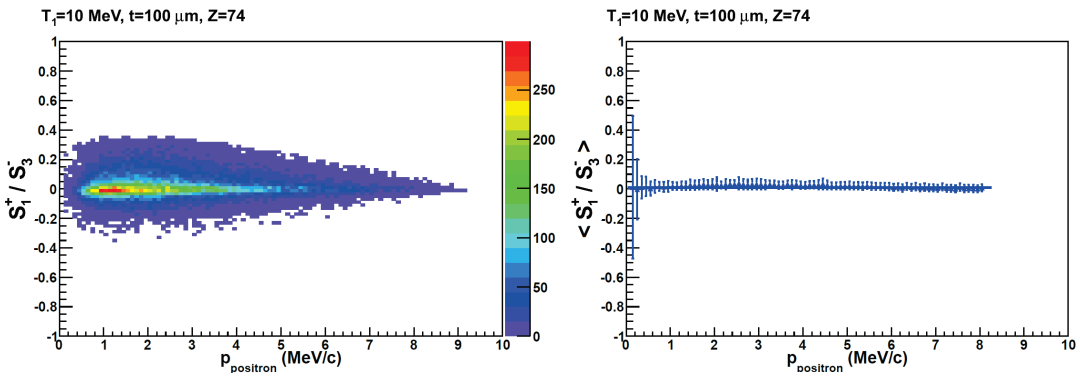

Figure 2.20: Distribution of the transverse polarization component of forward positrons from 10 MeV longitudinally polarized electrons off a 100 μm tungsten target (left) and average polarization distribution (right) as a function of the positron momentum.

populated. The bremsstrahlung origin of the radiated photons translates into the dominance of low polarization at small positron momentum. The average polarization is, as expected, low at small momentum and high at large momentum (fig. 2.19 right).

The transverse polarization component, as referenced in the particle frame, is remarkably small (fig. 2.20 left) as a consequence of the small magnitude of the photon circular polarization transfer and of the bremsstrahlung distribution of photons which favors low frequencies having low polarization from initial electrons. In average (fig. 2.20 right), this component can be safely neglected over the full positron energy range. Therefore the bremsstrahlung of longitudinally polarized electrons effectively yields to longitudinally polarized positrons at high mometum.

The polarization distribution of backward positrons is also of interest even if the expected yields are not favorable. For applications related to condensed matter physics, a scheme was proposed based on the collection of backward positrons [69]. Fig 2.21 shows that that similarly to forward positrons, backward positrons can also have significant longitudinal polarizations.

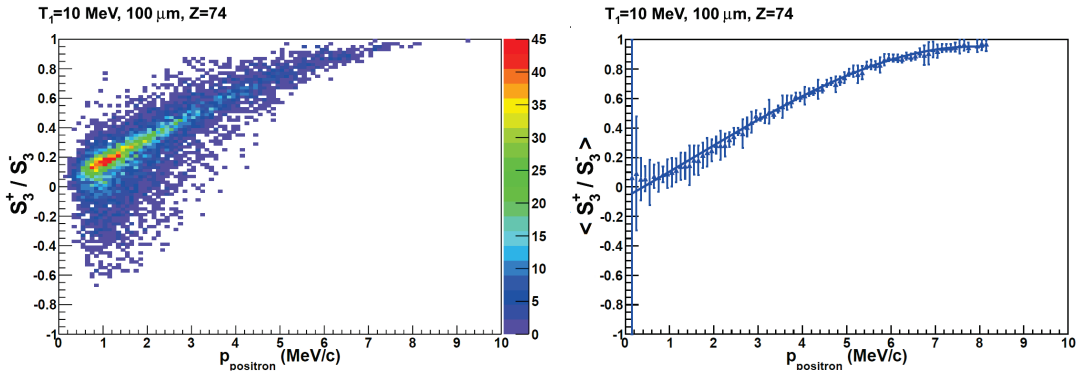

Figure 2.21: Distribution of the longitudinal polarization component of backward positrons from 10 MeV longitudinally polarized electrons off a 100 μm tungsten target (left) and average polarization distribution (right) as a function of the positron momentum.

4.3 Figure-of-merit

The sensitivity of a typical nuclear process to the polarization of an incoming electron/positron beam P_e can be expressed by the differential cross section

$$\frac{d\sigma^{\pm}}{d\Omega} = \frac{d\sigma^{0}}{d\Omega}(1 \pm P_e \mathcal{A}) \tag{2.28}$$

where the sign corresponds to the beam spin projection on the beam axis, and $\mathcal{A}$ symbolizes the analyzing power of the nuclear process, that is the sensivity of the nuclear reaction to the beam polarization. Considering an asymmetry experiment aiming at the measurement of the analyzing power, the experimental asymmetry is given by

$$A_S = \frac{N^+ - N^-}{N^+ + N^-} \tag{2.29}$$

where $N^{\pm}$ is the number of counts measured with an ad-hoc detector for opposite beam spin directions. It can be written

$$N^{\pm} = \rho\, \epsilon \frac{d\sigma^{\pm}}{d\Omega} \Delta\Omega\, N_e \tag{2.30}$$

where ρ is the target nuclei density ($\mathrm{g{\cdot}cm^{-2}}$), ϵ and $\Delta\Omega$ are respectively the detector efficiency and solid angle, and N_e is the number of incoming electrons/positrons of given polarization state.

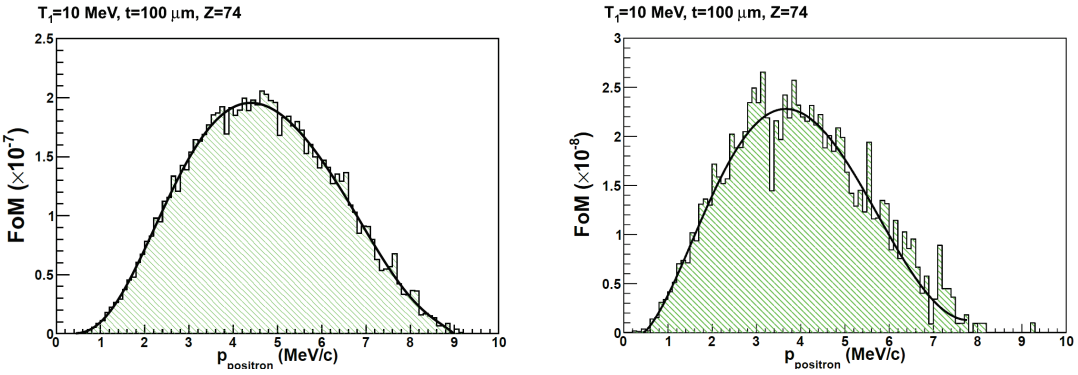

Figure 2.22: FoM of longitudinally polarized positrons created at forward (left) and backward angles by a 10 MeV longitudinally polarized electron beam.

The analyzing power is deduced from the experimental asymmetry according to

$$\mathcal{A} = \frac{A_S}{P_e} \tag{2.31}$$

and its statistical uncertainty is

$$[\delta\mathcal{A}]^2 = \left[P_e^2 \frac{(N^+ + N^-)^2}{4N^+N^-} \right]^{-1}. \tag{2.32}$$

Considering, for the sake of simplicity, the case of small experimental asymmetries ($N^+ \approx N^- \approx N^0$), the previous relation becomes

$$[\delta\mathcal{A}]^2 = \left[2\, P_e^2 N_e\, \rho\epsilon \frac{d\sigma^{0}}{d\Omega} \Delta\Omega \right]^{-1} \tag{2.33}$$

which clearly identifies a part related to the beam and a part related to the nuclear process filtered by the detector: the larger these quantities measured in a given time, the smaller the statistical uncertainty on the physics quantity of interest. The beam related term $P_e^2 N_e$ is the figure-of-merit (FoM) which characterizes the performances of a polarized source.

The positron yield and the polarization can be represented as a single feature via the FoM. The opposite trends of the momentum distribution of the positron yield and of the positron polarization combine in the FoM which presents a maximum value at about half of the total available energy that is 4.4 MeV/c for 10 MeV electrons at perpendicular incidence on a 100 μm tungsten target (fig. 2.22).
Two main parameters are then characterizing a polarized positron source: the maximum FoM and the average positron momentum at that maximum. The average positron production efficiency and the average positron polarization are subsequently determined at that optimum positron momentum.

4.4 Positron collection considerations

While defining the main parameters of a polarized positron source with respect to the physics processes, the previous figures integrated over the angular phase space are obviously not suitable for acceleration purposes. In addition to an angular acceptance, an accelerator system is also parametrized by a momentum acceptance symbolizing the operation of accelerating cavities and of the magnet elements constituting the machine. As an example, the acceptances of the CEBAF accelerator were estimated to be 2-4 mm·mrad (transverse-horizontal admittance) and 3×10^{-3} (momentum admittance) from experimental measurements [68]. Furthermore, the interaction of the initial beam with the target generates a large amount of secondary background particles which forbids any cryogenic system right after the target. A positron collection system is required as an interface between the production target and the accelerator in order to collect, collimate, select, and shape the positron population to constitute an acceptable beam.

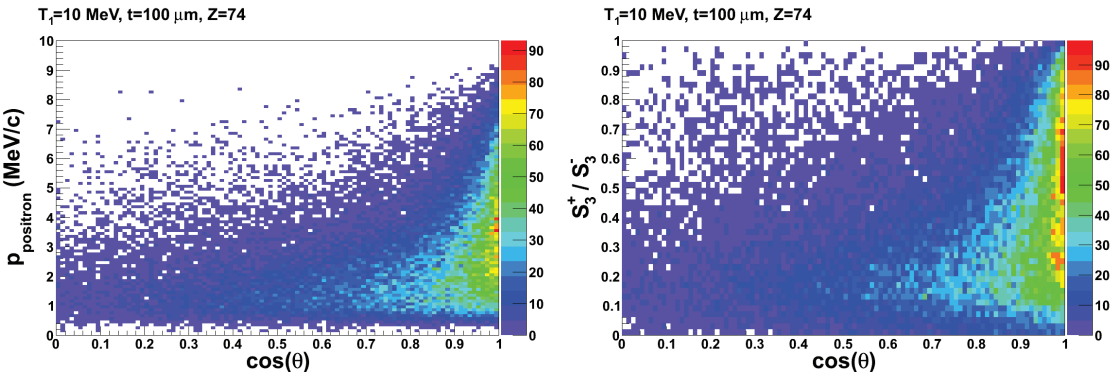

Figure 2.23: Angular distribution of the momentum (left) and the longitudinal polarization of the positrons for a 10 MeV electron beam at perpendicular incidence on a 100 μm tungsten target.

The purpose of the following discussion is to assess the influence of such a system

on the performances of a polarized positron source. The sensitivity of the main parameters driving the optimization a polarized source to the positron angular and momentum acceptances are considered.

4.4.1 Angular acceptance

The angular acceptance of an interface system is here represented by a forward virtual circular collimator centered on the beam axis and with different diameters defining the polar angle acceptance. The FoM is obviously bounded between a null value when the collimator is closed and a maximum value when the collimator is wide open (fig. 2.27 upper left). The raise to this maximum figures the effects of the acceptance increase and the decrease of the optimum momentum (fig. 2.27 upper right) which concur to smaller polarizations (fig. 2.27 lower left) and larger yields (fig. 2.27 lower right) at the optimum momentum. The saturation towards this maximum is more or less fast, depending on the energy of the incoming electron. The momentum acceptance does not influence the trend of the angular acceptance sensitivity but the magnitude of the FoM by acting as a yield enhancer.
The larger the angular acceptance, the better the performances of the polarized positron source. A suitable interface system should then figure a large angular entrance acceptance and a suitable exit one to allow for positron acceleration. This could be achieved to some extent with a set of magnetic elements: solenoid or quarter wave transformers and/or quadrupoles.

4.4.2 Momentum acceptance

The momentum acceptance does influence the shape of the momentum distribution of the yield and the FoM. The comparison between the momentum distribution and the momentum collection distribution (fig. 2.26) figures the natural effect of a relative momentum acceptance as compared to an absolute one. For 10 MeV incident electrons, the optimum FoM is shifted from 4.4 MeV/c to 5.2 MeV/c leading to slightly higher polarization. Its magnitude is however strongly enhanced consequently to the collection of a larger yield.

The amount of collected positrons is linearly proportional to $\Delta p/p$ and does not influence the optimum momemtum (fig. 2.26). The slight decrease of the polarization at the maximum as the momentum acceptance increases, corresponds to accepting smaller momentum positrons with smaller polarization and higher population.
Obviously, the larger the momentum acceptance, the better the performances of a polarized positron source.

5 Optimized polarized positron source

5.1 Target thickness

The target thickness has an important role to play as the electromagnetic shower increases with the amount of atoms (fields) encountered. However, secondary particles constituting the potential positron source have lower energies and may not exit the target if its thickness is too large. Therefore on optimum thickness depending

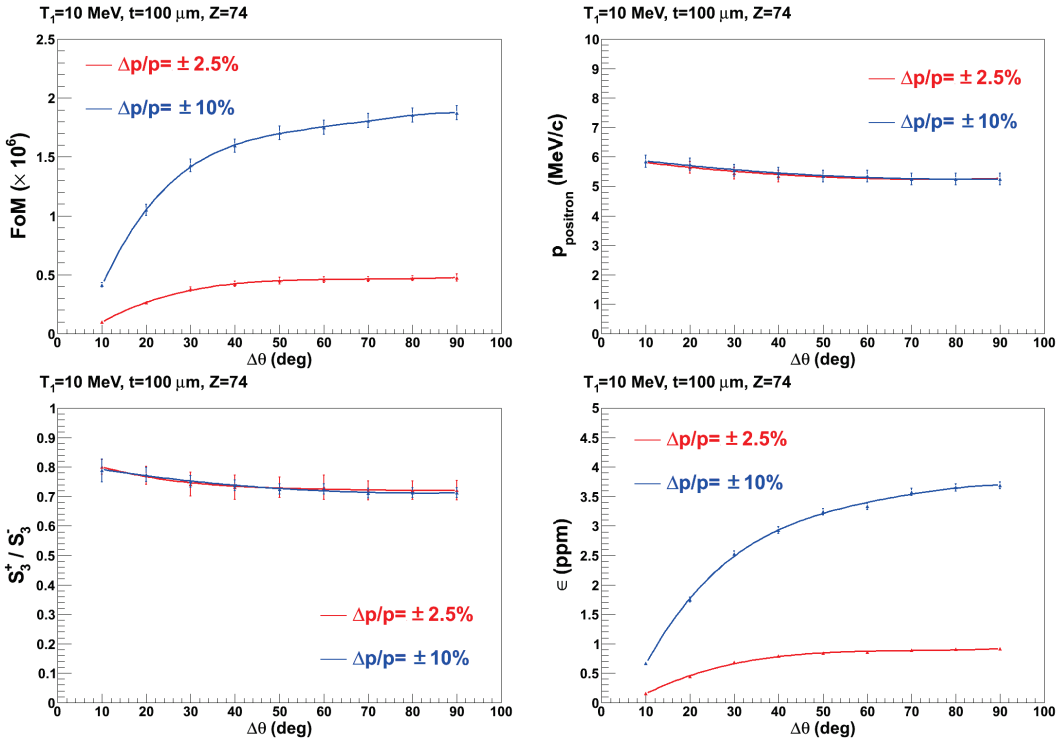

Figure 2.24: FoM (upper left), optimum positron momentum (upper right), positron longitudinal polarization (lower left) and positron production efficiency (lower right) at optimum as a function of the forward angular acceptance of an interface system. Curves are shown for a 10 MeV electron beam at perpendicular incidence on a 100 μm tungsten target and two different momentum acceptances.

on the incoming electron energy is expected.
Figure 2.27 (upper left) shows the target dependency of the optimum FOM for at 10 MeV incident electron beam at perpendicular incidence on a tungsten target. The combination of primary electrons bremsstrahlung and of the energy loss of secondary particles leads to the expected maximum at 1.3 mm for the considered example. Depolarization effects lead to the observed decrease of the optimum momentum (fig. 2.27 upper right). These effects remains however small, as can be inferred from the comparison of the optimum thicknesses maximizing the yield (fig. 2.27 lower right) on the one hand, and the FoM on the other hand: 1.5 mm and 1.3 mm, respectively. Accordingly, the average polarization at the optimum momentum is weakly depending on the target thickness.

The heat loss might be an issue for an efficient positron source. For instance, the fusion point of tungsten is 3695 K but the tungsten still evaporates even if the temperature of the target is kept below that limit: at 3100 K a tungsten target would lose 10 % of its mass in 1 hour or in 24 hours at 2700 K, according to the tables of Langmuir and Jones [71] on the evaporation rate of tungsten filaments under Joule effect. An experimental test on a tungsten foil 5×5 cm^2 and 50 μm thick with a 20 mA electron gun intended to weld metal pieces demonstrated a sustainable power deposit of 2 kW/cm^2 [72]. However, this limit corresponding to a thin foil under perpendicular incidence can be surpassed if the incident beam angle θ_i

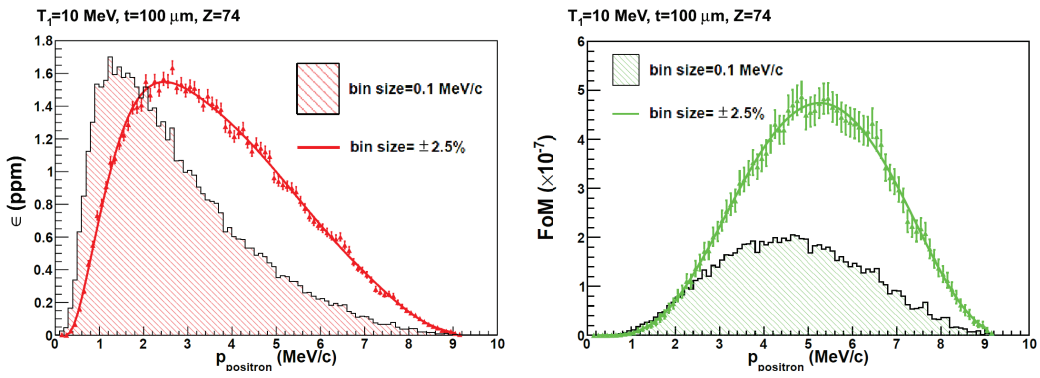

Figure 2.25: Momentum distributions of the forward positron yield and FoM integrated over angles for a momentum collection acceptance of $\pm 2.5\%$.

is reduced [72]. Because of the $1/\sin(\theta_i)$ magnification factor, the equivalent target length seen by the beam corresponds to smaller target thickness. The energy deposit of secondaries is also reduced because of the transverse size of the target. The beam spot size is larger on a tilted target for equivalent transverse beam sizes. These effects lead to smaller energy deposit which were shown to originate essentially from ionization effects [73]. A new optimization scheme can then be developed involving the same quantities normalized to the power deposit. This would however involve many other technological characteristics of the target (mechanical design, cooling power...) which are not the scope of this work.

5.2 Electron beam energy

The incident electron beam energy is the last physics parameter to be considered characterizing a polarized positron source. Its choice clearly depends on the capabilities of the electron accelerator and the focus is here on the energy range accessible with the CEBAF injector as is or after the 12 GeV upgrade. The higher the beam energy, the better the performances of a polarized positron source, as a consequence of the large increase of the positron yield and the focusing of secondary particles. Figure 2.28 gives the optimized parameters of a polarized positron source as a function of the electron beam energy. For each energy, the optimum thickness was determined at a momentum acceptance of ± 10 % in respect to the optimum momentum and an angular acceptance of 10° (fig. 2.28 lower). The optimum FoM and positron momentum, and the average polarization and efficiency at that optimum are then determined for the optimum thickness. The evolution of the FoM is dominated by the evolution of the yield and the average polarization is almost constant over the considered energy range. The optimum positron momentum is about half of the incoming electron energy (fig. 2.28 upper right). Over the full energy range studied here, an efficient polarized positron source can be obtained with a high polarization level.

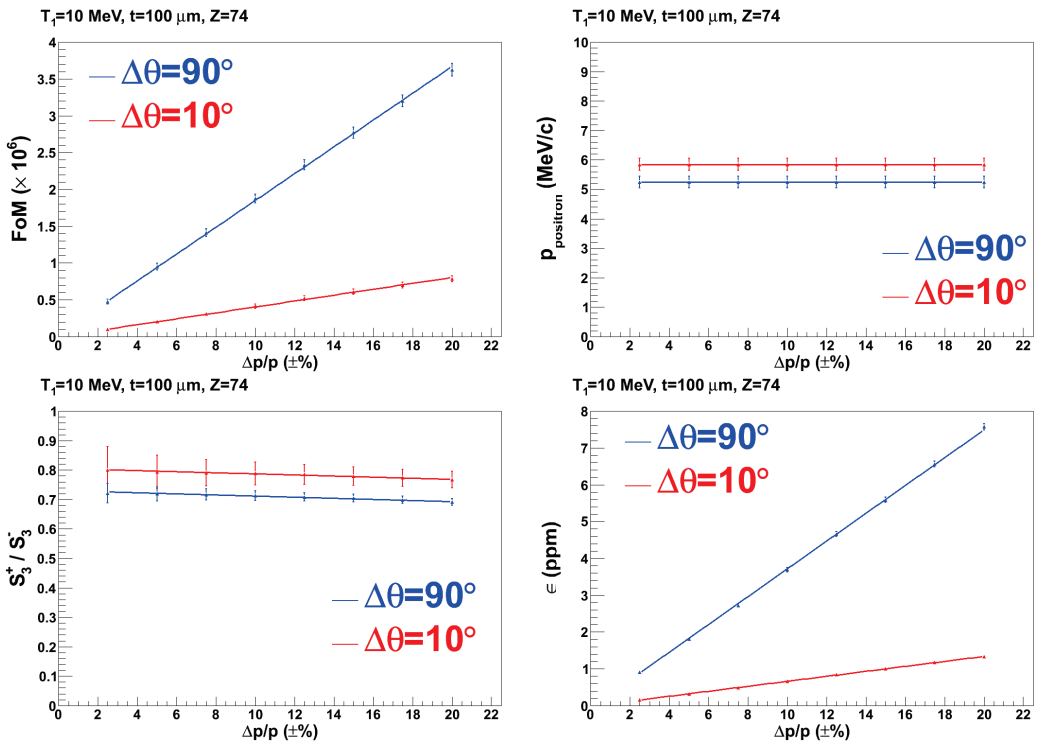

Figure 2.26: FoM (upper left), optimum positron momentum (upper right), positron longitudinal polarization (lower left) and positron production efficiency (lower right) at optimum as a function of the forward angular acceptance of an interface system. Curves are shown for a 10 MeV electron beam at perpendicular incidence on a 100 μm tungsten target and two different angular acceptances.

6 Conclusion

The bremsstrahlung of longitudinally polarized electrons has been shown to be a potentially efficient scheme to serve as a source of polarized positrons. Average longitudinal polarization transfer of 75 % over the energy range of the CEBAF injector can be expected with typical production efficiencies ranging from 10^{-6} up to 10^{-3}. Together with the today capabilities of the CEBAF polarized electron source (~1 mA), this would lead to polarized positron beam currents from 1 nA up to 1 μA, suitable for physics experiments into the different experimental halls of JLab. These figures can certainly be improved with an appropriate and refined collection system, assuming the achievement of a high power target.
Following the same concept of previously demonstrated polarized positron source techniques, a two target system where circularly polarized photons are first produced and then create polarized e^+e^- pairs in a second production target could have been also addressed. Using the bremsstrahlung technology in such a context would require a very bright photon beam that may be obtained from the channeling of ultra-relativistic electrons inside a crystal [70]. Electrons propagating in the vicinity of the crystal axis present some characteristics of the trajectories of electrons in a magnetic wiggler with a periodicity of several times the atomic separation distance. This atomic wiggler allows for a high flux of collimated photons. While this scheme

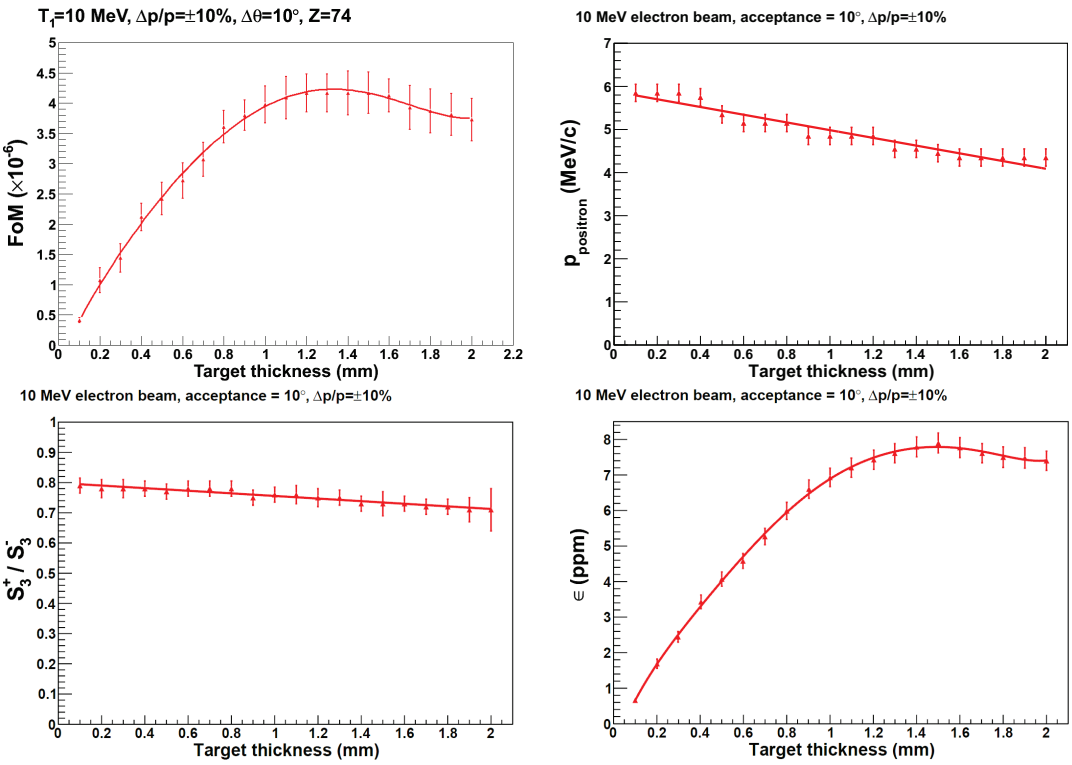

Figure 2.27: FoM (upper left), optimum positron momentum (upper right), positron longitudinal polarization (lower left) and positron production efficiency (lower right) at optimum as a function of the forward angular acceptance of an interface system. Curves are shown for a 10 MeV electron beam at perpendicular incidence on a 100 μm tungsten target, an elementary momentum acceptance of $\pm$10 % and an angular acceptance of 10°.

was studied in the context of the ILC, the required electron beam energies are too high to be considered for CEBAF purposes.
Nevertheless, the elementary physics of polarization transfer in the pair creation process has been shown to be largely not understood in their most currently used prescriptions. A novel theoretical approach motivated by the present studies appears to bring the necessary knowledge of these phenomena at low energies and would impact the high energy schemes if experimentally proved. This feature together with the experimental demonstration of the capabilities of the polarized bremsstrahlung technique are the main motivations of the PEPPo experiment (Polarized Electrons for Polarized Positrons) which is presented in the next chapters.

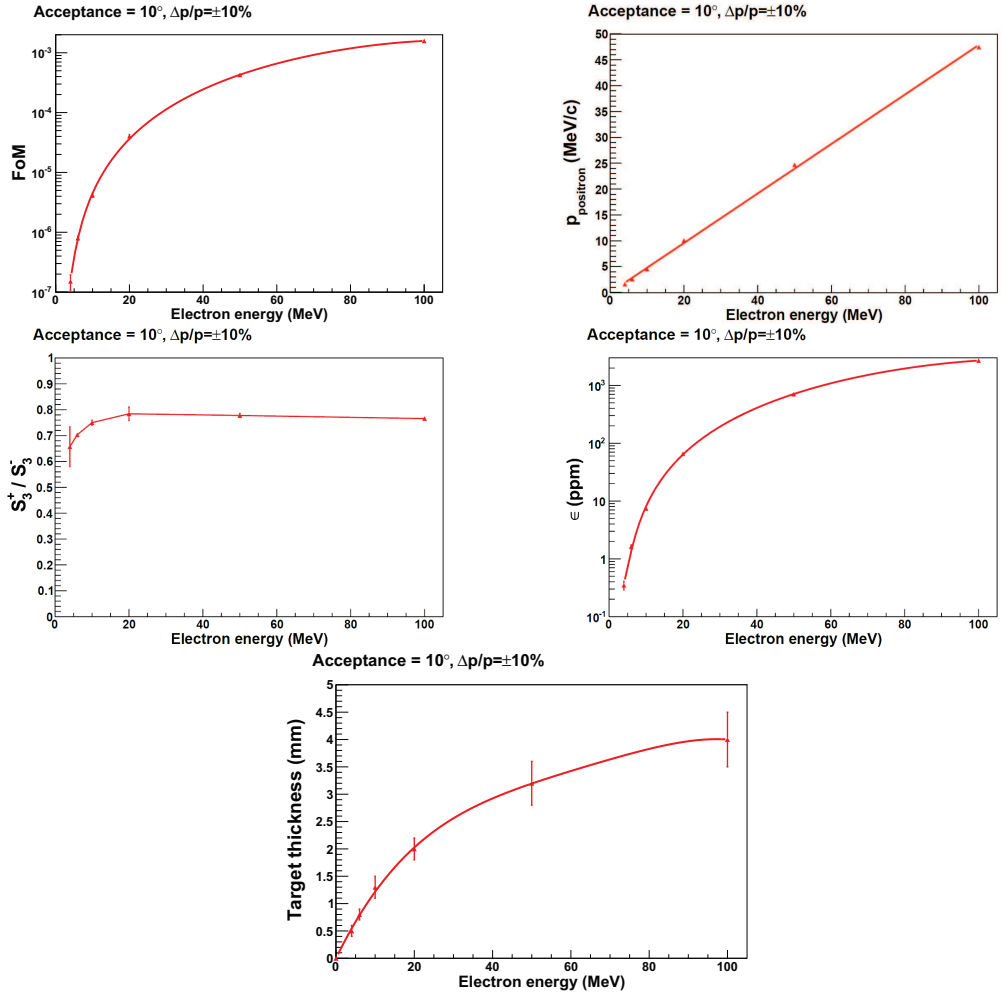

Figure 2.28: Incoming electron beam energy dependence of the optimum FoM (upper left), optimum positron momentum (upper right), positron longitudinal polarization (middle left) and positron production efficiency (middle right) at optimum, and of the optimum target thickness. Curves are shown for at a given incident electron beam energy at perpendicular incidence on a tungsten target of optimum thickness, and elementary acceptances of ±10 % in momentum and 10° in angle.

Chapter 3

PEPPo conceptual design

1 Introduction

The Polarized Electrons for Polarized Positrons experiment is planned at the CEBAF injector at the Thomas Jefferson National Accelerator Facility in Newport News, VA. In this experiment a modest energy (less than 10 MeV) beam of highly spin polarized electrons will strike a conventional pair production target foil. The resulting positrons will be collected and analyzed. A goal of this experiment is to demonstrate and characterize the transfer of polarization via bremsstrahlung and pair production processed in the production foil. It includes the measurement of the resultant positron yield and polarization as a function of positron kinetic energies for given incident electron beam conditions.

This chapter describes the CEBAF photoinjector and polarized electron beam which can be used for this experiment, and the simulations as functions of critical components of the apparatus to perform this experiment.

2 Polarized electron injector

Figure 3.1: Schematic drawing of the critical components of the CEBAF injector.

The CEBAF polarized electron photoinjector provides the drive beam for this proposed demonstration experiment. An electron beam with energy not more than 10 MeV and high polarization is sufficient. In addition, the low energy prevents neutron production [43] and the low current needed (1-10 μA) requires only a low power target. This section describes the critical components (Fig. 3.1) to produce, control and characterize the polarized electron beam.

2.1 Polarized electron source

The production of the polarized beam results from the excitation of a Gallium Arsenide (GaAs) semiconductor with circularly polarized laser photons. The polarization of the electrons comes from the optical pumping between the $P_{3/2}$ valence band and the $S_{1/2}$ conduction band levels. The spin of atomic electrons $m_s = \pm 1/2$ and the orbital angular momentum m_l (the orbital l corresponds to $2l+1$ values of m_l, hence $m_l = -1, 0, 1$ for the P valence band and $m_l = 0$ for the S conduction band) make a spin substate degeneracy with characteristic total angular momentum $m_j = m_l + m_s$ (two degenerated spin substates with $m_j = \pm 1/2$ are then possible for S and four for P with $m_j = \pm 3/2, \pm 1/2$). The minimum energy gap between $P_{3/2}$ and $S_{1/2}$ energy levels is 1.43 eV corresponding to the laser photon energy required for electron extraction. Right(Left)-circularly laser photons lead then to preferential $\Delta m_j = 1$ (-1) transitions between the valence and conduction bands. Besides, the transition $-3/2$ $(3/2) \rightarrow -1/2$ $(1/2)$ is three times more likely to occur than $-1/2$ $(1/2) \rightarrow -1/2$ $(1/2)$ as indicated by the Clebsh-Gordan coefficient on fig. 3.2.

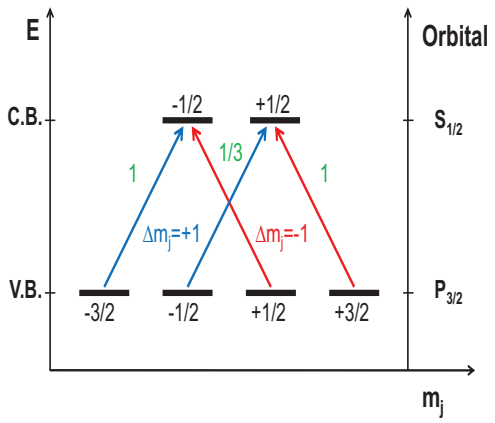

Figure 3.2: The transition of the atomic electron bound state in GaAs for a right(left)-circularly polarized laser photon are represented by the blue(red) arrows; relative amplitudes of preferential transitions are in green.

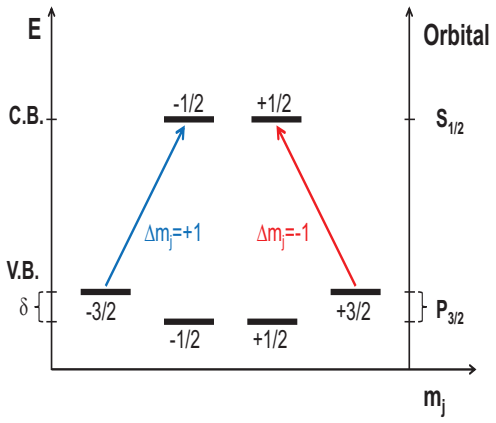

Figure 3.3: The transition of the atomic electron bound state in the strained GaAs/GaAsP for a right(left)-circularly polarized laser photon are represented by the blue(red) arrows; δ is the energy gap breaking the degenerated spin substates of $P_{3/2}$.

This results in a theoretical limit of 50 % polarized electrons. The polarization can be increased by shifting the $\pm 3/2$ above the $\pm 1/2$ substate energy levels. This degeneracy in GaAs may be removed by providing a strain to the crystal structure. A suitable strain at the atomic level is accomplished by growing alternating layers of a few nanometers thick of GaAs and GaAsP (phosphorous dopant). The resultant difference in GaAs lattice spacing provides a suitable strain that lifts the degeneracy. The difference between $-1/2$ and $-3/2$ states of $P_{3/2}$ is of the order of δ=0.1 eV and overcomes the 50 % limitation (Fig. 3.3). In reality depolarization of the electrons occur as they scatter during the photoemission process. So-called

superlattice strained GaAs photocathode provide polarization as high as 90 %.

Spin polarized photoemission ultimately depends upon the capability for electrons reaching the conduction band to leave the crystal. Generally, the electronic affinity of GaAs, E_a, prevents the conduction band electrons from leaving the crystal and pass to the vacuum (Fig. 3.4). The electronic affinity is about 4 eV for GaAs but may be reduced to zero if a layer of alkali such as Cesium (Cs) is applied at the GaAs surface. The oxidation of that layer with nitrogen trifluoride (NF_3) further reduce the electron affinity to become negative, allowing electrons reaching the conduction band to tunnel through the surface barrier potential and exit the crystal into the vacuum.

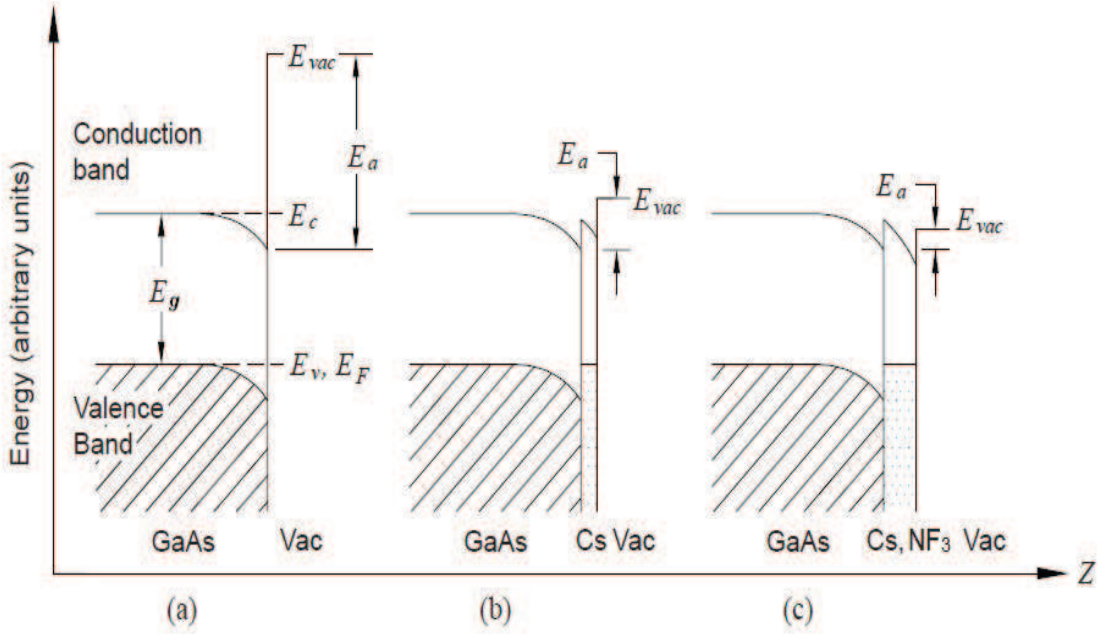

Figure 3.4: GaAs electronic affinity and band structure at the surface of the crystal; (a) Bulk GaAs; (b) GaAs with a layer of Cesium; (c) GaAs with a layer of Cesium and oxydant NF_3.

Quantitatively, the number of electrons extracted $q_{extracted}$ from the GaAs photocathode per laser photon N_γ is termed the quantum efficiency (QE)

$$QE = \frac{q_{extracted}}{N_\gamma} \tag{3.1}$$

or in terms of incident laser power P_γ and photon energy $h\nu$ as

$$I_e = QE\frac{P_\gamma}{h\nu}\,. \tag{3.2}$$

The photocathode is illuminated by a fiber-based laser which consists of three stage components; first, a gain-switched fiber-couple 1560 nm diode seed laser synchronized to the accelerating cavity radio-frequency signal, followed by a ErYb-doped fiber amplifier to increase the power at 1560 nm and ultimately a periodically poled lithium niobate (PPLN) frequency doubler which results in 780 nm suitable to optically pump the spin polarized state of the superlattice GaAs/GaAsP photocathode. Optical pulses with duration of about 40 ps are directed by mirrors and

through polarization controlling optics through a vacuum beam line window and focused to about 0.5 mm spot on the photocathode. The linearly polarized laser light is converted to either left/right circular polarization by an electro-optic Pockels cell which can set the laser (and electron) helicity at nearly 1 kHz. In addition, optical quarter-wave plate may be inserted/retracted to change the overall sign of the laser helicity.

The photocathode itself is fixed in the cathode electrode of the high voltage photogun at a short distance in front of a grounded anode electrode. Circularly polarized laser light illuminating an activated photocathode will photoemit electrons which are accelerated across the cathode/anode electrode gap thus attaining the energy of the high voltage power supply. These semi-relativistic electrons emitted synchronously with the accelerator radio-frequency have an initial bunch length comparable to the optical pulse length, are 130 keV (semi-relativistic) and form the basis for the electron beam.

2.2 Electron beam energy and measurement

The beam energy is defined by a sequence of electron acceleration. Electrons emitted from the photocathode are accelerated across a potential gap of 130 kV sustained by an external high voltage power supply. All subsequent acceleration is by radio-frequency cavities with a fundamental frequency of 1497 MHz, the same as the time structure produced at the source. The first cavity is a room temperature 5-cell graded-beta cavity constructed from copper which accelerates the electrons to 500 keV. Acceleration to higher energy is accomplished using two 5-cell niobium cavities, referred to as a quarter cryounit. Power is distributed from high power klystrons in a ground level service building, into the accelerator enclosure via a RF waveguide under vacuum and through a ceramic vacuum window to the cavity itself. The power to each cavity is controlled by a gradient setpoint and monitored by a gradient readback. These cavities are submersed in a bath of liquid helium and become superconducting which allows for continuous operation compatible with the 100 % duty factor electron beam. The current beam energy at this level is 5 MeV but can be accelerated by increasing the two niobium cavity gradients. The maximum stable accelerating gradients achieved were 8.4 MV/m and 6.1 MV/m [44]. Each cavity has an effective length of 0.5 m indicating a total energy of 7.25 MeV is achievable by the cryounit. In summary, the total electron beam can attain a maximum beam energy of about 7.75 MeV. To precisely know the beam energy, a momentum spectrometer is used. The relation between momentum, magnetic field and deflected angle is given by:

$$\frac{pc}{e} = \frac{\int Bdl}{\theta}, \tag{3.3}$$

where θ is the deflection angle in radians and $\int Bdl$ is the integrated magnetic field along the deflected orbit. Experimentally the bend angle is determined by two quadrupoles which define the incident beam direction and a scanning wire diagnostic (Harp) which defines the deflected beam direction through a dipole magnet of known magnetic profile. The positions of these elements are listed in table 3.1. The two quadrupoles (Q1 and Q2) are coupled to viewers. The position of the beam is

Component	z (m)	x (m)	y (m)	Yaw (deg)
Q1	0.0000	0.0000	0.0000	
Dipole	1.7513	0.0139	0.0002	14.905
Q2	6.1079	0.0000	0.0000	
Harp	4.6543	1.6760	-0.0005	

Table 3.1: Position survey of the spectrometer components compared to the position of the first quadrupole Q1 which defines the electron reference path with Q2; the dipole and the harp represent the spectrometer arm.

estimated to be centered on the quadrupole centerline if the beam position on the viewers does not change when the quadrupole fields are modified. The position of the spectrometer elements are surveyed with a design tolerance of 0.25 mm.

The spectrometer arm angle is surveyed at 29.97°. According to eq. 3.3, an integrated field of 14388.5 G.cm is necessary to deflect a 7.75 MeV (corresponding to a momentum of 8.245 MeV/c) electron beam into the spectrometer arm. The

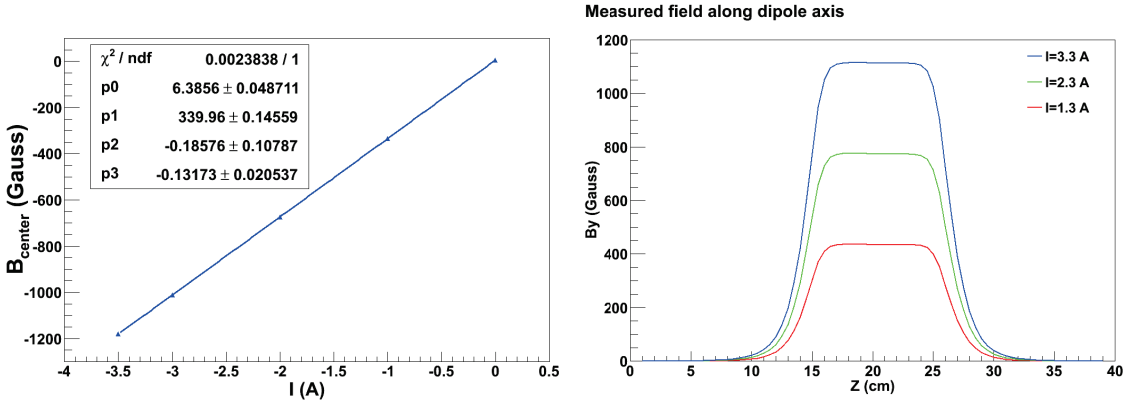

Figure 3.5: Magnetic field at the center of the magnet (left) and along the axis of the magnet (right) for different currents.

core field of the spectrometer dipole is measured with a NMR probe for currents between 0 and -3.5 A (Fig. 3.5). The current/field correlation is not linear and can be better estimated with a polynomial function $B = 6.38 + 339.96I - 0.18576I^2 - 0.13173I^3$. A three dimension magnetic field map is also realized with a Hall probe (more efficient for fields outside the core), measuring the field along axes collinear to the magnet direction, fringe field included. The dipole current corresponding to the integrated field of 14388.5 G.cm along the path of the electron beam can be calculated. The electron path in the dipole can be known by small iterations of the deflection corresponding to the field at a given position. In the present dipole configuration, with a yaw of 14.905°, a current of 3.351 A is necessary to match the integrated field of 14388.5 G.cm along the electron path. For the implementation of PEPPo, the dipole might be rotated to a yaw of 0°. Geometrically, the electron beam in the spectrometer would go through a longer section of the dipole, requiring less current to reach the same integrated field as before. A calculation determines that a current of 3.300 A would be sufficient for the integrated field of 14388.5 G.cm.

The precision of the beam momentum is determined by the accuracy of the bending angle and the determination of the dipole field. The bending angle precision is determined by:

- the positions of the quadrupoles is surveyed with a 0.25 mm design tolerance and the electron beam going through the center of the quadrupoles is estimated to be ~ 5 mm, resulting in a $\pm 0.01^\circ$ precision as the quadrupoles are 6.427 m apart;
- the stray field due to the natural earth field is measured at 350 mG and could be responsible in the beamline for a deflection between the quadrupoles, representing an other 0.07° uncertainty for a 7.75 MeV electron beam;
- for the spectrometer arm, the harp measures the beam position with a 0.05 mm precision and its position is known within 0.25 mm. The position of the beam at the exit of the dipole is not monitored. The spectrometer arm is 3.30 meter long with a beam pipe radius of 12.7 mm. Most of the arm is covered with μ-metal preventing the effects of the stray field (350 mG $\rightarrow$ 10 mG). There is a possible $\pm 0.23^\circ$ incident angle in the spectrometer arm.

The total uncertainty on the bending angle θ is $\pm 0.31^\circ$. The dipole field was surveyed with a precision is given by:

- the variation of the field against the time = 0.00 %;
- the reproducibility, the variation of the field when the magnet is turned off and on is 0.04 %;
- the vertical field variation is 0.02 %;
- the probe precision is better than 0.1 %.

The total field precision is estimated at $\triangle \int B.dl / \int B.dl = \pm 0.16$ %. The uncertainty on the bend angle and the field measurement can be added quadratically, leading to the total precision of the momentum

$$\frac{\triangle p}{p} = \sqrt{\left(\frac{\triangle \int B.dl}{\int B.dl}\right)^2 + \left(\frac{\triangle \theta}{\theta}\right)^2} = 1.00\,\% . \tag{3.4}$$

2.3 Spin rotators and Mott electron polarimeter

The control and the knowledge of the electron beam polarization is crucial to polarized dependent experiments. The electron beam polarization, parallel or anti-parallel to the beam momentum of electrons emitted at the photocathode, is defined by

$$\mathrm{P} = \frac{N_\uparrow - N_\downarrow}{N_\uparrow + N_\downarrow} \tag{3.5}$$

where $N_\uparrow(N_\downarrow)$ is the number of electrons with a spin $\frac{\hbar}{2}(-\frac{\hbar}{2})$ aligned(anti-aligned) with the beam direction.

The overall sign (helicity) of the photo-emitted electrons are fundamentally controlled by the defined sign of the circular laser polarization. Typical methods to do this (Pockels cell, wave plate retarders) are described in the earlier section. Once the electron beam is formed the mean value of the electron polarization is conserved, however the orientation in space may be transformed by rotations using electro-magnetic fields of either Wien filters or solenoids.

Wien filters (Fig. 3.6) present crossed electric and magnetic fields which do not alter the electron beam trajectory but rotate the polarization on an axis transverse to the beam momentum (horizontally or vertically). The magnetic field rotates the beam and its polarization by an angle ϕ_{spin} as

$$\phi_{spin} = \int B.dl/mc\gamma^2\beta \tag{3.6}$$

where β is the velocity and γ the Lorentz factor of electrons. The polarization can be rotated independently from the beam direction as a perpendicular electric field E evens out the Lorentz force:

$$\vec{F} = e\left(\vec{E} + \frac{\vec{\beta}}{c} \wedge \vec{B}\right) = \vec{0}\,. \tag{3.7}$$

The Wien filter requires that $|E| = \beta|B|$

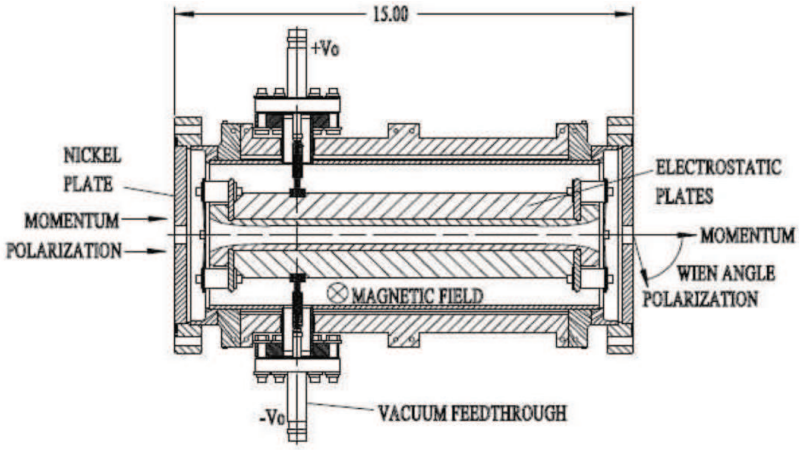

Figure 3.6: Wien filter in which an electric $\vec{E}$ and magnetic $\vec{B}$ field are applied to rotate the particles spin with an angle θ while preserving their momentum from Ref. [45].

Solenoids present a longitudinal magnetic field which similarly does not deflect the electron beam trajectory but rotate the polarization about the axis of the beam momentum

$$\phi_{spin} = e/2p \int Bdl\,. \tag{3.8}$$

By sequencing a vertical Wien filter with a spin precession of $\pm\pi/2$, followed by 2 solenoids ($\pm\pi/4$ each), followed by a horizontal Wien filter ($\pm\pi/2$) the three successive rotations about the X, Z and Y axis may set the polarization to any orientation in 4 π.

A Mott electron polarimeter on a dedicated beam line following the cryounit may be used to measure orthogonal components of the electron polarization normal to the beam direction. The polarimeter relies on the interaction of the electron spin with the nuclear potential of an unpolarized target (Fig. 3.7 left).

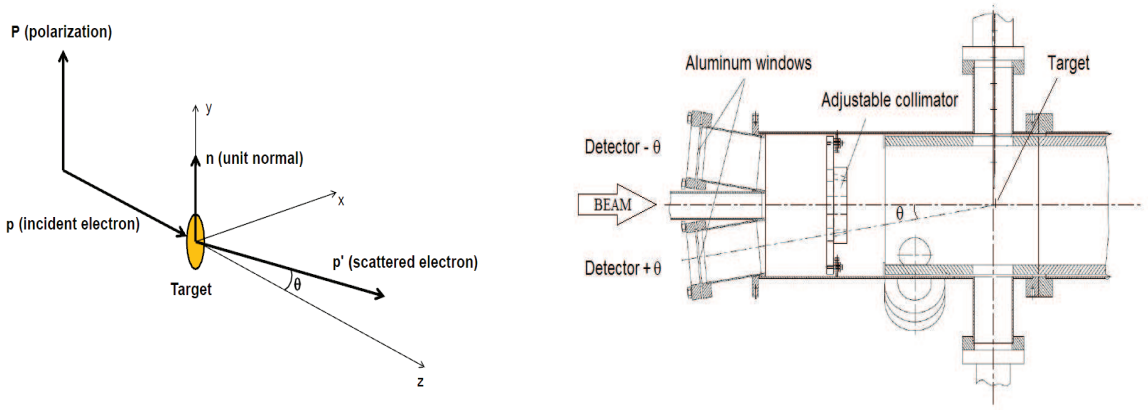

Figure 3.7: Mott scattering for a transversely polarized beam (left) and the Mott schematic apparatus with detectors at $\pm 173^{\circ}$ compared to the beam direction (right).

The magnetic field provided by the electron motion in the nucleus electric field and the electron magnetic moment (related to the spin) results in a spin-orbit coupling in the electron scattering potential and leads to a spin dependent component in the Mott cross section

$$\frac{d\sigma}{d\theta} = \frac{d\sigma_0}{d\theta}\left[1 + S(\theta)\vec{P}.\hat{n}\right] \tag{3.9}$$

where $S(\theta)$ is the Sherman function and the unpolarized cross section is

$$\frac{d\sigma_0}{d\theta} = \left(\frac{Ze^2}{2mc^2}\right)^2 . \frac{(1-\beta^2)(1-\beta^2\sin^2(\theta/2))}{\beta^4 \sin^4(\theta/2)} \tag{3.10}$$

and $\vec{n}$ is the unitary vector normal to a plane defined by the incident and scattered electron directions, respectively $\vec{p}$ and $\vec{p'}$ as

$$\hat{n} = \frac{\vec{p} \times \vec{p'}}{|\vec{p} \times \vec{p'}|} . \tag{3.11}$$

The transverse component of the electron polarization $\vec{P}$ to the scattering plane (collinear with $\hat{n}$) generates a contribution to the polarized Mott cross section. The asymmetry A_M of electrons with opposite transverse polarization $N^{\uparrow}$ and $N^{\downarrow}$ and scattering at two (symmetric) angles ($\pm\theta$) with the electron beam direction is given by

$$\mathrm{A_M} = \frac{1-r}{1+r} = PS(\theta) \tag{3.12}$$

with

$$r = \sqrt{\frac{N^{\uparrow}_{+\theta} N^{\downarrow}_{-\theta}}{N^{\downarrow}_{+\theta} N^{\uparrow}_{-\theta}}} . \tag{3.13}$$

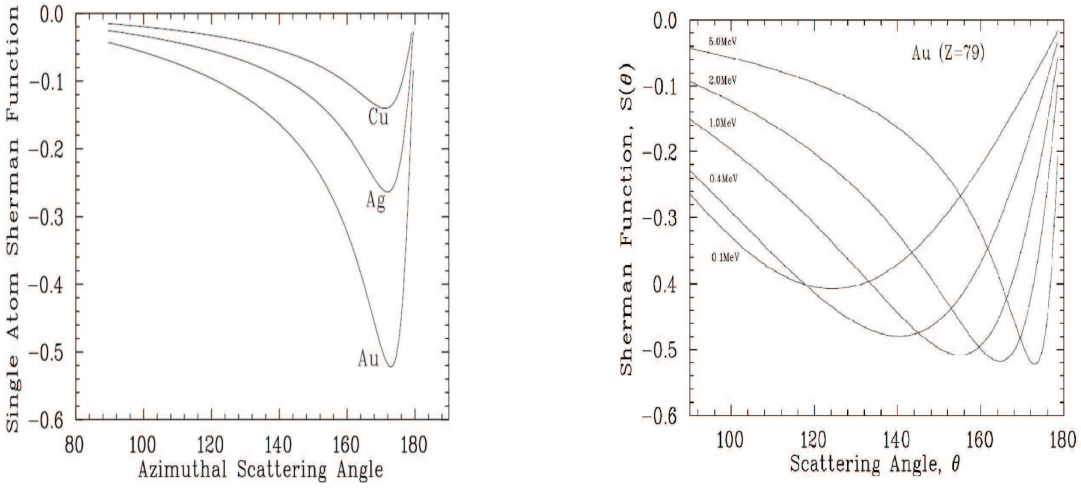

Figure 3.8: Sherman function for different materials (left): copper (Z=29), silver (Z=47) and gold (Z=79) and for different beam energies (right).

The Sherman function determines the experimental asymmetry or analyzing power of the polarimeter and can be maximized with a) the atomic number Z (spin-coupling increases with large Z) of the target (fig. 3.8 left), b) the electron beam energy (fig. 3.8 right) and c) the scattering angle θ. For a 5 MeV electron beam, the Sherman function is maximized at a scattering angle of $\pm 173°$. Thin gold targets (ranging from 0.1 μm to 5 μm) are used to minimize multiple scattering. The polarimeter measures a transverse polarization, so in order to measure the longitudinal component of the beam polarization, the electron spin needs to be redirected with a Wien filter.

3 Concept of PEPPo Layout

The PEPPo conceptual layout is based on the modification of the electron beam line to include a section dedicated to positrons. This new line is meant to be as less invasive and as much compact as possible. It can take advantage of the existing dipole used for the spectrometer and the Mott polarimeter. It requires a new vacuum chamber with an additional spigot on the other side of the electron beamline. The new line would be instrumented with various diagnostic devices and can be decomposed in three regions of interest: the positron production, the collection of positrons and finally the polarimetry (Fig. 3.9).

This conceptual layout is largely inspired from the E166 experiment as the particle energy range (<10 MeV) and measurement requirements are very similar. The electron beam would be driven from the existing electron line to the positron production chamber by steering magnets. At this point, a ladder would be installed and support several production foils, a viewer to ensure that the electron beam spot is correctly placed at the center of the conversion foils and also an empty slot so that electrons can go through the whole positron line and assess the rest of the equipment. A first solenoid (S1) is meant to collect the large angular distribution of positrons right after the target. The positron energy is selected by a 2 dipole spectrometer

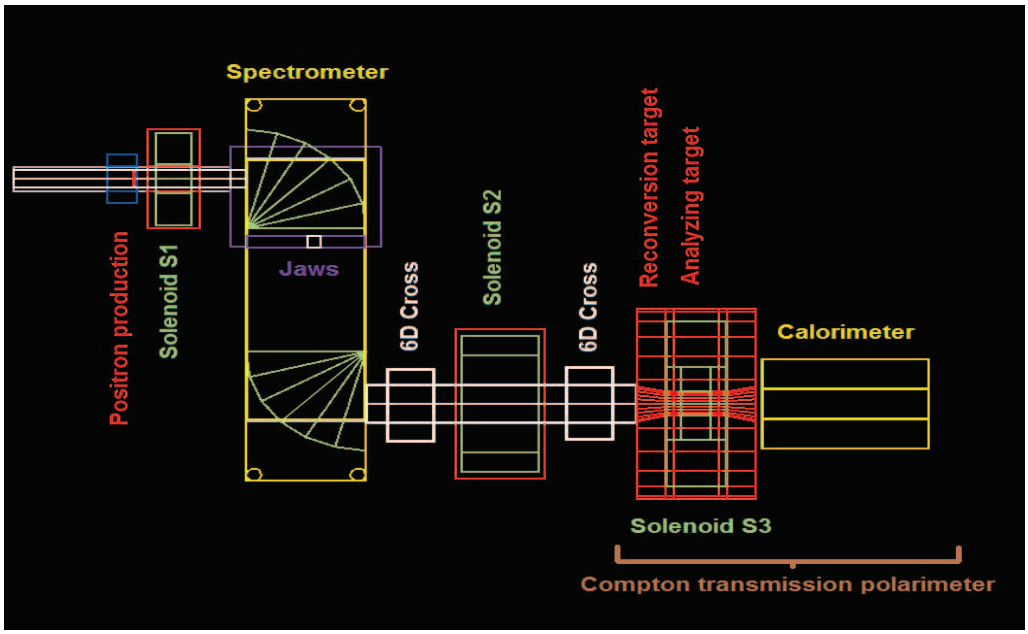

Figure 3.9: Positron segment that could be added to the existing injector beamline.

each bending the particles of 90 degrees associated with a collimator referred to as jaws in between the two dipoles. A section of beamline at the exit of the spectrometer could be composed of two 6 dimensional crosses allowing the installation of ladders. These ladders can be equipped with a viewer, to monitor the particles that go through the spectrometer, a Faraday cup to measure the current and an empty slot. A second solenoid S2 could collect particles, canceling the spectrometer particle spread, steering them to the Compton transmission polarimeter.

This Compton transmission polarimeter requires the radiation of bremsstrahlung photons by positrons in a target very similar to the positron production target. An analyzing target, much thicker than the others by at least one order of magnitude, is polarized by a third solenoid (S3). The asymmetry in the photons transmission resulting from a polarization flip of the analyzing target is characteristic of the lepton polarization. Analyzing a well defined electron beam is a first step to calibrate the polarimeter for positrons. A calorimeter composed of a 3×3 crystal array detects the photons after the analyzing target.

The next sections review the role played by the 3 targets of this layout and discuss the transport system between the positron production and the polarimetry.

4 Targets

4.1 Production target

For simplicity, a monochromatic electron beam with a kinetic energy of 8 MeV is considered, comparable with the capability of the quarter cryounit. Anticipating an important power load in the production target, the positron yield is expressed for a 1μA electron beam. The polarization of the electron beam is fixed at 85 %. For example, a large variety of target thicknesses (0.25-2mm) is presented on fig.3.10 for

the three kinds of particles of interest. The current, mean energy, mean polarization

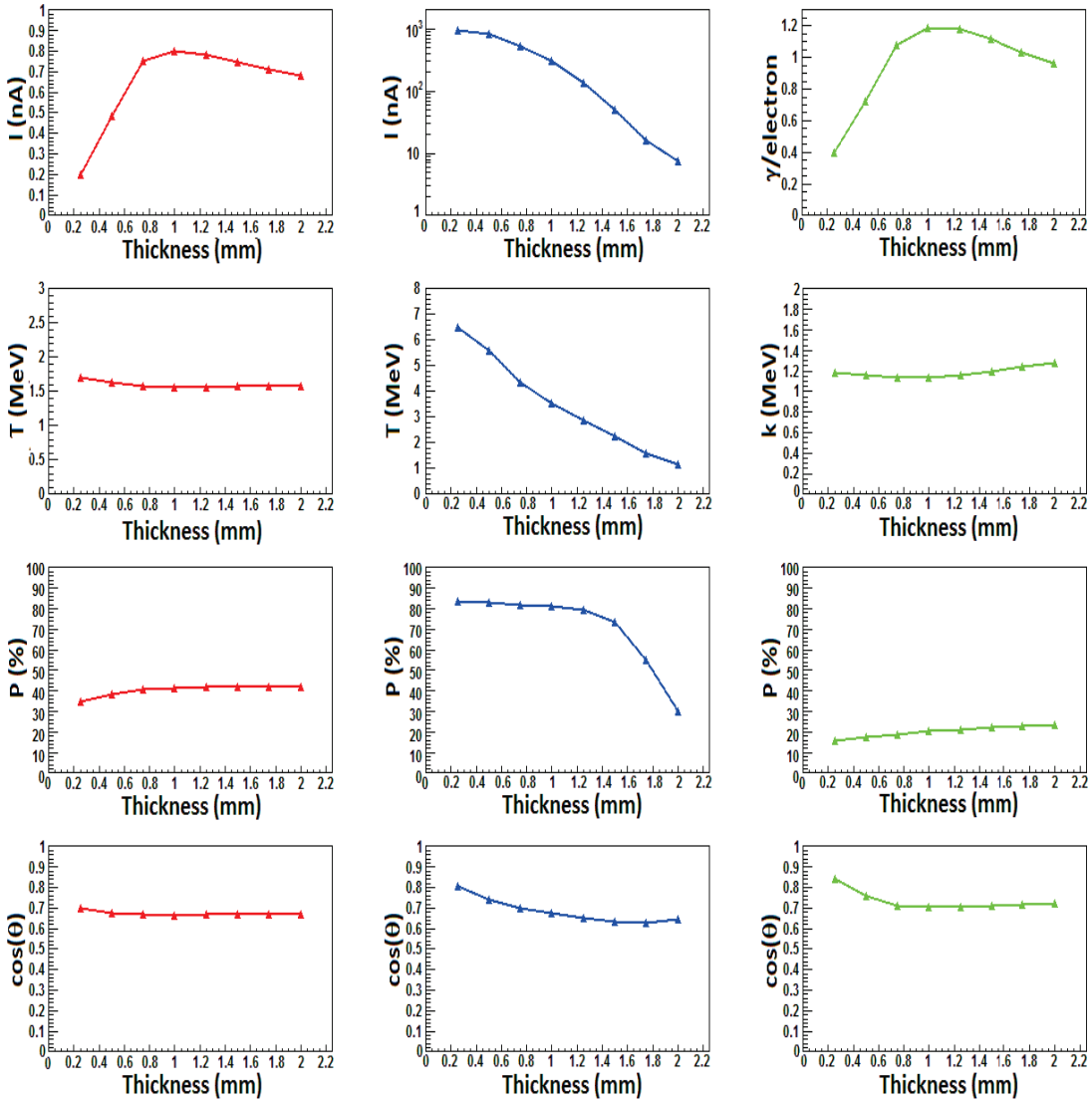

Figure 3.10: Positron (red), electron (blue) and photon (green) mean distribution after a tungsten target hit by a 1 μA electron beam of 8 MeV

and mean scattering angle after the production target are shown. The current is integrated over all energies and the evolution of positron production as a function of the target thickness is as expected reaching a maximum at 1 mm. The study of the electrons after the target is interesting because of the background it will produce in the rest of the line and the power deposit in the elements following the target. A 0.25 mm target thickness lets most of the electrons go through. A 2 mm target however drastically reduces the amount of electrons escaping the target more than 90 %, almost reaching the same order of magnitude of positron production. The photons produced per electron show that the target thickness maximizing production is the same for photons and positrons.
The positron and electron mean energy decreases with the target thickness, it however reveals that positrons escaping the target are produced in the last layers of the

target as the electron mean energy dominated by the beam electrons that have a mean energy which is lower than the positron one. A few millimeters of tungsten is sufficient to decrease the mean energy of beam electrons to ~ 1 MeV. The photon mean energy increases as the lower energy photons are more subject to Compton scattering and absorption.
The mean polarizations of positrons and photons increase as low energy particles carrying low polarization do not leave the target. The electron polarization drastically decreases for target thickness above 1.6 mm and even reaches a lower polarization than the positron one. This comes from the depolarization of the beam electrons present in much greater amounts than the pair creation electrons.
The mean scattering angle of positron is steady as the target thickness increases. Positrons in thicker targets are more likely to scatter but it tends to show that positrons created in the first layers, do not exit the target. The electrons and photons mean angles decrease as these particles do go through the whole target and not only the last bit. The optimum target thickness maximizing the figure of merit is mostly determined by the positron current as the polarization is steady. A 1 mm target should be picked in this case. A thinner target is also interesting to prevent depolarization effects and energy loss related modifications. A really thick target is also interesting to prevent background particles interfering with the measurements.

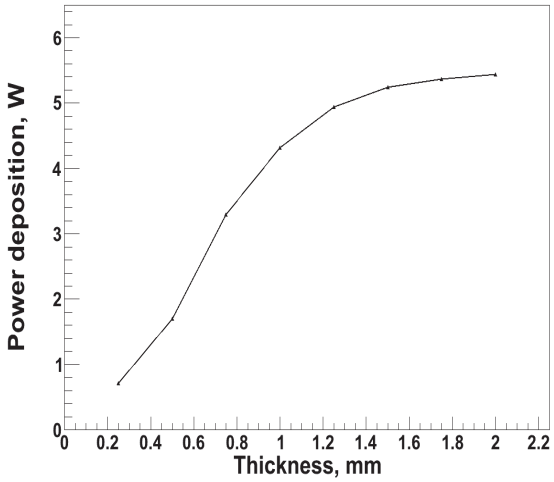

Figure 3.11: Power deposited as a function of the target thickness by a 1 μA electron beam of 8 MeV.

The power deposited in the target is shown in Fig. 3.11. The electron beam represents a total power of 8 W. In a 1 mm target, the beam power deposited has been simulated to be about half the total electron beam power. The power deposition saturates at ~ 6 W as part of the electron beam backscatters and also photons with high energy can go through larger distances in matter with a reduced energy loss.

PEPPo is intended to measure the produced positron polarization as a function of their energy (Fig. 3.12 left). The magnitude of the positron current is pA for simplistic acceptances in kinetic energy and acceptances corresponding to what is expected from the transport line between the production target and the polarimeter.

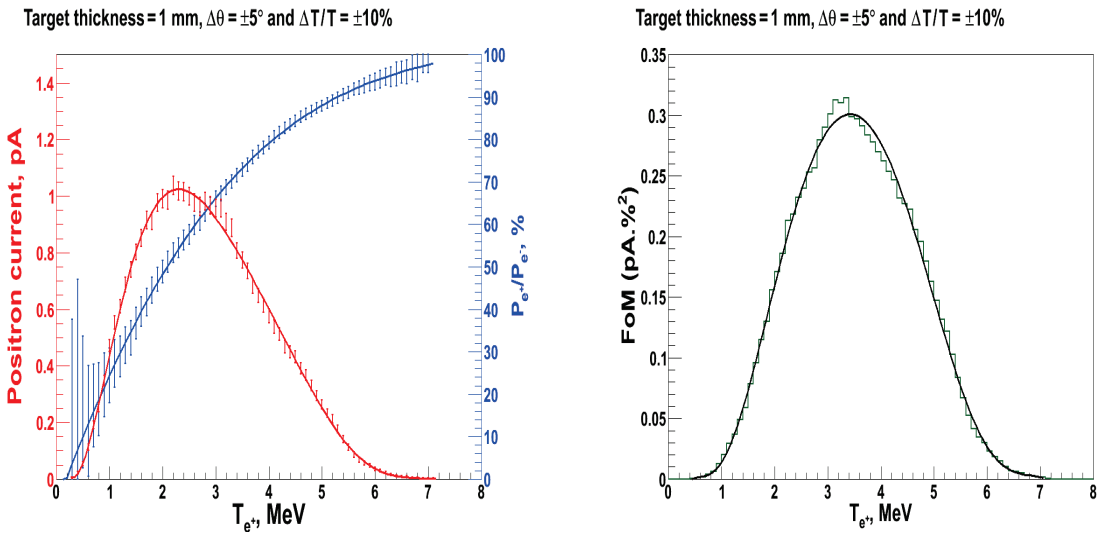

Figure 3.12: Positron polarization and positron production as a function of positron energy (left) and corresponding FoM (right) from the interaction of a $1\mu A$ electron beam with a kinetic energy of 8 MeV and a polarization of 85 %; simplistic acceptances in angles $\Delta\theta/\theta = \pm 5$ % and in kinetic energy selection $\Delta T/T = \pm 10$ %

The figure of merit (Fig. 3.12 right), shows that the most time efficient measurements are made between 2 and 5 MeV, where positron polarization ranges from 50 % to 90 % of the electron beam polarization.

4.2 Re-conversion target

As the first part of the Compton transmission polarimeter, polarized leptons produce polarized photons in a foil, the re-conversion target. The photons are then going through the analyzing target of the polarimeter. The degree of photon polarization depends on the lepton polarization to be measured. The re-conversion target is very similar to the production target. Before positrons, the electron beam could be used to calibrate the polarimeter and understand the relation between the signal received by the polarimeter and a well defined electron beam.

The target thickness that maximizes the photon figure of merit is calculated just like in the previous section. Angle acceptances can be implemented as only photons going through the analyzing target are useful. Three angular acceptances have been considered, 90, 10 and 4 degrees, respectively corresponding to the full photon production after the target, the analyzing magnet acceptance as used in the E166 experiment and as could be used if the re-conversion target is located in the cross after the second solenoid. Electron beams of different kinetic energies (2-8 MeV) have been used to understand the photon production (Fig. 3.13). The Compton transmission polarimetry relies on the figure of merit of the photons, calculated as number of photons per electron and the photon polarization normalized by the electron polarization squared. At 4 MeV, a 0.7 mm target is maximizing the FoM for an angular acceptance of 90 degrees. A target of 0.9 mm is more suited for smaller acceptances. The FoM of photons as a function of the target thickness is steady above 0.9 mm for 10° and 4°. There is however an order of magnitude between

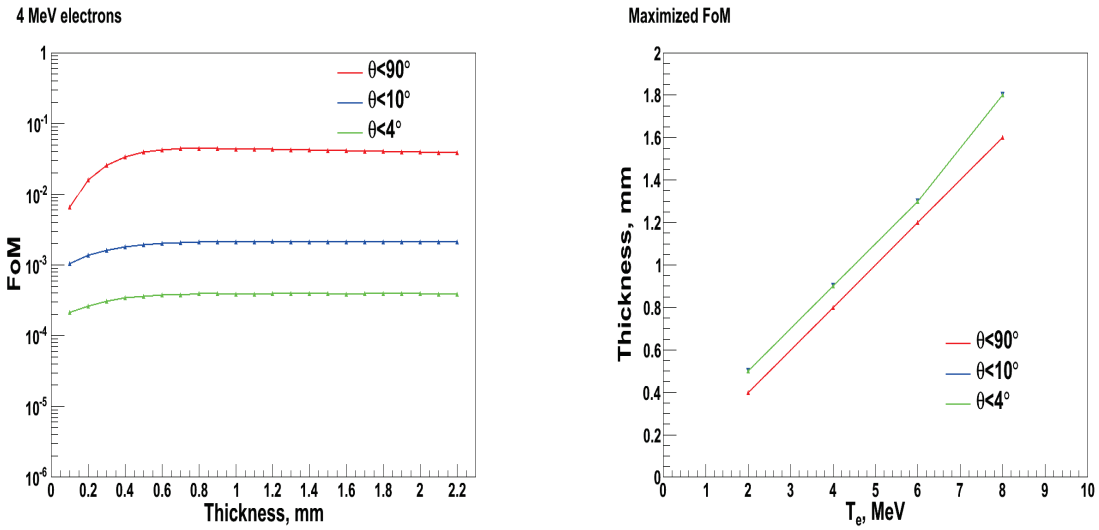

Figure 3.13: Photon FoM as a function of the target thickness for 4 MeV electrons (left) and optimum target thickness for any electron beam energy (right) for three different angular acceptances.

these angular acceptances. The optimum target thickness is represented on the right part of Fig. 3.13. A 1 mm target would optimize the FoM of 5 MeV leptons. Since the FoM does not decrease drastically for targets thicker than the optimized thickness, 1 mm is still acceptable for leptons between 2 and 5 MeV.

4.3 Analyzing target

Polarized photons created in the re-conversion target go through a polarized iron target. A solenoid (S3) magnetizes the iron. At saturation, the iron polarization can reach 8.52 %. The interaction of interest is the polarized Compton scattering. The differential cross section for the Compton scattering of circularly polarized photons (P_γ) from a longitudinally polarized electron target (P_t) can be written

$$\frac{d^2\sigma}{d\theta d\phi} = \frac{d^2\sigma^0}{d\theta d\phi}\left[1 + P_\gamma P_t A_C(\theta)\right] \tag{3.14}$$

where $d^2\sigma^0/d\theta d\phi$ is the unpolarized Compton cross section

$$\frac{d^2\sigma^0}{d\theta d\phi} = \frac{1}{2}\left(r_0 \frac{k}{k_0}\right)^2 \left[\frac{k_0}{k} + \frac{k}{k_0} - \sin^2(\theta)\right] \sin(\theta) \tag{3.15}$$

and $A_C(\theta)$ is the analyzing power of the Compton process

$$A_C(\theta) = \left[\frac{k_0}{k} - \frac{k}{k_0}\right], \cos(\theta) \Big/ \left[\frac{k_0}{k} + \frac{k}{k_0} - \sin^2(\theta)\right], \tag{3.16}$$

both quantities depending on the scattered photon energy (k) and angle (θ), and the incoming photon energy (k_0).

Compton transmission polarimetry takes advantage of the sensitivity of the Compton process to the absorption of circularly polarized photons in a polarized

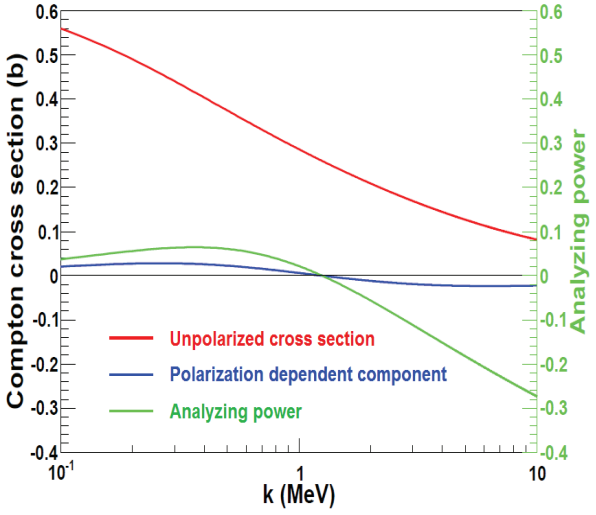

Figure 3.14: Total Compton cross section (red for unpolarized and blue for polarized) components and analyzing power (green).

target. This method, which involves a single detection device matching the size of the incoming beam, is intrinsically easy to implement and has been recently used successfully in experiments similar to PEPPo [39, 46]. Considering the simple case of a monochromatic parallel photon beam scattering off a polarized electron target with length L, the transmission efficiency characterizing the probability that a photon exits the target may be written

$$\varepsilon_T = \exp\left[-(\mu_0 + P_\gamma P_t \mu_1)L\right] \tag{3.17}$$

which assumes the loss of any photon interacting in the target and the dominance of the Compton process; μ_0 and μ_1 are the unpolarized and polarized Compton absorption coefficients

$$\mu_0 = \rho_e \int d\theta d\phi \, \frac{d^2\sigma^0}{d\theta d\phi}, \qquad \mu_1 = \rho_e \int d\theta d\phi \, \frac{d^2\sigma^0}{d\theta d\phi} A_C(\theta), \tag{3.18}$$

with ρ_e the electron density of the target. The total unpolarized Compton cross section (μ_0/ρ_e), the polarization dependent part (μ_1/ρ_e) and the Compton analyzing power (μ_1/μ_0) are shown in Fig. 3.14 as a function of the incoming photon energy. The magnitude of the cross section and of the analyzing power guarantee an efficient polarimeter over the energy range of this experiment. The measurement of the circular polarization of the photon beam is obtained from the number of transmitted photons for opposite beam helicities or polarized target orientations. The corresponding asymmetry is expressed as

$$A_T = \frac{N^+ - N^-}{N^+ + N^-} = \tanh(-P_\gamma P_t \mu_1 L) \tag{3.19}$$

from which the photon circular polarization is inferred according to

$$P_\gamma = -A_T / P_t \mu_1 L \,. \tag{3.20}$$

The associated statistical uncertainty is given by

$$\delta P_\gamma = \left[2N_\gamma\, P_t^2\, \mu_1^2 L^2 \exp\left(-\mu_0 L\right)\right]^{-1/2} \tag{3.21}$$

from which the optimized target length can be deduced

$$L = \frac{2}{\mu_0}\,. \tag{3.22}$$

In the 2-5 MeV lepton energy range of PEPPo, the optimized length varies between 6 and 11 cm considering the highest photon energy. This is comparable to the existing analyzing target used for the E166 experiment which length is 7.5 cm.

5 Transport

Major parts of the characterization equipment of the E166 experiment used in a similar energy range could be installed after the production region. The positrons produced at the production target are going through the transport system and tracked in the magnetic field down to the polarimeter. Two options are considered for transport after the collection solenoid (S1) after the production target and the two dipole spectrometer selecting particle energy and charge: a) one 6D cross allowing a position detector such as a viewer and a current monitor such as a Faraday cup followed by the Compton transmission polarimeter represented by the $NoS2ReconvTarget$ virtual detector (Fig.3.15); b) the second option is an arrangement with two 6D crosses allowing beam direction monitoring. A JLab solenoid (S2) between the crosses could collect positrons and control the beam waist. The polarimeter would sit where the $S2ReconvTarget$ virtual detector is located.

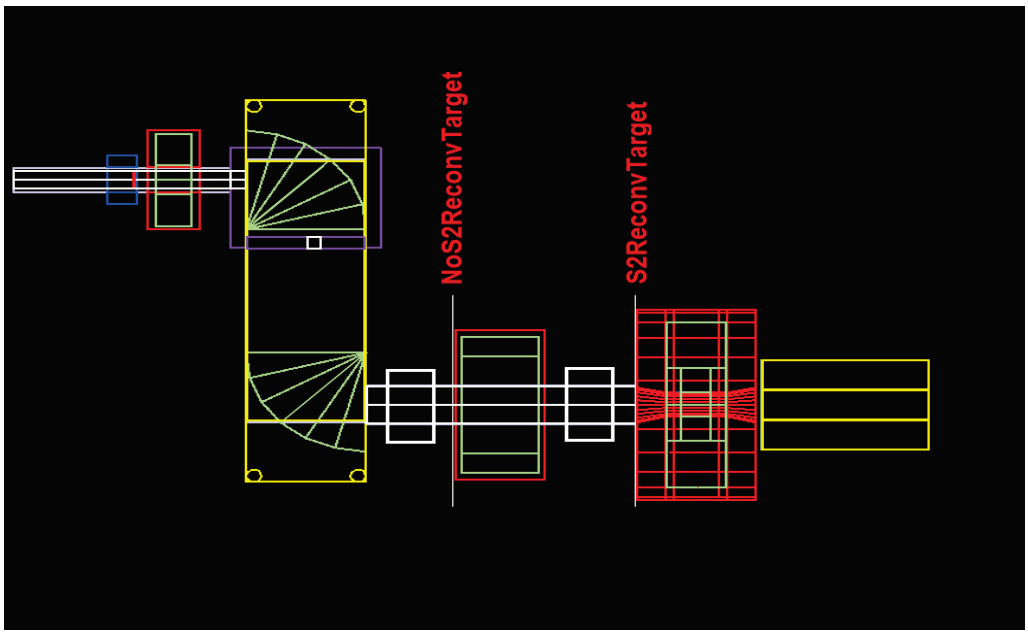

Figure 3.15: Schematic of the PEPPo transport system with virtual detectors "NoS2ReconvTarget" and "S2ReconvTarget", respectively located before S2 and S3

Geant4 simulations are aiming at the study of the two option scenarios and the determination of the setting points (I_{S1}, I_D, I_{S2}) maximizing the transmission of positrons from the production target to the polarimeter. The spectrometer current I_D, and the solenoid currents I_{S1} and I_{S2} can be studied separately.

The position and dimensions of the elements in the positron line are listed in table 3.2. The first solenoid right after the production target is collecting particles to increase the number of particles accepted in the spectrometer. The angular acceptance of the spectrometer vacuum chamber entrance from the production target is about 5°. Due to the low power considered, the electrons remaining from the initial beam after the production target can be dumped in the spectrometer vacuum chamber. The positrons are guided through the collimating jaws that select a slice of positron kinetic energy ($\Delta T/T \leq 10$ %). The positron energy selection is large enough to ensure a large amount of particles and an accurate polarization measurement for a given energy. As the particle spread at the exit of the spectrometer is expected to be important due to the large energy acceptance, the second solenoid S2 can help the positron transport through the two 6D crosses down to the polarimeter. The S2 solenoid is available at JLab and its inner radius can be extended from 19.05 mm to 38.1 mm. A radius of 38.1 mm is preferable to increase its angular acceptance.

Magnetic field maps of solenoids, calculated with Poisson/superFish, and of the spectrometer used and modelled by the E166 collaboration (MERMAID), were implemented in the simulation aiming at the optimization of the collection system. The solenoid fringe fields are simply added with the spectrometer dipole fields where the maps overlap.

Component	x (mm)	y (mm)	z (mm)	lx (mm)	ly (mm)	lz (mm)
Production target W	0	0	0	50	50	1
S1 solenoid bore	0	0	66.947	25.4	NA	86.36
Spectrometer entrance bore	0	0	189.544	18	NA	3
Spectrometer vacuum chamber	228.6	0	289.644	534.512	50	197.2
Jaws aperture	129.396	0	304.064	25	50	28.8
Spectrometer exit bore	463.55	0	-389.744	24.84	NA	3
1^{st} 6D cross	463.55	0	467.444	38	NA	152.4
S2 Solenoid	463.55	0	620.144	38.1	NA	150
2^{nd} 6D cross	463.55	0	771.344	38	NA	152.4
S3 Solenoid	463.55	0	872.344	25	NA	200
Re-conversion target	463.55	0	822.344	25	NA	1
Analyzing target	463.55	0	872.344	25	NA	75
Calorimeter	463.55	0	1122.344	180	180	280

Table 3.2: Position in x,y and z and dimensions lx, ly and lz of PEPPo elements as implemented in this conceptual design. Dimensions for cylindrical symmetric elements are lx for inner radius, ly is not applicable (NA) and lz for the length.

A trilinear interpolation method was used to calculate the field along the particle track. The field at position (x, y, z) of the particle is a combination of the 8 surrounding field values corresponding to the cubic mesh of the field map (fig. 3.16)

$$\begin{aligned} B = \quad & B_{0,0,0}(1-x)(1-y)(1-z) + B_{1,0,0}x(1-y)(1-z) \\ + \quad & B_{0,1,0}(1-x)y(1-z) + B_{0,0,1}(1-x)(1-y)z \\ + \quad & B_{1,1,0}xy(1-z) + B_{1,0,1}x(1-y)z \\ + \quad & B_{0,1,1}(1-x)yz + B_{1,1,1}xyz\,. \end{aligned} \tag{3.23}$$

The field interpolation can be calculated in the three directions for B_x, B_y and B_z. The particle transport through these fields are discussed in the following sections.

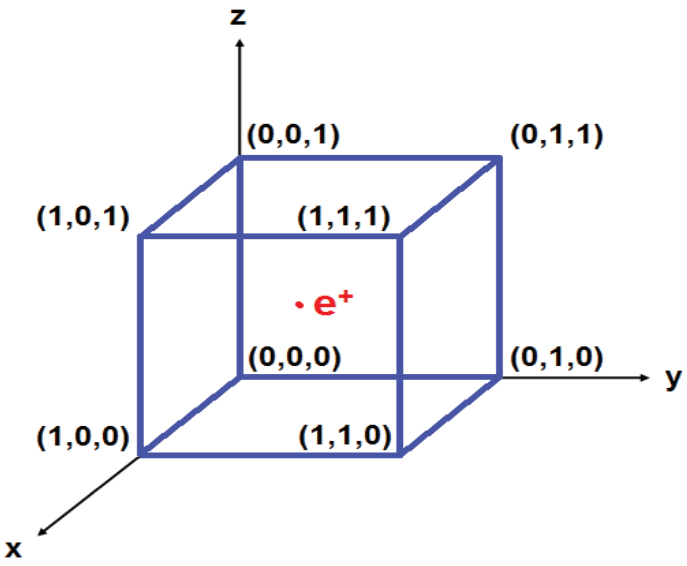

Figure 3.16: Field interpolation at a given positron position (x,y,z) in the field map mesh.

5.1 Spectometer

The particles going through the center of solenoids are not deflected. The spectrometer can be the first element to be studied with an ideal pencil-like beam. The spectrometer magnets are shaped as quarter of circles with a radius r of 203.4 mm, the gap between the poles is 53.3 mm for r <61 mm and are increasing linearly up to 104.1 mm at the outer part of the poles. A power supply provides the current for both magnets, the two dipoles have however opposite polarities to limit the effects of spin precession. By design, the two 90 degree angles result in a transverse displacement of 463.5 mm. The field map was calculated by the E166 collaboration and checked against measurements [47] (Fig. 3.17 left). The goal is to determine the spectrometer current necessary to deflect the ideal beam in the spectrometer to the polarimeter. The current running through the yokes of the dipoles is a function of the dipole fields, relating the current to the beam energy. A measurement [48] using a Hall probe showed that the saturation of the yokes introduced a non-linearity in

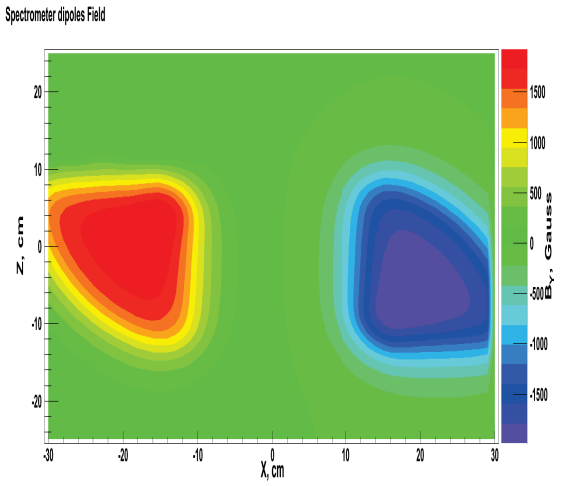

Figure 3.17: Spectrometer field map for the mid plan with a current of 100 A.

the field-current ratio. The field non linearity was estimated as $B_y = aI^2+bI+c$ with $a = -1.683.109-6T/A^2$, $b = 1.536.10^{-3}$ T/A and $c = 1.841.10^{-3}$ T. A simulation was conducted, as the dipole fields are not uniform (the integrated field along particles orbit in each dipole is not trivial), using a virtual detector at $S2ReconvTarget$. Using an ideal 8 MeV positron beam, the transverse position x from the center of the spectrometer exit beampipe and incident angle x' was studied as a function of the dipole current 3.18.

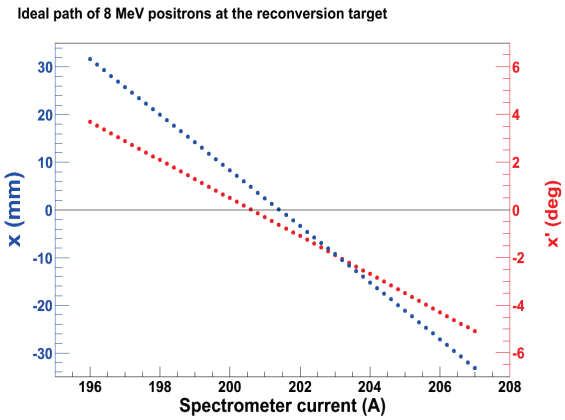

Figure 3.18: At the re-conversion target, the position and incident angle of a 8 MeV positron ideal path are represented as a function of the spectrometer current.

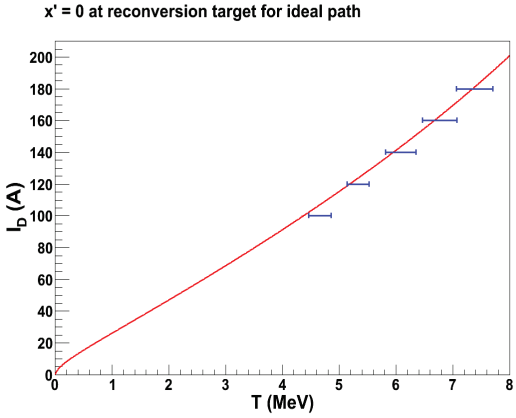

Figure 3.19: The spectrometer current for an incident angle of 0° at the $S2ReconvTarget$ virtual detector (red) and values experimentally found with a β source (blue).

At the $S2ReconvTarget$ virtual detector, an incident angle of 0° can be expected for an 8 MeV ideal beam with a spectrometer current of 200.6 A. For positron with kinetic energies $\{2; 3; 4; 5\}$ MeV, the current that could be applied in the spectrometer dipoles are $\{46.8; 68.4; 91.1; 115.2\}$ A (Fig. 3.19). These values are comparable to the experimental measurements of the E166 collaboration with a β source.

The energy selection of the spectrometer is determined by the angular acceptance of the jaws. The position of the jaws after the first dipole can be set so that the ideal beam track determined before goes through the center of the collimator allowing an even energy acceptance $T_{ideal} \pm \delta$. Two positron ideal beams with energies T_{ideal} + 10 % and T_{ideal} - 10 % along the same path before the spectrometer are sent in the spectrometer powered by a given current. The different paths set the total aperture of the jaws at 28.8 mm and an offset of 14.42 mm compared to the spectrometer vacuum chamber centerline for an energy acceptance $\Delta T/T = \pm 10$ %. The offset is due to the position of the jaws, right after the first dipole, right in the fringe field. The fields of the two dipoles cancel each other at the exact center of the vacuum chamber where the jaws could be centered on the spectrometer vacuum chamber center.

Based on the ideal path of particles, the spectrometer current can be used as a reference for the particles energy selection in case of a realistic positron distribution created by a 8 MeV electron beam in a 1 mm tungsten target. The solenoids can be used to collect particles off axis.

5.2 Solenoid S1

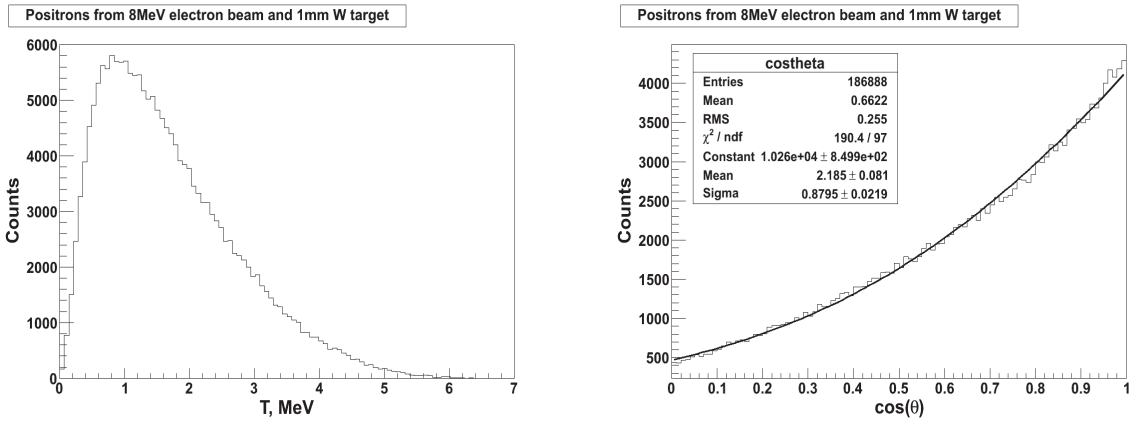

Figure 3.20: Energy distribution after the production target (left) and angular distribution (right) after the production target

The optimization of the first solenoid requires a realistic positron distribution (Fig. 4.8) from an 8 MeV electron beam in a tungsten target of 1 mm, in order to determine the current needed in the S1 solenoid for 2-5 MeV particles. Using the technical drawing provided by the E166 collaboration, a field map was extracted from Poisson/Superfish, see (Fig. 3.21) and implemented in the Monte Carlo. The solenoid current can be optimized to maximize the amount of positrons at the exit of the spectrometer and tuned as a function of the positron energy. The spectrometer current can be set for the ideal path of 2-5 MeV positrons and the positron phase space as a function of the S1 solenoid current can be studied at the two locations where virtual detectors save particle tracks.

The transmission rate represents the amount of positrons at $S2ReconvTarget$ or $NoS2ReconvTarget$ divided by the amount of positrons produced at the production target as a function of the S1 current. For a spectrometer current of 48.6

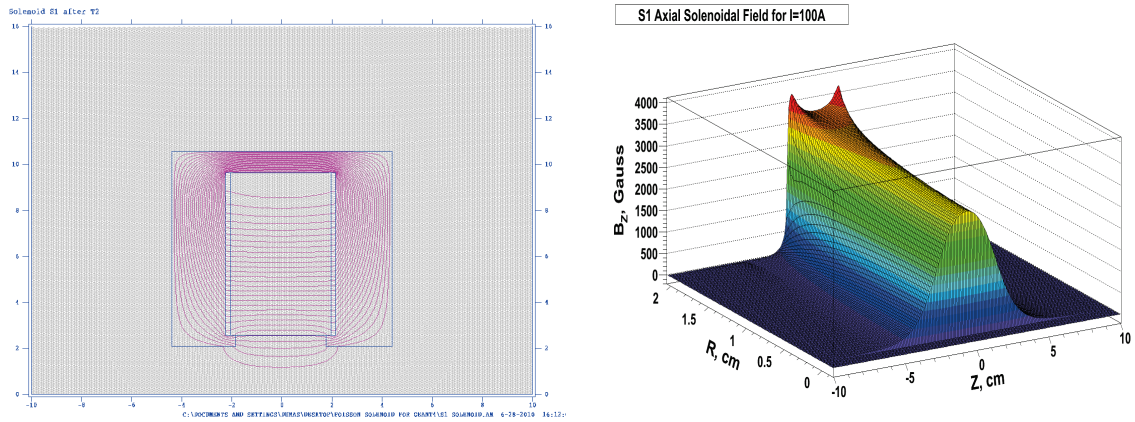

Figure 3.21: solenoid field lines (left) and axial field (right) for a current of 100 A in the coil.

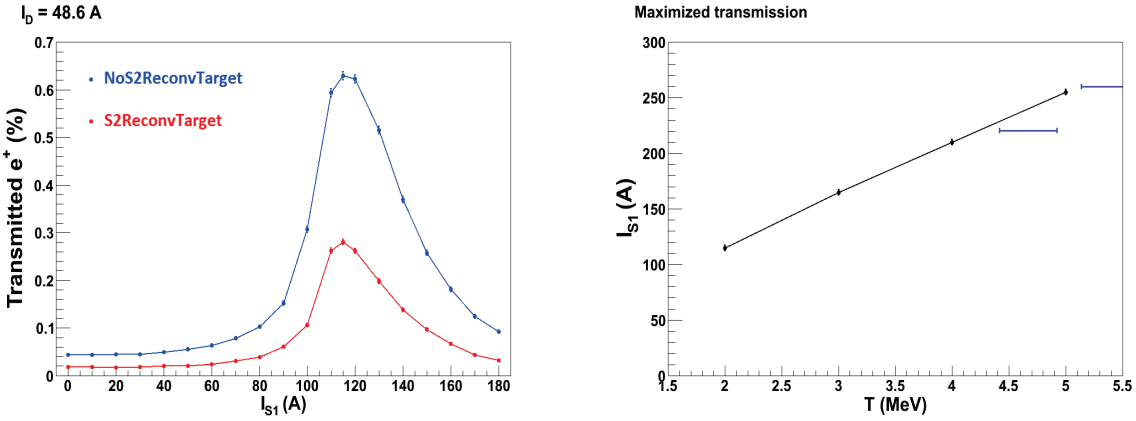

Figure 3.22: Transmission efficiency at $NoS2ReconvTarget$ and $S2ReconvTarget$ as a function of the current applied to the S1 solenoid for a given spectrometer current corresponding to a selection of 2 MeV particles (left) and optimized S1 currents calculated for PEPPo (black) and experimental currents measured for the E166 experiment (blue), as a function of the positron energy (right).

A (corresponding to 2 MeV positrons), the S1 solenoid current that maximizes the transmission is 115 A, see fig. 3.27 (left). The process can be repeted for other spectrometer currents corresponding to the selection of different positron energies, the optimum S1 current increases with the energy ranging from 120 A to 270 A (Fig. 3.27 right). The currents maximizing the transmission in the E166 experiment are reported as well. A minor difference can be explained by a different position of the collimator in between the dipoles.

5.3 Solenoid S2

For the second solenoid, the field of a standard CEBAF solenoid (FG) with a 76.2 mm inner diameter is calculated with Poisson/SuperFish (Fig. 3.23) Implemented in the simulation, the solenoid current can be optimized to maximize the amount of positrons at the re-conversion target and minimize the positron "beam" waist and phase space. This current can be optimized for every positron energy selected by the spectrometer ideal path and the S1 solenoid current that maximizes the amount of

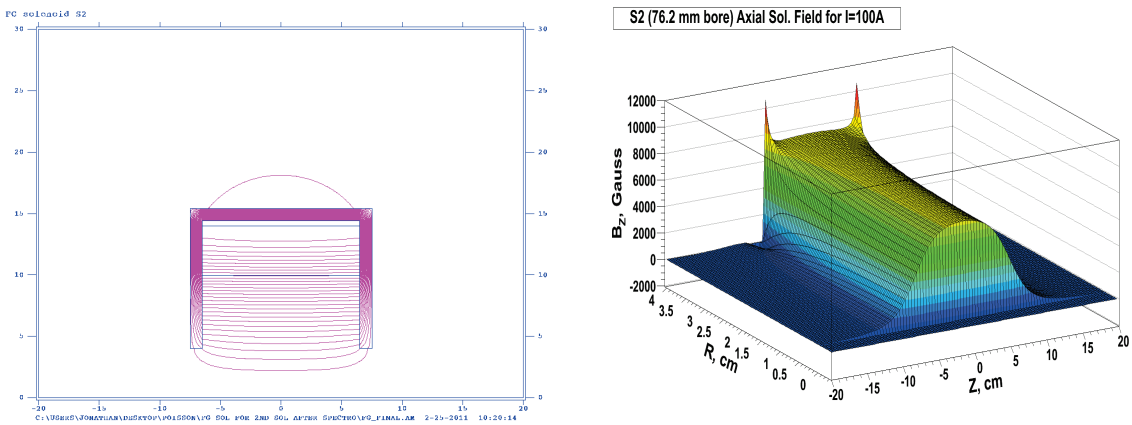

Figure 3.23: S2 solenoid field lines from Poisson/Superfish (left) and its axial field (right) for a current of 100 A in the coil.

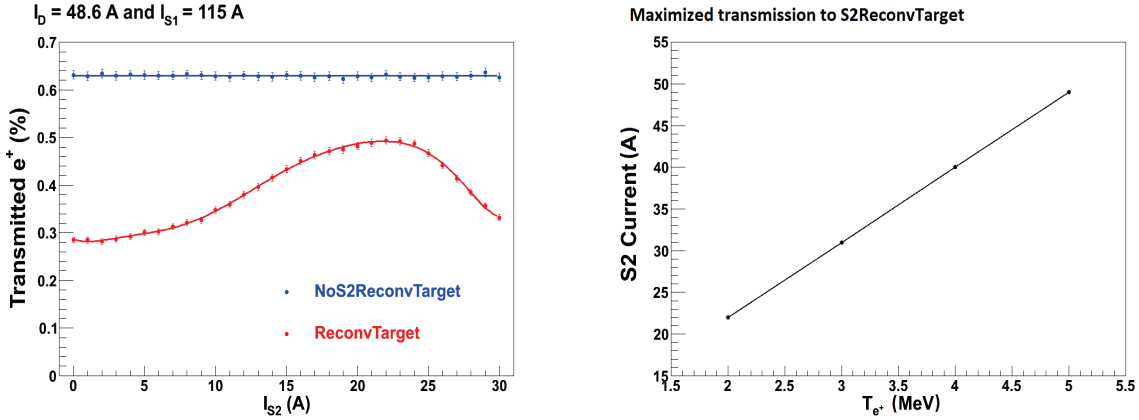

Figure 3.24: Transmission rate of positrons through the spectrometer at the virtual detectors (left) and optimum solenoid currents to maximize the amount of positrons as a function of their energy at $S2ReconvTarget$ (right)

positrons at $S2ReconvTarget$. For example, a spectrometer current of 48.6 A and an optimized S1 current of 115 A calculated in the previous section, maximize the collection of 2 MeV positrons at $NoS2ReconvTarget$, the S2 solenoid can maximize the amount of positrons at $S2ReconvTarget$ (Fig. 3.24 right).

The transmission rate at $S2ReconvTarget$ can gain a factor 2 from 0.29 % to 0.49 % with the help of the second solenoid (fig. 3.24). It is however not enough to collect all the particles present at the level of the $NoS2ReconvTarget$, where the transmission rate is 0.63 %. These rates do not take into account other parameters such as the energy selection or the control of the phase space after the spectrometer.

5.4 Solenoid S1 vs Solenoid S2

The transmission rate may be lower at $S2ReconvTarget$. The extra distance travelled eliminates particles with large angles at the exit of the spectrometer. The second solenoid provides a control over the positron beam waist, according to the phase space in the direction of spectrometer spread (Fig. 3.25). The second cross is also an asset for the characterization of the spectrometer line. A viewer in both

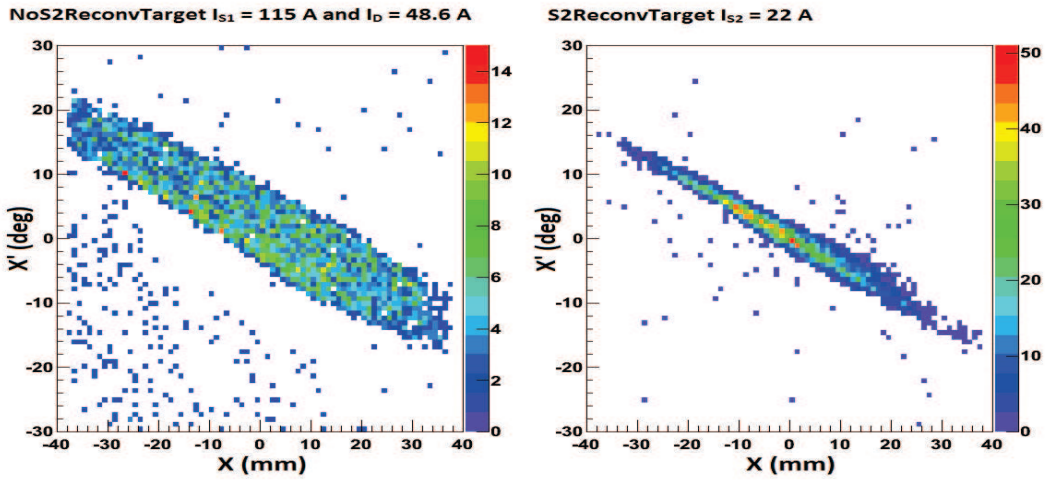

Figure 3.25: Positron phase spaces comparison at $NoS2ReconvTarget$ (left) limited by the beampipe size (76.2 mm) and at $S2ReconvTarget$ (right) for a spectrometer current of 48.6 A.

crosses gives information on the particles direction. The energy selection is also cleaner at $S2ReconvTarget$ where the positron energy is well constrained within $\Delta T/T \pm 10$ % (Fig. 3.26). At $NoS2ReconvTarget$, positrons with lower energies down to 0 MeV remain. The transport efficiency at the two locations considered with or without the second solenoid, (Fig. 3.27) shows the positron transmission between 2 and 5 MeV. After the spectrometer, depending on the distance travelled, the amount of positrons is lowered as they are dumped in the beampipe due to the wide spreading angle after the spectrometer. Adding collection optic devices help minimizing the effect of the dispersion. According to fig. 3.10, an 8 MeV electron beam in a 1 mm tungsten target produces a positron total current of 0.8 nA. The current that can be expected for 2 MeV positrons down to the end of the transport system at $S2ReconvTarget$, where the transmission is 0.49 %, is about 4 pA. The simplistic cuts ($\Delta T/T = \pm 10$ %) based on the energy selection of the jaws and the angular acceptance of the vacuum chamber $\Delta\theta = \pm 5°$ applied for fig.3.12 (left) were indicating a current four times lower at ~ 1 pA but still in the same order of magnitude. The S1 solenoid is responsible for increasing the amount of positrons going through the spectrometer down to the polarimeter.

6 Conclusion

The CEBAF photoinjector offers all the components necessary to produce and characterize a highly polarized electron beam. The addition of a new arm allowing the electron beam to produce polarized positrons in a tungsten target is not invasive. The resulting positrons can be collected and analyzed in a compact apparatus ($\sim$ m). A few μA of current can produce $\sim$ nA of positrons and $\sim$ pA can be used for a Compton transmission polarimeter. The polarized electrons could be used to calibrate the whole apparatus, transport and polarimetry. The Compton transmission polarimeter requires attention, especially for the signal detection and data acquisition. Part of the polarimeter was sent to the Laboratoire de Physique Subatomique

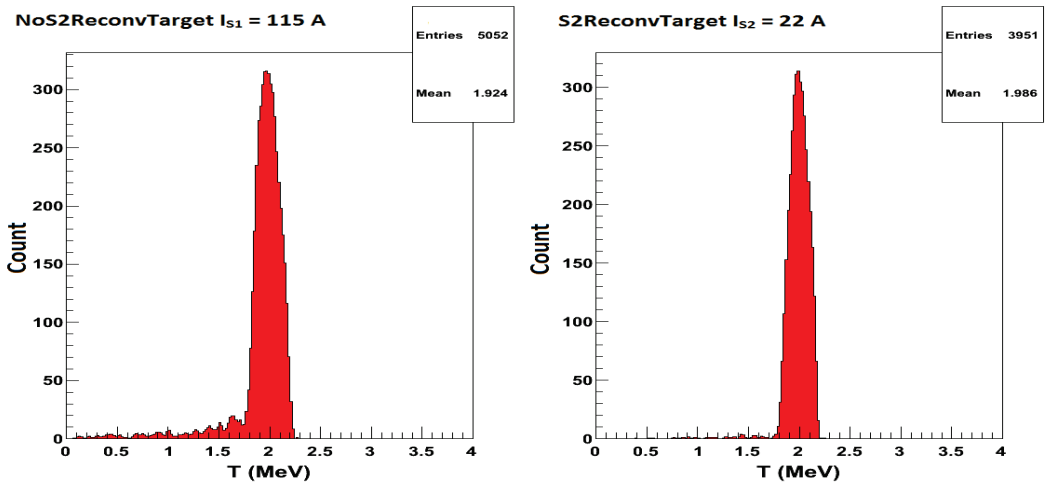

Figure 3.26: Energy distribution comparison at $NoS2ReconvTarget$ and at $S2ReconvTarget$ for a spectrometer current of 48.6 A.

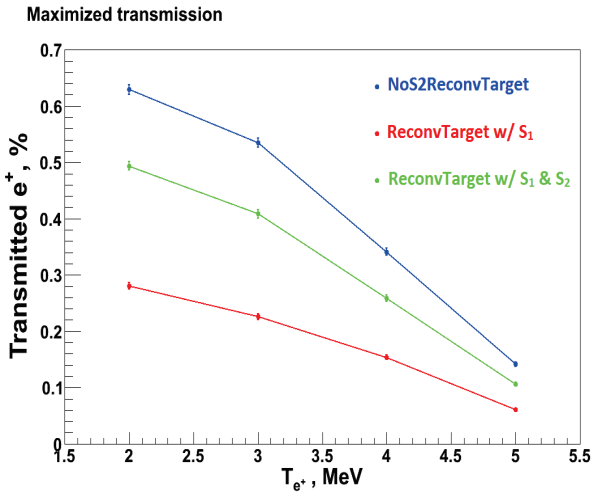

Figure 3.27: Positron transmission at optimized S1 and S2 currents as a function of the positron energy selected by the spectrometer.

et de Cosmologie de Grenoble for its characterization. The Compton transmission polarimeter and the tests made on the calorimeter are described in the next chapter.

Chapter 4

PEPPo polarimeter

1 Introduction

The polarimeter is part of the E166 collaboration loan. Some modifications have been applied for the signal integration. The Compton transmission polarimeter relies on the production of Bremsstrahlung photons in a tungsten reconversion target. The degree of polarization of the photons is indexed to the positron one. The photon polarization is measured through the polarization dependent component of the Compton scattering in a polarized iron target. The Compton absorption of these photons within a polarized iron target allows an asymmetry measurement between the number of photons transmitted for two opposite target polarization. In addition, the possibility of flipping the electron beam helicity hence the positron polarization allows the control of systematic uncertainties due to the target polarization switching. The photon flux is measured in a calorimeter after the polarized target.

2 Principle of operation

The photons can be counted in a calorimeter after the polarized target. The analyzing power of the Compton scattering changes with the photon energy. It can lead to two ways, an integrated or a semi-integrated method for measuring the photon asymmetry when flipping the beam polarization parallel $\uparrow\uparrow$ or anti-parallel to the polarized target $\downarrow\uparrow$. The signal detected by the calorimeter can be integrated with the photon energy or the signal can be associated with the photon energy.

2.1 Integrated method

The first method is integrating the whole energy deposited E_i^+ (E_i^-) by the Bremsstrahlung spectrum over the time corresponding to a single iron target-initial electron beam polarization set $\uparrow\uparrow$ ($\downarrow\uparrow$). The asymmetry is defined as

$$A_T = \frac{E^+ - E^-}{E^+ + E^-} = \frac{\sum_i E_i^+ - \sum_i E_i^-}{\sum_i E_i^+ + \sum_i E_i^-} \tag{4.1}$$

The total energy deposit per polarization set is

$$E_i^{\pm} = N_i \sum_p \epsilon_p^{\pm} e_p \tag{4.2}$$

where N_i is the total number of leptons per helicity macro-event i, and $\epsilon_p^{\pm}$ represents the photon efficiency, the number of photons associated with the energy e_p produced per lepton and absorbed in the calorimeter. The polarization dependent efficiency ϵ_p^3 can be expressed and separated from the non polarization dependent ϵ_p^0 according to eq 3.14 as

$$\epsilon_p^{\pm} = \epsilon_p^0 \pm P_e P_t \epsilon_p^3 \tag{4.3}$$

this leads to the experimental asymmetry

$$A_T = P_e P_t A_e = P_e P_t \left[\sum_p \epsilon_p^3 e_p / \sum_p \epsilon_p^0 e_p \right] \tag{4.4}$$

where A_e is the analyzing power of the polarimeter. The analyzing power can be estimated with either simulation or experiment with a known polarized beam. The electron beam which polarization can be compared with the Mott polarimeter. The statistical uncertainty on the beam polarization is deduced from the experimental asymmetry

$$\delta P_e = \left[2N P_t^2 \sum_p \epsilon_p^0 A_e^2 \right]^{-1/2} = [2N P_t^2 \mathrm{FoM_I}]^{-1/2} \tag{4.5}$$

assuming for simplicity that the experimental asymmetries are small and the uncertainties on the target polarization and the polarimeter analyzing power are neglected. The total number of electron per helicity state is defined as $N = \sum_i N_i$. The figure of merit ($\mathrm{FoM_I}$) represents the capabilities of the PEPPo polarimeter to actually measure the polarization.

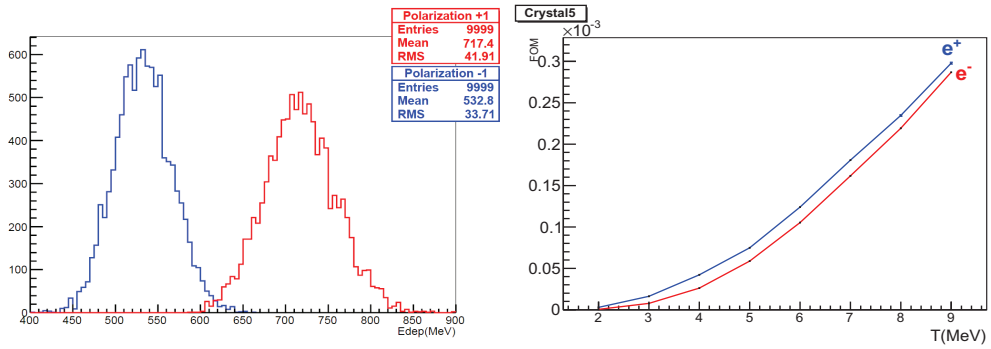

Figure 4.1: Simulated total energy deposit distribution in a CsI crystal for 6 MeV incident positrons (left) with opposite helicities (red and blue) and figure of merit (right) for electrons (blue) and positrons (red) with different energies. Each macro-event i corresponds to the crystal response for 10^5 incident particles, 10^4 macro-events have been generated assuming 100 % longitudinal polarization for the beam and the target (from Ref [74]).

The expected experimental asymmetry signal for 6 MeV positrons is shown on Fig. 4.1 (left). The positron beam and the polarized target are assumed to be fully

polarized to improve the simulation accuracy. The signal can be scaled to the actual target ($\sim 7\%$) and positron polarization. The experimental distribution of the total energy deposited in the calorimeter gives an idea of the sensitivity to polarization for PEPPo. The $\mathrm{FoM_I}$ is represented on Fig. 4.1 (right) for the crystal as a function of the kinetic energy of the incoming lepton beam. The difference between electron and positron response comes from the different processes implied such as annihilation which also produces polarized photons.

2.2 Semi-integrated method

An other way for extracting the polarization information is suggested by the sign change of the analyzing power as a function of the photon energies fig. 3.14. The idea is to separate the two opposite analyzing powers. This gives the intuition of an energy discretized method referred to as semi-integrated. The experimental asymmetry can be calculated for a given energy bin over the whole distribution of energy deposited in the calorimeter for each beam-target polarization set. The experimental asymmetry for an energy bin p is written as

$$A_T^p = \frac{n_p^+ - n_p^-}{n_p^+ + n_p^-} = \frac{\sum_i n_{pi}^+ - \sum_i n_{pi}^-}{\sum_i n_{pi}^+ + \sum_i n_{pi}^-} \tag{4.6}$$

where n_p is the number of photon detected with energy bin p for a given helicity macro-event i, the polarization dependence of the detector efficiency for each energy bin, the asymmetry can be written as

$$A_T^p = P_e P_t A_e^p = P_e P_t \frac{\epsilon_p^3}{\epsilon_p^0}\,. \tag{4.7}$$

The expected energy discretized asymmetry can be estimated by simulation or experiment just like for the integrated method. For each bin, the incoming beam polarization can be deduced from the corresponding experimental asymmetry, and the total experimental value is given by the sum of polarizations calculated at a given deposited energy

$$P_e = \sum_p \frac{P_e^p}{(\delta P_e^p)^2} \Big/ \sum_p \frac{1}{(\delta P_e^p)^2} \tag{4.8}$$

with the overall statistical uncertainty

$$\delta P_e = \Big[\sum_p \frac{1}{(\delta P_e^p)^2}\Big]^{-1/2} = \left[2N_e P_t^2 \sum_p \epsilon_p^0 (A_e^p)^2\right]^{-1/2} \tag{4.9}$$

$$= [2N_e P_t^2 FoM_{SI}]^{-1/2} \tag{4.10}$$

The semi-integrated asymmetry between two different beam-target sets is represented on Fig. 4.2 (left). The beam and target are fully polarized in the simulation comparison of the integrated and semi-integrated methods. The number of counts corresponds to 10^9 incident positrons of 6 MeV for each polarization set. The experimental asymmetry can be calculated for each energy bin. Asymmetries > 1 % are

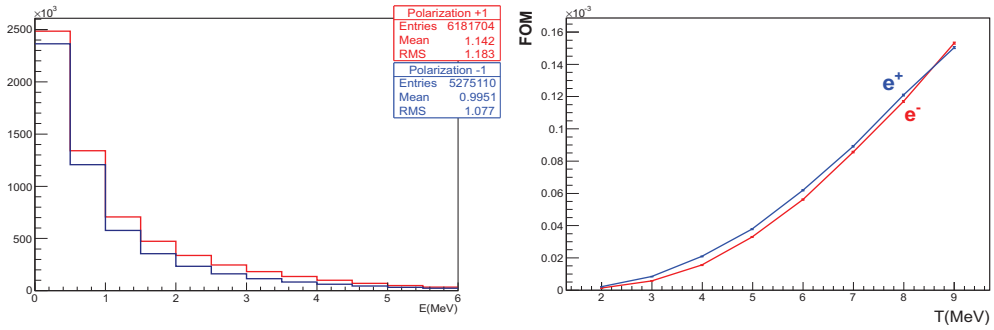

Figure 4.2: Simulated total energy deposit distribution in a CsI crystal for 6 MeV incident positrons (left) with opposite helicities (red and blue) and figure of merit (right) for electrons (blue) and positrons (red) with different energies. The events are generated assuming 100 % longitudinal polarization for the beam and the target from Ref [74].

observed at high deposited energies as expected with the Compton scattering but small efficiencies due to the bremsstrahlung spectrum. At low energy, it is interesting to notice that the asymmetry is not negative. This can be associated with the geometry of the calorimeter. The most energetic photons that go through a small section of the calorimeter can deposit as much energy as photons with low energy that deposit all of their energy. The sum of the two contributions gives a positive asymmetry. The figure of merit ($\mathrm{FoM_{SI}}$), as defined from eq. 4.10 is represented on Fig. 4.2 (right) as a function of the kinetic energy of the lepton beam. The figure of merit might be twice as less effective as the integrated method but the systematic uncertainties can be reduced by comparing the two methods.

3 Mechanical design

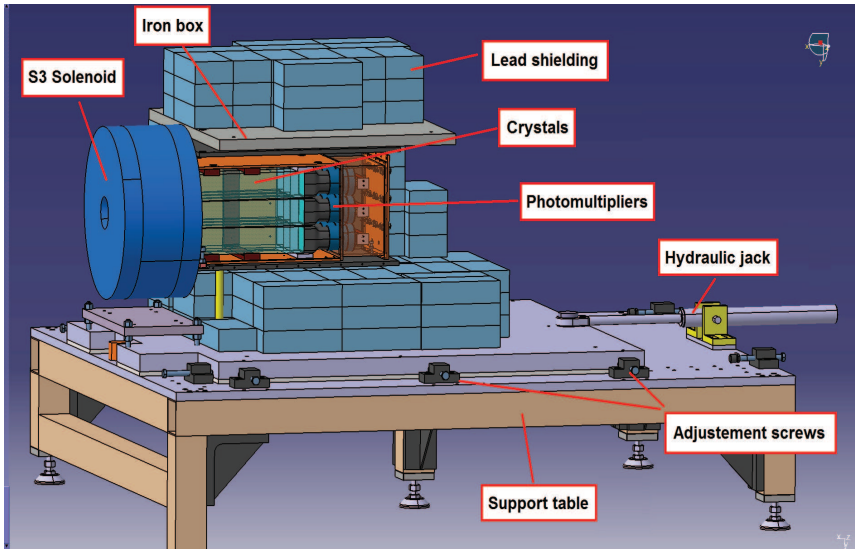

Figure 4.3: Schematic of the polarimeter setup

The layout of the positron polarimeter is shown in Fig. 4.3. All elements of the polarimeter are on a moving plate allowing fine adjustments in the positions and incidence angle of the lepton beam. The polarimeter can move independently from the rest of the positron line thanks to a hydraulic jack (20 cm shift possible) and adjustment screws on an iron plate allowing for rotations ($\pm 10^\circ$ relative to the positron transport line) where the whole apparatus is fixed. The table mechanical strength and displacements were both checked by Finite Element Model calculation and by a load testing (3,3 t).

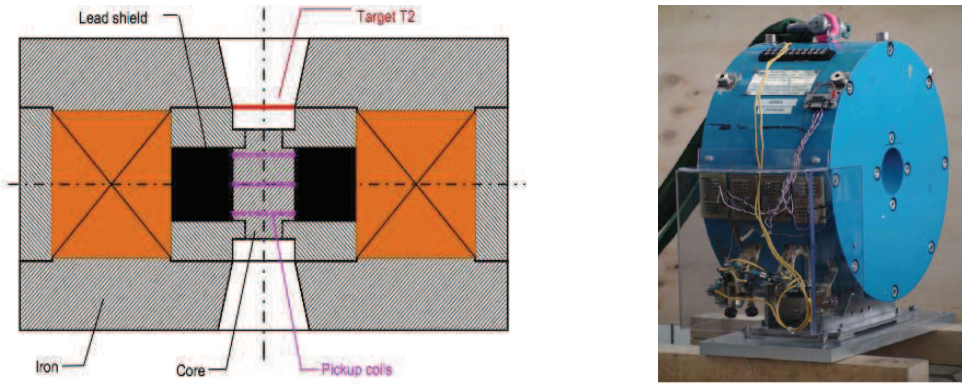

Figure 4.4: Schematic (left) and photo (right) of the S3 Solenoid

The S3 solenoid (Fig. 4.4) has a 7.5 cm long (5 cm diameter) magnetized iron core, used as the photon absorber, and holds the reconversion target (0.5 radiation length of tungsten) 1.25 cm upstream of the iron core frontline. The main characteristics are listed in table 4.1

Overall length	200 mm
Overall diameter	392 mm
Iron core length	75 mm
Iron core diameter	50 mm
Overall mass	175 kg
Number of coils	2
Coil length	49 mm
Coil inner diameter	152 mm
Coil outer diameter	322 mm
Number of turns per coil	160
Operating current	$\pm$ 60 A
Current reversal time	1 s
Time between reversal	5 min
Field B_z^{max} at center	2.324 T
Iron target polarization on axis	0.0736

Table 4.1: Characteristics of the S3 solenoid.

The calorimeter is located 7.25 cm downstream of the solenoid iron core and is constituted of 9 Cesium Iodide crystals doped with Thallium CsI(TI) in a 3×3

array. The crystals were supplied by Monokristal/Kharkov (Ukraine). They have a length of 28 cm corresponding to 15 radiation lengths to ensure the complete energy deposition of photons. Their transverse section is 6×6 cm^2 and they are stacked in a brass chamber with 6 mm wall thickness and an entrance window of 2 mm thickness. The box is light tight and filled with a continuous flow of nitrogen to prevent damaging the crystals due to air humidity. Each crystal is wrapped in two layers of white Tyvek paper to increase the scintillation light collection, and with a copper foil (30 μm) to prevent cross-talk. This results in a 1.2 mm dead space between the crystals. The most important properties of the crystals are summarized in table 4.2.

Material	CsI
Thallium (dopant)	0.08 mol %
Length	280 mm
Height	60 mm
Width	60 mm
Density	4.51 g/cm^3
Radiation length	18.6 mm
Moliere radius	38 mm
Decay time signal	2 μs
Peak emission wavelength	550 nm

Table 4.2: Parameters of the CsI(Tl) crystals.

The crystals are coupled with Hamamatsu R6236-01 photomultipliers (PMTs) via a 3 mm thick optical silicon cookie. The PMTs have a mechanical transverse size of 6×6 cm^2 but the photocathode is 5.4×5.4 cm^2. The brass box containing the crystals, PMTs and electronic system is enclosed in a μ-metal shoe box and a 1 cm iron layer to prevent any field (from the Earth or S3) interference with the PMTs. The calorimeter total weight (including brass box, crystals, PMTs, electronics) is 48 kg. Shielding with 250 bricks is used to reduce the photon background that is not coming from the iron target.

4 Technical performances

At saturation, the overall longitudinal polarization of the iron target is 8.19%. Saturation is obtained using a 60 A bipolar current supply for the solenoid. A 2.3 Tesla magnetic field is created by two coils (160 turns per coil with a section of 4×4 mm^2) that are equipped with a water cooling system. Averaged polarization value of the iron target is 0.069±0.002, according to the E166 collaboration. The magnetic field of the iron can be measured with several pickup coils surrounding the core of the magnet. The induced-voltage signal due to a change of the magnetic flux through the pickup coils is measured with a Precision Digital Integrator PDI upon field reversal. The external Field map will also be measured to know the fringed field and to constraint the calculations. The expected polarization error is of the same order of magnitude that the one obtained for E166 (∼1%). The solenoid field can be determined with a Poisson/Superfish calculation, Fig. 4.5 The field at the

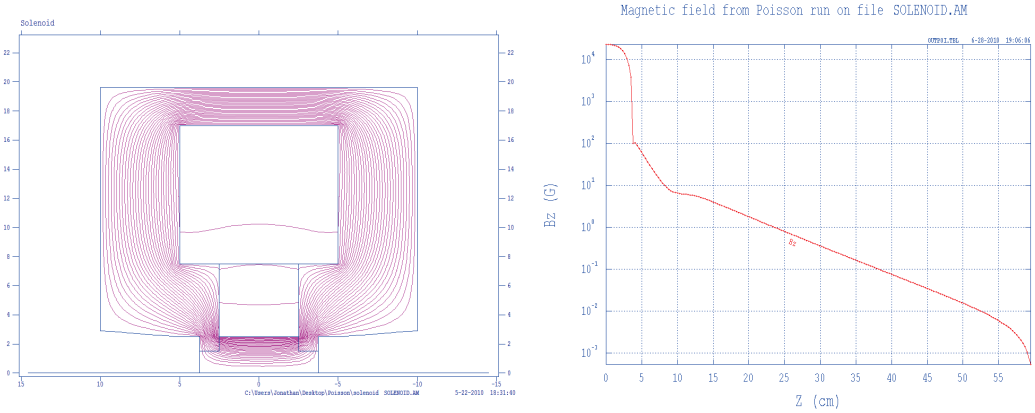

Figure 4.5: S3 solenoid field lines (left) and numerical field values along the central axis.

level of the PMTs (38.5 cm from the solenoid centerline) is calculated to be $\sim$ 0.1 G, which is not problematic since the brass box in which the PMTs are located is covered with μ-metal.

The PMTs are using a homemade socket which includes an amplifier ($\times$108). A typical high voltage ranging from 1000 V to 1400 V depending on the PMTs (maximum for these PMTs are 1500 V) allows for a wide range of photon energies between 0.1 MeV and 5 MeV. All high voltage internal connections are insulted to avoid direct contact. The output signal (50 Ω) ranges from -40 mV to 1.9 V which is suitable for the fast ADC input (FADC). A set of optical fibers coupled to the crystals are inserted to monitor the relative change in gain during operation for off-line correction and occasional high voltage adjustment. A LED trigger is made with a pulser and a rate divider which amplitude can be adjusted between 0 and -3 V.

5 Experimental characterization of the crystals

The quality test of the crystals was made at the LPSC. Using a photon source and a crystal coupled with a PMT. A collimator between the source and the detector was limiting the area of the crystal to ensure the full energy deposition of the photons. Cosmic particles were also studied using scintillating paddles as triggers.

5.1 Data acquisition system

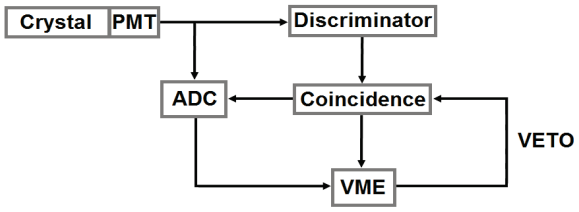

Figure 4.6: Schematic of the data acquisition system for radioactive source measurements

The Data acquisition (DAQ) is built upon a Versa Module Eurocard (VME) system. For a radioactive source test for crystals taken individually, a very simple setup can be made using the signal from the photomultiplier. This signal is splitted to go in the Analog-to-Digital Converter (ADC) directly or analyzed by a discriminator. The discriminator output goes through a coincident module which acts as a gate of signal integration for the ADC (see Fig. 4.6). For cosmic measurements, scintillators paddles are used for triggering cosmic muons passing through the calorimeter (see Fig. 4.7). The scintillators are connected to a leading edge discriminator (CAEN V895), the majority level is set to two, corresponding to a 2 paddle scintillator hit out of a 5 paddle setup where 2 paddles are above (H1, H2) the crystals and 3 under (B1, B2, B3). The discriminator output is sent to a Time-to-Digital Converter (TDC) for off-line selection of fired paddles.

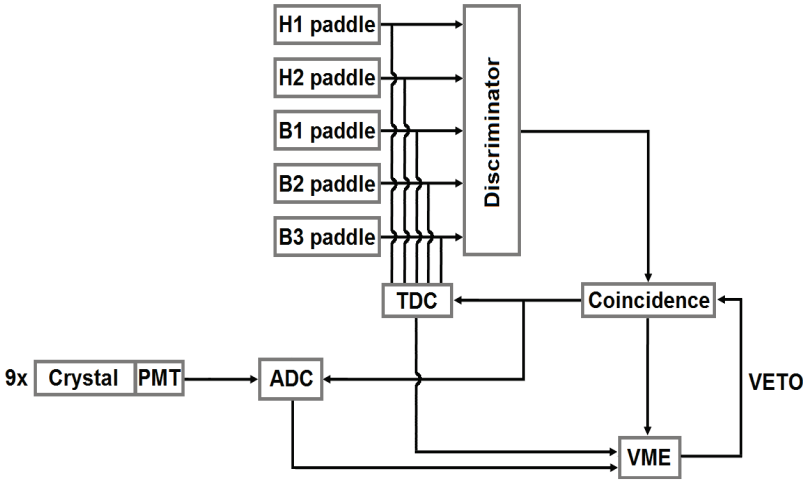

Figure 4.7: Schematic of the data acquisition system for cosmic measurements

5.2 Radioactive source measurements

A typical measurement with a radioactive source shows a photo-peak signal that can be fit by a Gaussian (Fig. 4.8). It can be used for the energy calibration of the crystal-PMT setup. The peaks in green for both plots correspond to the pedestal, a reference against which the signal peaks can be compared to. Its ADC channel is located around 360 and can be associated with the origin of the ADC scale. The difference between the pedestal and signal peak locations represents quantitatively the analyzed photon energy. For example, the Cesium 137 source emits monochromatic photons with an energy of 0.662 MeV. The ADC peak in red for an ADC channel of 1900 indicates that a 1540 ADC channel difference between the pedestal and peak location corresponds to an energy of 0.662 MeV. For a Sodium 22 source, the emission of 0.511 and 1.275 MeV photons correspond to ADC channels of 1600 and 3500 respectively.

The energy resolution of the crystal-PMT setup can be determined using these radioactive sources and the width of the signal peaks. For a Cs^{137} source, the energy

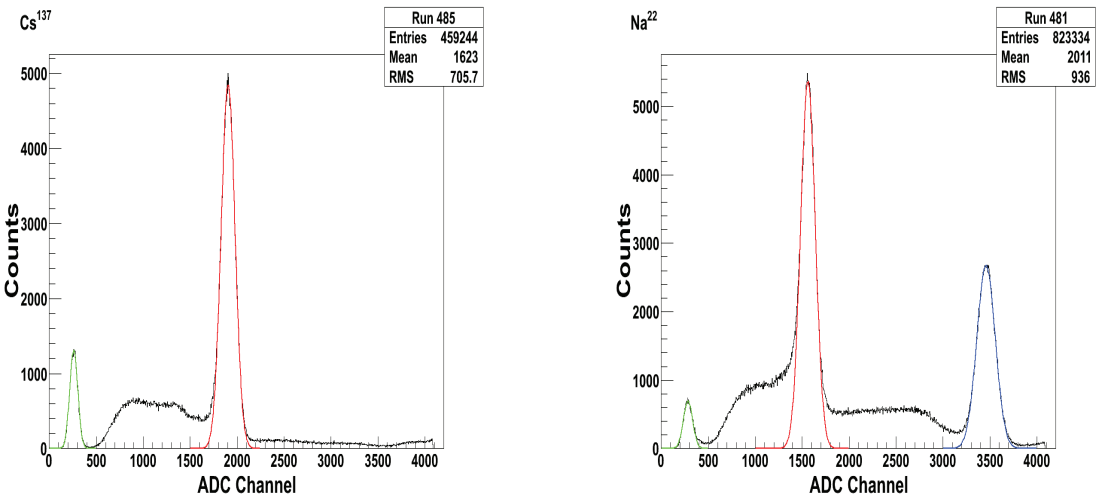

Figure 4.8: ADC spectrum of the crystal for a Cs^{137} (left) and a Na^{22} (right) sources.

detector resolution defined as

$$\frac{\Delta E}{E} = \frac{Peak\,Width}{Peak\,Loc. - Pedestal\,Loc.}\,. \tag{4.11}$$

The resolution depends on the time length of integration for the photon signal (Fig. 4.9 left). As the gate length increases, the ADC signal becomes sharper as more and more signal is integrated, the energy resolution decreases and reaches 3.5% for a 4 μs gate. The resolution increases then for a 6 μs as more and more background noise is integrated along with the real signal. For a fixed 2 μs gate length, the 9 crystals can be compared individually. The resolution ranges from 3.5 and 5.5 % (Fig. 4.9).

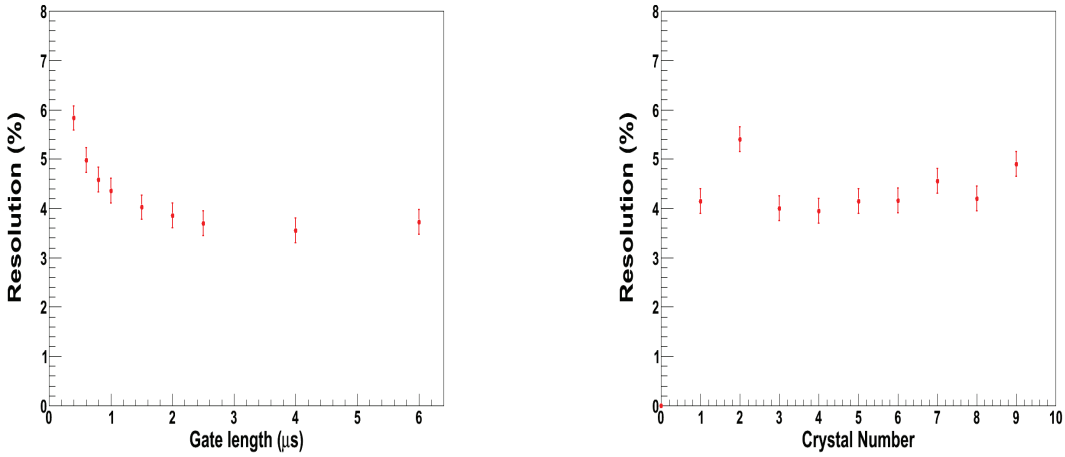

Figure 4.9: Gate integration time for the central crystal (left) and energy resolution for each crystal with a gate length of 2 μs (right).

The PMT voltages can be adjusted to standardize the Cs^{137} signal amplitude at $\sim$250 mV. The voltages are listed in table 4.3 for the nine crystals.

Crystal	Voltages
1	1200
2	1050
3	1125
4	1000
5	1060
6	1080
7	1145
8	1225
9	1170

Table 4.3: PMT voltages for a 250 mV signal amplitude corresponding to 0.662 MeV photons.

5.3 Cosmic rays measurements

A cosmic measurement have been realized using a set of 5 scintillating paddles that triggers cosmic muons passing through the calorimeter (Fig. 4.10). A coincidence between one of 2 scintillators above (H1 and H2) and one of 3 scintillators below (B1, B2 and B3) have been made. The calorimeter allows measuring the cosmic at minimum ionization and gives an absolute calibration of the crystals. Energy loss of a minimum ionizing muon is 40 MeV for each crystals according to simulations. A rate of 1 Hz was obtained during the test and several hours of counting were necessary. Due to the large signal of the cosmics (40 MeV compared to a ∼MeV gammas for the sources) amplifiers on the PMTs basis have to be bypassed for cosmic measurements. The output amplitude of the cosmic is then around 140 mV.

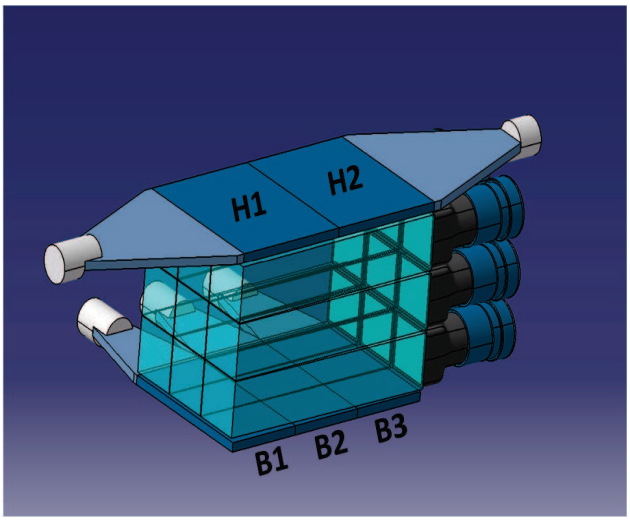

Figure 4.10: Plastic scintillator trigger setup.

The measurement selecting the scintillator paddles hit by the muons are either triggered with a) the H1 and B1 scintillators, b) H1 or H2 with B2 resulting in more counts, or c) H2 with B3 (Fig 4.11). The peaks representing cosmic rays, in red, are attenuated so that they are included in the ADC scale. The ∼40 MeV correspond to an ADC channel of 1900 regardless of the cosmic ray position relatively to the PMT as expected.

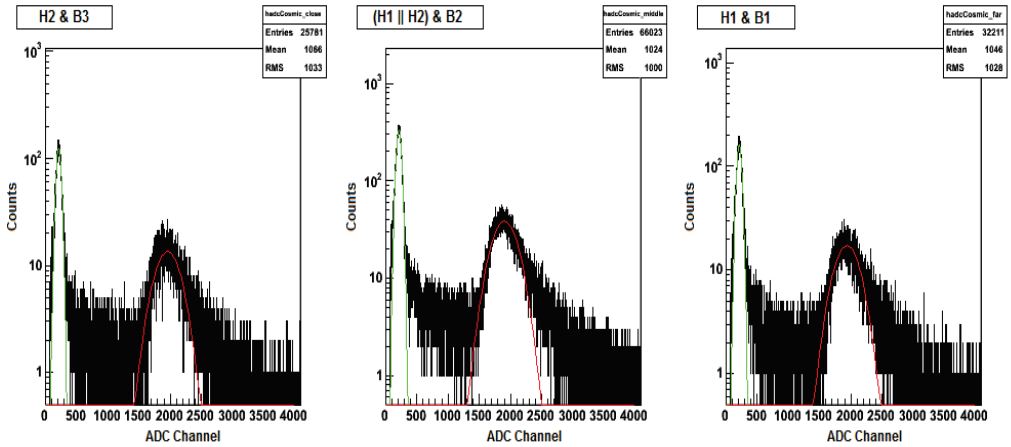

Figure 4.11: Cosmic measurement for the three scintillator triggers.

6 Conclusion

Two methods of signal integration are proposed, controlling the effect of systematic uncertainties. The calorimeter has been tested and the table support built at the LPSC. It has been sent to JLab for the assembly with the S3 solenoid The resolution of the calorimeter is precise at the 5 % level which is accurate enough for both integrated and semi-integrated methods.

Chapter 5

Conclusion

Polarized positrons became an important issue for the next generation of accelerator facilities. In the context of the JLab 12 GeV Upgrade, the availability of a polarized positron source would enhance the physics reach of CEBAF providing a unique tool to investigate more accurately the partonic structure of nucleons, and would allow for a precise study of the leptonic probe. Among the different possible schemes for the production of polarized positrons, the polarization transfer from sub-GeV electrons via polarized bremsstrahlung and pair creation appears the most appropriate to pursue at JLab.

The investigations of the conceptual capabilities of this new technique demonstrated a promising scheme, potentially able to deliver beam currents up to 1 μA assuming an ad-hoc collection system and less than 100 MeV incident electrons. These studies did also point-out the lack of understanding of polarization transfers in the pair creation process at low energy. This present thesis work did motivate new theoretical developments which brought a specific light on the importance of the electron mass in these calculations, and predicted a significant impact on the polarization transfers even at relativistic energies where the most commonly used prescriptions were expected appropriate. This feature is one additional motivation for an experimental demonstration of this technique.

There are experimental expectations from the bremsstrahlung production of polarized photon beams and the creation of polarized e^+e^- pairs from polarized photons that the bremsstrahlung of polarized electrons could serve as a mechanism for the production of polarized positrons. It is the purpose of the PEPPo experiment at JLab to demonstrate the reliability of this technique which was never attempted. This proposal which built in a *Letter of Intent* to the Program Advisory Committee (PAC) of JLab (see appendix) is a direct result of this thesis work. Within the context of this thesis, the conceptual design of this experiment was studied and optimized, on the basis of the experimental equipment of the SLAC E166 experiment which successfully demonstrated the helical undulator technique for a polarized positron source for ILC. It was shown that some mechanical adjustments of the existing equipment would benefit the operation of the set-up: accommodating an independent motion of the jaws allows a better selection of a given momentum range by taking into account the effects of the fringe field of the dipoles. Additionally, a new solenoid at the exit of the 2-dipoles spectrometer would allow a better control of the secondary positron beam at the polarimeter target, improving the quality of

the positron polarization measurements intended with PEPPo.

Taking advantage of electronics developments for the JLab 12 GeV Upgrade, these measurements will be performed following two different methods allowing for a better control of systematics, an issue of importance for small experimental asymmetries. Energy integrated and energy semi-integrated measurements have been proposed. The energy resolution requested for the latter method did led to the modification of the readout of the light-output of the crystals array. The design and construction of the PEPPo polarimeter has been discussed, together with the measured experimental performances obtained with radioactive sources and cosmic rays.

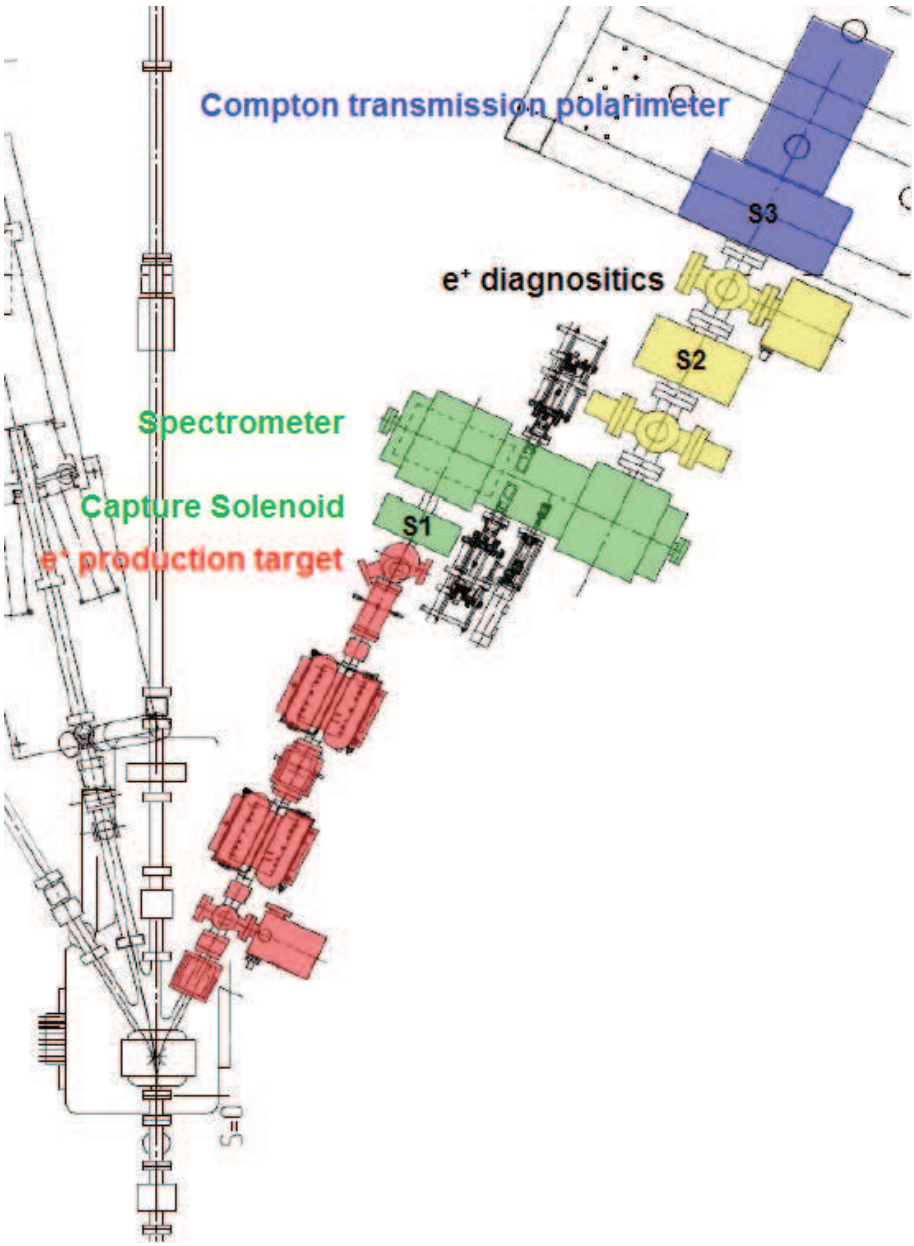

Figure 5.1: Final PEPPo layout [74].

During the writing of this manuscript, the PEPPo project developed and became

a full proposal [74] submitted to the JLab PAC which will meet in August 2011. The PEPPo technical design evolved and is including today several other elements and diagnostic devices (Fig. 5.1) which makes PEPPo a unique facility under construction at the CEBAF injector. Following this work, a new vacuum chamber for the spectrometer has been designed and a new beam section between the spectrometer and the polarimeter has been inserted which comprises a solenoid, a positron annihilation counter, a Faraday cup, beam viewers and a fiber array detector to characterize the positron beam profile.

PEPPo will prove the feasibility of polarized positron sources based on polarized bremsstrahlung. The experiment will run at low energy, precisely in the region where different calculations show drastically different results. PEPPo is then expected to test to some extent the elementary physics of polarization transfers in the pair creation process. We would expect that PEPPo data will verify the accuracy of the KBST description as an improvement of the OM description.

Bibliography

[1] P.A.M. Dirac, Proc. Roy. Soc. Lond. **117** (1928) 612.

[2] C.D. Anderson, Phys.l Rev., **43**, (1933) 491.

[3] A.A. Sokolov, I.M. Ternov, *Synchrotron Radiation*, Pergamon Press, 1968.

[4] C.K. Sinclair, et al .,*AIP Conf. Proc.*, **35**, (1976) 426 .

[5] L. Elouadrhiri, T.A. Forest, J. Grames, W. Melnitchouk, E. Voutier, *Proc. of the International Workshop on Positrons at Jefferson Lab (JPos09)*, AIP Conf. Proc. **1160**, 2009.

[6] L.A. Page, M. Heinberg, Phys. Rev. **106** (1957) 1220.

[7] V.B. Berestetskii, E.M. Lifshitz, L.P. Pitaevskii, *Quantum Electrodynamics*, Pergamon Press, 1982.

[8] H. Olsen, L.C. Maximon, Phys. Rev. **114** (1959) 887.

[9] D. Rice, Proc. of the *Vth European Particle Accelerator Conference*, Barcelona (Spain), (1996) 17.

[10] D.P. Barber, Proc. of the *IInd European Particle Accelerator Conference*, Nice (France), (1990) 164.

[11] D.P. Barber *et al.*, Proc. of the *IInd European Particle Accelerator Conference*, Nice (France), (1990) 173.

[12] A. Hofmann, Nucl. Phys. B - Proc. Suppl., **3**, (1988) 511-523.

[13] J.J. Kelly, Phys. Rev. C **66** (2002) 065203.

[14] M.N. Rosenbluth, Phys. Rev. **79** (1950) 615.

[15] A.L. Akhiezer, M.P. Rekalo, Sov. J. Part. Nucl. **3** (1974) 277.

[16] R.G. Arnold, C.E. Carlson, F. Gross, Phys. Rev. C **23** (1981) 363.

[17] M.K. Jones *et al.*, Phys. Rev. Lett. **84** (2000) 1398.

[18] O. Gayou *et al.*, Phys. Rev. Lett. **88** (2002) 092301.

[19] A.J.R. Puckett *et al.*, Phys. Rev. Lett. **104** (2010) 242301.

[20] L. Andivahis *et al.*, Phys. Rev. D **50** (1994) 5491.

[21] M.E. Christy *et al.*, Phys. Rev. C **70** (2004) 015206.

[22] I.A. Qattan *et al.*, Phys. Rev. Lett. **94** (2005) 142301.

[23] A.J.R. Puckett, *JLab Users Group Meeting*, June, 7-9, 2010; *http://conferences.jlab.org/ugm/2010/Wednesday/AM/User2010ThesisPrizePuckett.pdf*

[24] P.A.M. Guichon, M. Vanderhaeghen, Phys. Rev. Lett. **91** (2003) 142303.

[25] M.P. Rekalo, E. Tomasi-Gustafsson, Nucl. Phys. A **740** (2004) 271-286.

[26] D. Müller, D. Robaschick, B. Geyer, F.M. Dittes, J. Hořejši, Fortschr. Phys. **42** (1994) 101

[27] A.V. Radyushkin, Phys. Rev. D **56** (1997) 5524.

[28] X. Ji, Phys. Rev. Lett. **78** (1997) 610.

[29] M. Diehl, Phys. Rep. **388** (2003) 41.

[30] M. Burkardt, Phys. Rev. **D** 62 (2000) 071503(R).

[31] M. Diehl, Eur. Phys. Jour. **C** 25 (2002) 223.

[32] M. Diehl, *CLAS12 European Workshop*, Genova (Italy), February 25-28, 2009; *http://www.ge.infn.it/∼clas12/talks/thursday_ session6/diehl-genova.pdf*

[33] M. Guidal, Eur. Phys. J. A **37** (2008) 319.

[34] H. Moutarde, Phys. Rev. D **79** (2009) 094021.

[35] P.-Y. Bertin, C.E. Hyde, C. Muñoz Camacho, J. Roche *et al.*, Jefferson Lab Prop. **PR-07-007**, 2007.

[36] R.H. Milburn, Phys. Rev. Lett. **10** (1963) 75.

[37] A. D'Angelo *et al.*, Nucl. Inst. Meth. A **455** (2000) 1.

[38] T. Hirose *et al.*, Nucl. Inst. Meth. A **455** (2000) 15.

[39] M. Fukuda *et al.*, Phys. Rev. Lett. **91** (2003) 164801.

[40] M. Fukuda *et al.*, Phys. Rev. Lett. **96** (2006) 114801.

[41] B.M. Kincaid, J. Appl. Phys. **48** (1977) 2684.

[42] A.A. Mikailichenko, Cornell CBN **02-10**, SLAC LCC **0106** (2002).

[43] S.M. Seltzer, M.J. Berger, Phys. Rev. C **7** (1973) 858.

[44] J. Dumas, J. Grames, E. Voutier, JLab-TN **0**8-086 (2008).

[45] J. Grames et al., Proc. of the *PAC*, New York (USA), March-April (2011).

[46] G. Alexander *et al.*, Nucl. Inst. Meth. A **610** (2009) 451.

[47] K. Laihem, Ph.D. Thesis, Humboldt University, Berlin (Germany), 2008.

[48] W. Bugg, Spectrometer test experiment **Technical report, SLAC, E-166 Collaboration** (2006).

[49] G. Alexander *et al.*, Phys. Rev. Lett. **100** (2008) 210801.

[50] H.W. Koch, J.W. Motz, Rev. Mod. Phys. **31** (1959) 920.

[51] Y.-S. Tsai, Rev. Mod. Phys. **46** (1974) 815.

[52] E.A. Kuraev, Y.M. Bystritskiy, M. Shatnev, E. Tomasi-Gustafsson, Phys. Rev. C **81** (2010) 055208.

[53] E.G. Bessonov, A.A. Mikhailichenko, Proc. of the V^{th} *European Particle Accelerator Conference*, Barcelona (Spain), June 10-14, 1996.

[54] A.P. Potylistin, *Nucl. Inst. Meth. A* **398** (1997) 887.

[55] E. Haug, W. Nakel, *The elementary process of bremsstrahlung*, World Scientific, Lect. Not. Phys. **73**, 2004.

[56] E. Voutier, Proc. of the *XXth Baldin Seminar on High Energy Physics Problems*, Dubna (Russia), October 4-9, 2010.

[57] C.G. Darwin, Proc. Roy. Soc. A **118** (1928) 654.

[58] H.A. Bethe, L.C. Maximon, Phys. Rev. **93** (1954) 768.

[59] H. Davies, H.A. Bethe, L.C. Maximon, Phys. Rev. **93** (1954) 788.

[60] J.L. Matthews, R.O. Owens, Phys. Rev. **111** (1973) 157.

[61] W.H. McMaster, Rev. Mod. Phys. **33** (1961) 8.

[62] B.A. Mecking *et al.*, Nucl. Inst. Meth. **A 503** (2003) 513.

[63] S. Agostinelli *et al*, Nucl. Inst. Meth. **A 506** (2003) 250.

[64] R. Dollan, K. Laihem, A. Schälicke, Nucl. Inst. Meth. **A 559** (2006) 185.

[65] J.M. Hoogduin, Ph.D. Thesis, Rijkuniversiteit Groningen, Groningen (Netherlands), 1997.

[66] X. Artru, Proc. of the *POSIPOL 2009 Workshop*, Lyon (France), 23-26 June, 2009.

[67] J. Dumas, J. Grames, E. Voutier, AIP Conf. Proc. **1160** (2009) 120.

[68] S. Golge, Ph.D. Thesis, Old Dominion University, Norfolk (Virginia, USA), 2010.

[69] C. Hugenschmidt, K. Schreckenbach, D. Habs, P.G. Thiroll, ArXiv nucl-ex:1103.0513.

[70] X. Artru *et al.*, Nucl. Inst. Meth. **B 119** (1996) 246.

[71] D.R. Lide, Handbook of Chemistry and Physics, 73rd Edition, CRC Press, Boca Raton (Florida, USA), 1992.

[72] P. Perez, A. Rosowsky, Nucl. Inst. Meth. **532** (2004) 523.

[73] J. Dumas, Master Thesis, Université Joseph Fourier, Grenoble (France), 2007.

[74] J. Grames, E. Voutier *et al.*, Jefferson Lab Prop. **PR-11-**, 2011.

1 Letter of intent to PAC35

Letter of Intent to PAC35

Polarized electrons for polarized positrons:
A proof–of–principle experiment

Alexandre Camsonne[1], Jonathan Dumas[1,2], Arne Freyberger[1], Joseph Grames[1,†], Matt Poelker[1], Jean-Sébastien Réal[2], Eric Voutier[2,†]

[1] *Thomas Jefferson National Accelerator Facility, 12000 Jefferson Avenue Newport News, Virginia 23606, USA*

[2] *Laboratoire de Physique Subatomique et de Cosmologie IN2P3/CNRS, Université Joseph Fourier, INP 53 rue des Martyrs 38026 Grenoble cedex, France*

Abstract

This letter proposes an experiment at the CEBAF injector to demonstrate and measure the longitudinal polarization transfer from a highly spin polarized electron beam to positrons via the polarized bremsstrahlung and subsequent pair-creation processes in radiator and pair production targets, respectively. A new dedicated injector beam line and experimental apparatus is described. The segmentation of the MeV region of the injector from the remaining CEBAF complex is described as a strategy to perform the experiment during the 6-month shutdown (May-October, 2011) of the 12 GeV Upgrade.

† *grames@jlab.org, voutier@lpsc.in2p3.fr*

1 Synopsis

The purpose of this letter is to inform, and seek approval from, the Program Advisory Committee for an experiment we would like to perform during the 6-month shutdown (May-October, 2011) for the 12 GeV Upgrade. The experiment constitutes the Ph.D. Thesis of Jonathan Dumas (LPSC/JLab) and would be the first ever demonstration and measurement for producing polarized positrons using a polarized electron beam. The experiment is proposed to occur in the CEBAF injector using a new dedicated electron beam line and an experimental apparatus successfully applied at the SLAC E166 experiment [1] to demonstrate polarized positrons by an alternative method. The proposed beam energy for the experiment is 3-8 MeV which can be provided by the injector cryounit ($\frac{1}{4}$ cryomodule). The low electron beam current required (1-10 μA) implies a relatively straight-forward and low-power target conversion system and small radiation budget. The positron polarization will be measured by a Compton transmission polarimeter. To perform this experiment during the 6-month shutdown we propose to temporarily segment the lowest MeV energy region of the injector from the remaining CEBAF complex. This configuration and long shutdown provide ample time to install the segmentation, then install, commission and perform the experiment, and finally recover the original injector configuration in advance of restoring the injector for CEBAF operations.

2 Motivation

An efficient scheme for positron production, widely used in particle accelerators, relies on the creation of electron-positron pairs from high energy photons. A significant aspect of the process is the dependence on the polarization, in particular, the circular polarization of the photon transfers to the longitudinal polarization of the positron [2]. This is the basic concept of operation tested for the polarized positron source being developed for the International Linear Collider (ILC). The circularly polarized photons are produced either from the Compton back-scattering of a laser light from high energy electrons [3] or from the synchrotron radiation of very high energy electrons travelling through a helical undulator [1], the latter approach selected for the ILC. This letter of intent proposes an experiment to investigate an alternative scheme based on the polarized bremsstralhung process [4].

Similarly to pair creation, the bremsstrahlung process is a polarization sensitive mechanism. This property has been widely used at un-polarized electron accelerators to produce linearly polarized photon beams. In addition to the intrinsic linear polarization, the photons have a circular component when the incoming electron beam is polarized, such that the bremsstrahlung of polarized electrons most generally lead to elliptically polarized photons [2,5]. This concept is routinely used to obtain a linearly or a circularly polarized photon beam at Hall B [6] at several GeV beam energy.

The production of polarized positrons from polarized bremsstrahlung [7,8] was explored in the ILC context, although not pursued in part because of the requirement of a high intensity polarized electron beam. However, recent advances in high-polarization (85%) and high-current (1 mA) electron sources [9] are encouraging and may offer greater potential for a compact, low energy driver for a polarized positron source [10]. To the best of the authors' knowledge this basic operational concept to transfer the longitudinal polarization of electrons to positrons via polarized bremsstrahlung and subsequent polarized pair-creation has never been experimentally investigated. It is the goal of the present experiment to demonstrate and quantify this concept by measuring the energy distribution of the positron yield and polarization obtained using a highly polarized electron beam of 3-8 MeV.

3 Physics processes

3.1 Polarized bremsstrahlung

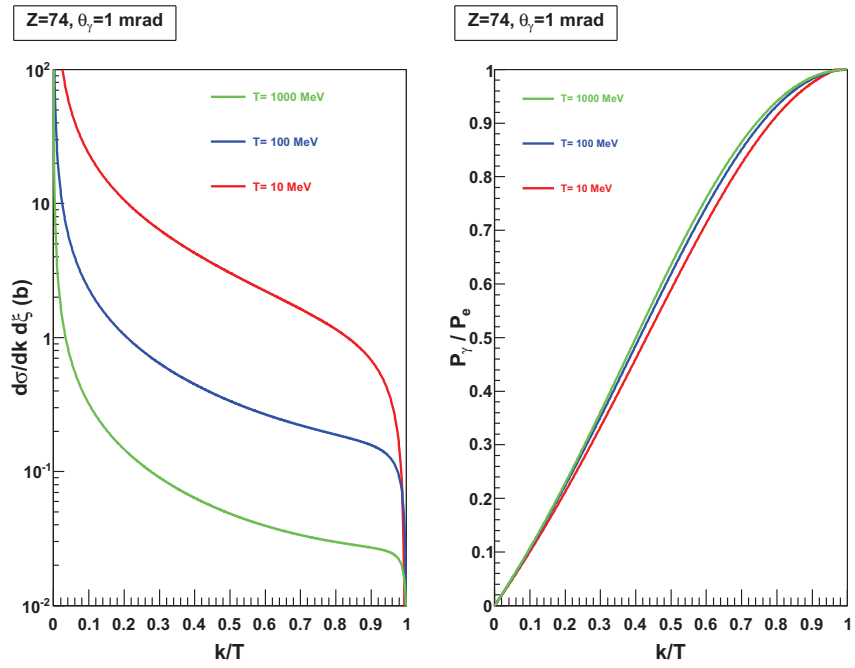

Figure 1. (color) Differential bremsstrahlung cross section ($d\sigma/dkd\xi$) and longitudinal to circular polarization transfer (P_γ/P_e) from electrons (or positrons) to photons with energy (k) expressed as a fraction of the electron beam energy (T), for a tungsten nucleus (Z=74) calculated at a fixed angle θ_γ=1 mrad.

As the essential mechanism for the production of high energy photons, the bremsstrahlung process is a text-book reaction widely investigated theoretically and experimentally. Polarization observables at high energy, including effects of the nuclear field screening and corrections to the Born approximation, were first addressed by H.A. Olsen and L.C. Maximon [2] and are

still today the reference calculations implemented in the GEANT4 simulation package [11]. Fig. 1 shows the energy distribution of the differential cross section and of the polarization transfer from longitudinally polarized electrons to circularly polarized photons, as a function of the photon energy for a tungsten nucleus and a fixed photon angle of 1 mrad . The sharp decrease of the cross section in the end-point region is typical of the bremsstrahlung spectra. The polarization transfer is essentially universal, the highest circular polarization being obtained at the highest photon energy.

3.2 Polarized pair-creation

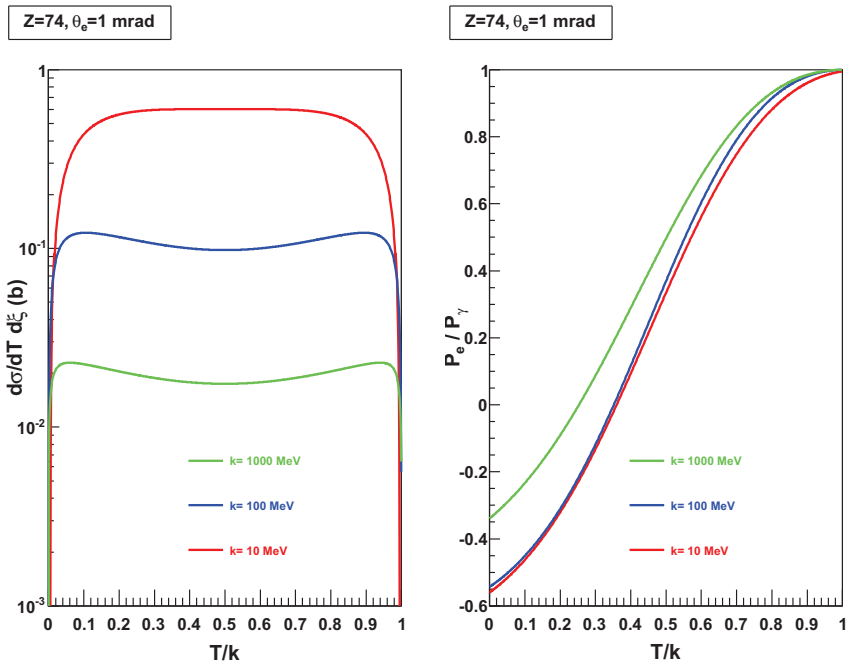

Figure 2. (color) Pair creation differential cross section ($d\sigma/dkd\xi$) and circular to longitudinal polarization transfer (P_e/P_γ) from photons to positrons (or electrons) with energy (T) expressed as a fraction of the photon beam energy (k), for a tungsten nucleus (Z=74) calculated at a fixed angle θ_e=1 mrad.

As the inverse process of the bremsstrahlung reaction, pair production is described by the same matrix elements so that the cross section and polarization transfer relations can be derived from the bremsstralhung expressions following elementary substitutions [2]. Differential cross sections and polarization transfer are shown in Fig. 2 for a tungsten nucleus and a fixed positron angle of 1 mrad, at typical incoming photon energies. The essentially flat distribution is a direct consequence of the production of two identical mass particles from a massless photon. The polarization transfer shows a shape similar to bremsstrahlung but over a larger range of values, allowing for negative and positive polarization transfer.

Fig. 3 shows the expected positron yield and polarization obtained from a GEANT4 simulation using an 8 MeV electron beam and a 1 mm thick tung-

sten target. Angular ($\pm 10^\circ$) and momentum (± 5 %) acceptance cuts, reflecting collection and selection magnets, respectively, have been applied to the simulated yield. It is seen that a 2 pA positron current can be obtained with 30-60% longitudinal polarization. Higher polarizations may be obtained at the expense of reduced positron current. Such a configuration should be easy to achieve and improve upon because of the small energy deposited in the target: the beam current can be increased to 10-30 μA without major impact on the target, and possibly more by using a tilted foil [12]. Such a positron current and polarization can be measured rapidly (minutes) as described in Sec. 6.

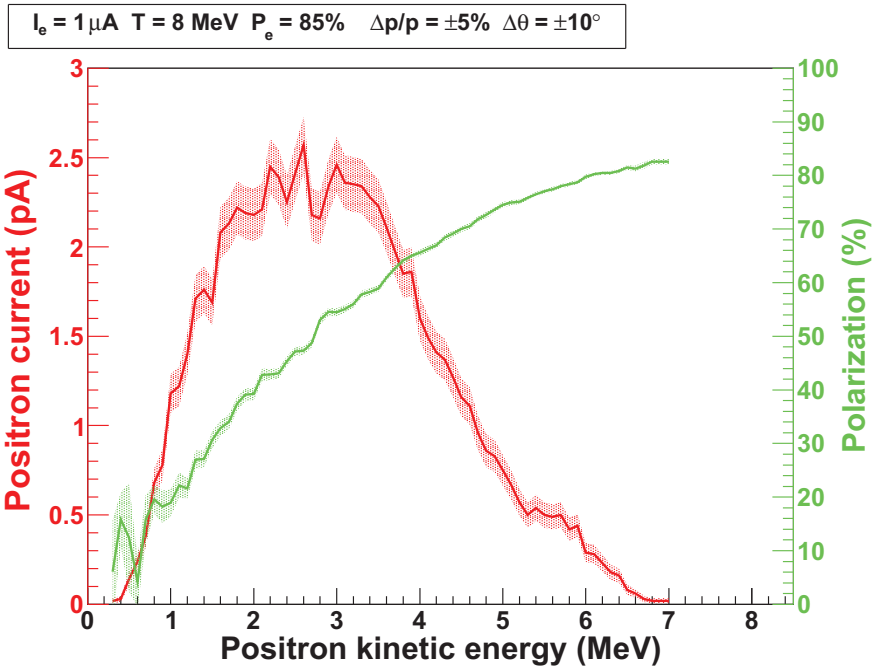

Figure 3. (color) Positron yield and polarization produced from a 1 μA and 85% longitudinally polarized electron beam of 8 MeV striking a 1 mm thick tungsten target.

4 Experiment strategy

The experiment we propose foremost requires a polarized electron beam with energy of at least $\sim$1 MeV to achieve pair creation. While both the CEBAF and FEL accelerators may in principle provide such a beam, reproducing at the FEL the highly spin polarized electron beam, electron spin manipulators and electron polarimeters that exist at CEBAF is costly and impractical. Consequently, we limited ourselves to the CEBAF complex and evaluated how we might accomplish the experiment at locations defined by typical energy ranges: 1-10 MeV (lowest MeV region) [4], 10-60 MeV (injector full energy) [10] and several GeV (linacs or end stations) [13]. While all cases appear viable, our final choice is guided by practical considerations. For example, photoneutron background radiation yield becomes increasingly a distraction above $\sim$8 MeV, *green field* designs are less invasive than modifiying existing beam

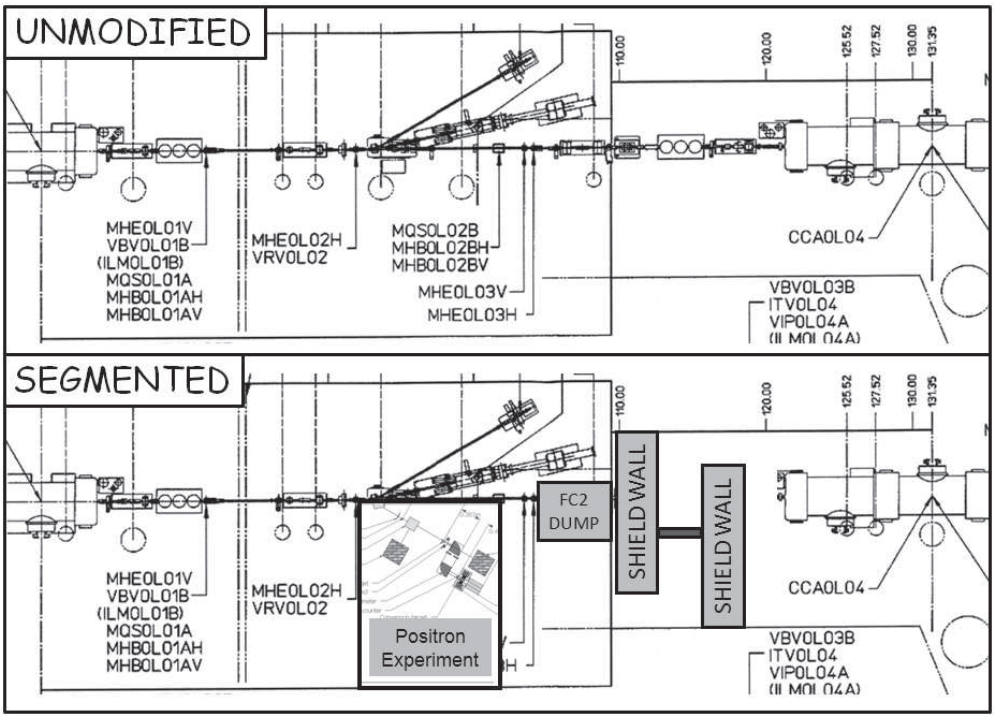

Figure 4. The unmodified (top) and conceptual segmented (bottom) injector layouts are shown together for comparison. In this configuration the segmented injector may operate to deliver a highly polarized (85%) electron beam with energy up to 10 MeV. The beam current may be monitored by both a BCM cavity and a fixed termination Faraday cup (FC2 DUMP) with both operational and hardware limits as routinely used for CEBAF operations.

lines, and the potential availability of experimental equipment (discussed in Sec. 7) significantly reduces cost and overhead. Of all concerns, integration with the CEBAF schedule, dictated by the Nuclear Physics (NP) program, Scheduled Accelerator Down (SAD) periods and the 6-month and 12-month 12 GeV Upgrade shtudowns, is required. Finally, the strategy we propose is to temporarily segment the lowest MeV region of injector following the 10 MeV cryounit from the remainder of the CEBAF complex during the 6-month shutdown May-October, 2011.

Historically, the operation of the electron gun had required for personnel safety purpose that the entire injector and north linac be elevated to a Beam Permit status. However, about 3 years ago an injector segmentation was constructed to allow for operation of the electron gun and warm radio-frequency cavities to accelerate the beam to 500 keV. This was done within constraints set by the Radiological Control (RadCon) and Personnel Safety System (PSS) groups to protect personnel and hardware. This mode has since become routine and proved invaluable for maintenance opportunities and beam operations, particularly while starting the accelerator after a shutdown. The proposed segmentation of the injector for 10 MeV beam energy would offer similar opportunities. In particular the 6-month 12 GeV Upgrade shutdown would provide sufficient opportunity to install, commission and run this experiment. While we may still consider a permanent segmentation, for the purpose of this letter of in-

tent we only request a temporary segmentation, that is, one that would be entirely removed at the end of the shutdown.

The region of the injector intended for segmentation is shown in Fig. 4, where the unmodified (top) and conceptual segmented (bottom) layouts are shown together for comparison. Our plan proposes to reconfigure approximately 5 meters of beam line. All components would be surveyed prior to removal for later re-installation. Two optics girders and one differential pump girder would be removed and stored under vacuum. A fourth girder containing a Faraday cup would move upstream, where installed 10 years ago, to function as a fixed beam dump (rated for 10 MeV and 200 μA); effectively the termination point of the segmented injector. The cleared region would be used to fabricate a temporary shield wall labyrinth consisting primarily of steel shield blocks and re-using the existing PSS personnel gate and egress controls. Downstream of the shield wall the existing cryomodule 0L03 would exist unmodified, never vented. Note the primary entrance of the injector (not shown) provides routine egress and a 2-ton crane/door for moving equipment to the injector. The ultimate configuration would be evaluated by the RadCon and PSS groups and approved by the Director of Operations.

The new electron beam line and experimental apparatus to be installed, occupy a 3×3 m^2 footprint, shown in Fig. 4 and discussed in detail in the next section. The cyrounit, electron spectrometer and electron Mott polarimeter have been previously tested with 2-8 MeV electron beam energy. The proposed experimental collection optics, spectrometer and polarimeter have been previously applied in a comparable energy range [14].

5 Experiment layout

The existing equipment of the injector beam line offer the capabilities of beam energy and polarization measurements, allowing for a precise knowledge of the electron beam. For the production of positrons, a new electron line would be installed on the opposite side of the injector line, with no interference with these beam characterization capabilities. This new line (Fig. 5) would be instrumented with various diagnostic devices and a target ladder supporting a viewer, an empty target, and different production targets.

For example, a 1 μA highly longitudinally polarized electron beam of 3-8 MeV would produce a circularly polarized photon beam within a 1 mm tungsten target (T_1) via polarized bremsstrahlung. The beam power deposited in T_1 has been simulated to be about 4 W, corresponding to half of the total electron beam power. A dipole located after the target would guide the exiting electrons towards a beam dump. At a 1 m distance from the initial production target, the polarized photons would create a longitudinally polarized electron-positron pair in a second tungsten target (T_2), the remaining part of the secondary photon beam being absorbed in an appropriate photon-dump.

Major parts of the characterization equipment of the SLAC E166 experi-

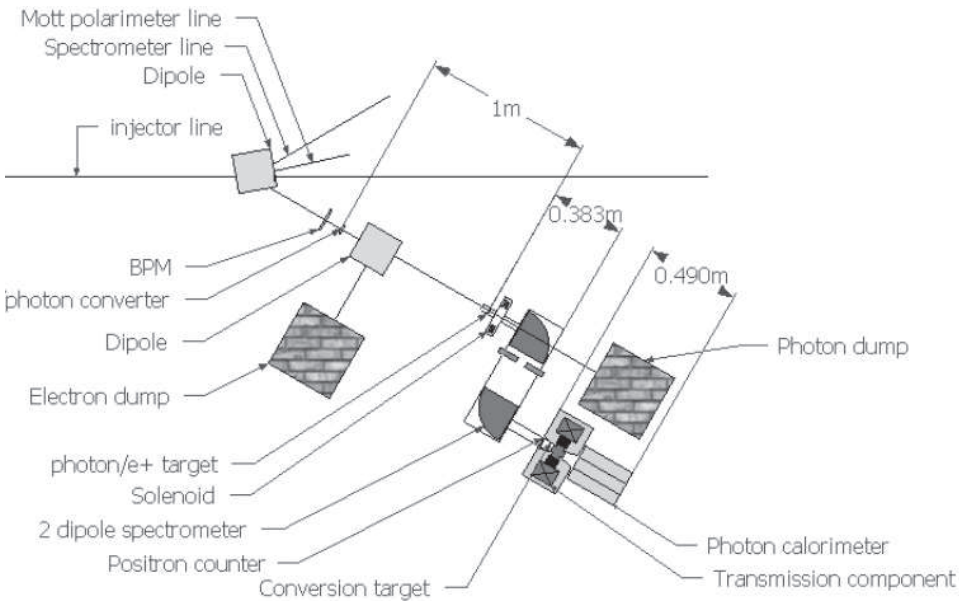

Figure 5. Schematic layout of the experiment.

ment [14] used in a similar energy range would then be installed to measure the positron yield and polarization. A solenoid collects the positrons, a double-dipole spectrometer selects the positron momentum and preserves the longitudinal polarization. In the Compton transmission polarimeter the polarized positrons convert into circularly polarized photons in a third tungsten target (T_3). The Compton absorption of these photons within a polarized iron target is the operationnal principle of the transmission polarimeter: the asymmetry between the number of transmitted photons measured for two opposite target orientations is proportionnal to the positron polarization. In addition, the same experimental asymmetry can also be obtained by reversing the incoming positron polarization (by reversing the electron beam helicity) allowing for the control of systematics. Furthermore, the knowledge of the electron beam polarization from the Mott electron polarimeter allows for a cross calibration of the Compton transmission polarimeter. It is then forseen to firstly commission the new beam line and the Compton transmission polarimeter in electron mode, and secondly perform the positron characterization experiment.

6 Electron and positron polarimetry

6.1 Compton transmission polarimetry

The differential cross section for the Compton scattering of circularly polarized photons (P_γ) from a polarized electron target (P_t) can be written

$$\frac{d^2\sigma}{d\theta d\phi} = \frac{d^2\sigma^0}{d\theta d\phi}\left[1 + P_\gamma P_t A_C(\theta)\right] \quad (1)$$

where $d^2\sigma^0/d\theta d\phi$ is the unpolarized Compton cross section

$$\frac{d^2\sigma^0}{d\theta d\phi} = \frac{1}{2}\left(r_0\,\frac{\omega}{\omega_0}\right)^2\left[\frac{\omega_0}{\omega}+\frac{\omega}{\omega_0}-\sin^2(\theta)\right]\,\sin(\theta) \tag{2}$$

and $A_C(\theta)$ is the analyzing power of the Compton process

$$A_C(\theta) = \left[\frac{\omega_0}{\omega}-\frac{\omega}{\omega_0}\right]\cos(\theta)\Bigg/\left[\frac{\omega_0}{\omega}+\frac{\omega}{\omega_0}-\sin^2(\theta)\right]\;; \tag{3}$$

both quantities depending on the scattered photon energy (ω) and angle (θ), and the incoming photon energy (ω_0).

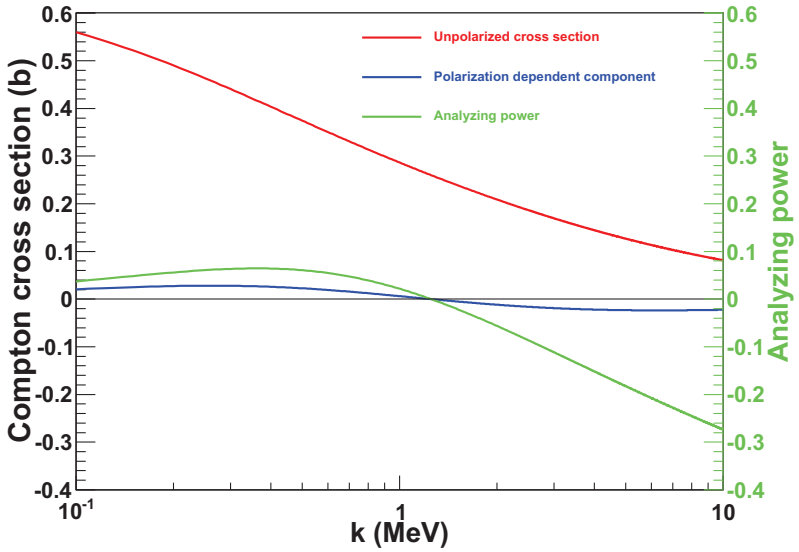

Figure 6. (color) Total Compton cross section components and analyzing power.

Compton transmission polarimetry takes advantage of the sensivity of the Compton process to the absorption of circularly polarized photons in a polarized target. This method, which involves a single detection device matching the size of the incoming beam, is intrinsically easy to implement and has been recently used successfully in experiments similar to the present one [14,15]. Considering the simple case of a monochromatic parallel photon beam scattering off a polarized electron target with length L, the transmission efficiency characterizing the probability that a photon exits the target may be written

$$\varepsilon_T = \exp\left[-(\mu_0 + P_\gamma P_t \mu_1)L\right] \tag{4}$$

which assumes the loss of any photon interacting in the target and the dominance of the Compton process; μ_0 and μ_1 are the unpolarized and polarized Compton absorption coefficients

$$\mu_0 = \rho_e \int d\theta d\phi\,\frac{d^2\sigma^0}{d\theta d\phi}, \qquad \mu_1 = \rho_e \int d\theta d\phi\,\frac{d^2\sigma^0}{d\theta d\phi}A_C(\theta), \tag{5}$$

with ρ_e the electron density of the target. The total unpolarized Compton cross section (μ_0/ρ_e), the polarization dependent part (μ_1/ρ_e) and the Compton analyzing power (μ_1/μ_0) are shown in Fig. 6 as a function of the incoming photon energy. The magnitude of the cross section and of the analyzing power guarantee an efficient polarimeter over the energy range of this experiment. The zero-crossing of the analyzing power at about 1.5 MeV is of particular interest for detector calibration purposes.

The measurement of the circular polarization of the photon beam is obtained from the number of transmitted photons for oppositly polarized target orientations. The corresponding asymmetry is

$$A_T = \frac{N^+ - N^-}{N^+ + N^-} = \tanh(-P_\gamma P_t \mu_1 L) \tag{6}$$

from which the photon circular polarization is inferred according to

$$P_\gamma = -A_T / P_t \mu_1 L \,. \tag{7}$$

The associated statistical uncertainty is

$$\delta P_\gamma = \left[2 N_\gamma \, P_t^2 \, \mu_1^2 L^2 \exp\left(-\mu_0 L\right) \right]^{-1/2} , \tag{8}$$

in the case of small asymmetries. In this discussion a single photon energy is assumed, however, in reality the broad photon spectrum must be considered. The resulting experimental asymmetry is then a convolution of this spectrum with the polarized Compton absorption process. This multistep process has been simulated with GEANT4 taking advantage of improvments to include polarized electron, positron and photon interactions [16].

As an example, consider a 7.5 MeV electron beam of 400 μm width illumintating a 1 mm thick tungsten foil. The created photons travel 12 mm to a polarized analyzing target (iron cylinder 75 mm in length and 50 mm in diameter with a 7.4 % polarization). The photon detector is modeled by a 60×60 mm^2 ideal detection surface located 72.5 mm from the exit of the polarized target. This geometrical arrangement corresponds to the E166 experiment [14]. Fig. 7 shows the number of transmitted photons and the expected asymmetry for a measurement lasting about 100 s with a 1 pA electron beam of 85% longitudinal polarization. For each photon energy bin, the electron beam polarization can be inferred from

$$P_e = \frac{A_T}{P_t A_e} \tag{9}$$

where the electron analyzing power A_e is determined either from simulation or experiment with a known polarized beam, varying from -0.08 to 0.34 in the considered energy range. The statistical average over the accepted photon energy yields the absolute statistical uncertainty ±0.03 on the determination of P_e meaning that an accurate measurement may be obtained within a short amount of time due to the high (150 kHz) event rate.

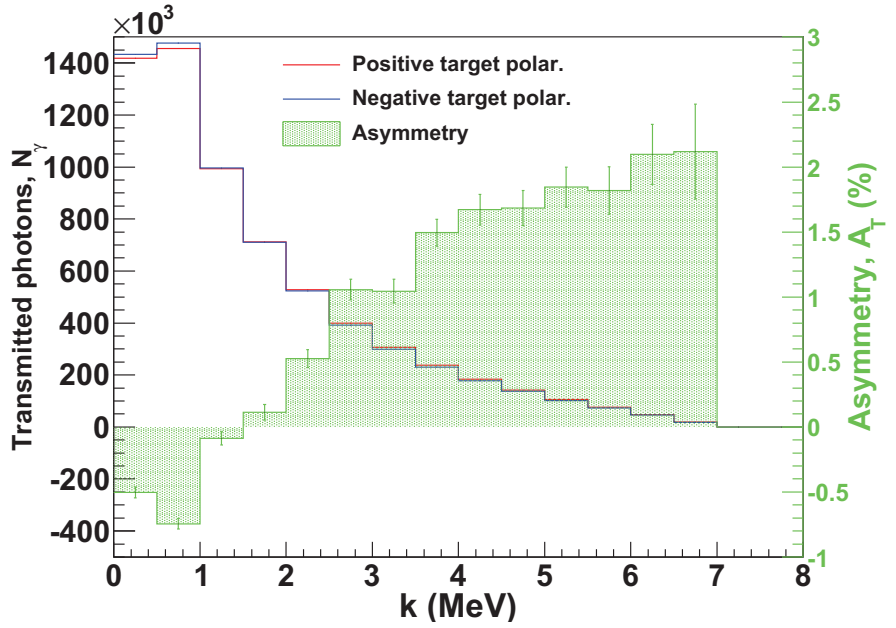

Figure 7. (color) Number of transmitted photons for two opposite target polarizations and expected experimental asymmetry as obtained from GEANT4 simulations. The statistical error bars correspond to a measurement time of 100 s at a 1 pA current.

6.2 Data acquisition

In order to achieve the statistical accuracy in reasonable time, a fast acquisition will be designed for the readout of the photon calorimeter of the Compton transmission polarimeter. Achieving anticipated rates of several hundred kilohertz is possible through the use of Flash Analog to Digitial Converters (Flash ADC), allowing pipe-lining and buffering of the event data. The data acquisition system (DAQ) proposed for this experiment is similar to that presently implemented for the Hall A Compton polarimeter, which demonstrated 100 kHz trigger acquisition already in 1999 [17].

Wireless technology and increased micro-processor speeds with GHz bandwidth have made suitable Flash ADC's both attainable and affordable. The benefit to the DAQ system is that complete pipe-lining of the event data is possible, meaning data is recorded continuously into a large circular memory buffer (access rates from 1.5 μs up to 250 μs). A consequence is the ability to locate events by accessing the memory corresponding to the trigger time thereby eliminating extrinsic dead time as long as events are read before being overwritten by another event. This concept will be the core of the acquisition system of Hall D [20] intended to record and generate the trigger of several thousand calorimeter channels at rates of 160 kHz. Jefferson Laboratory has developed the corresponding Flash ADC with a sampling rate of 250 MHz and is presently commissioning the ADC in the Hall A Moeller DAQ where direct on-board processing of the data using scalers allows for computation of experimental asymmetries and polarization calculations without dead time [18].

As mentioned previously the Hall A Compton polarimeter reached high event rates 10 years ago using a 40 MHz Flash ADC, the state of the art transfer VME protocol available at that time with a speed of 20 MBytes/s, buffering and online histogramming on the VME CPU. A new data acquisition is now being tested in parallel to the *old* DAQ, using a similar 250 MHz Flash ADC to compute the integral of the signal during each helicity period [19]. By using commonly available Field Programmable Gate Arrays (FPGA) one can easily implement integration of the signal or histogramming, completely eliminating the dead time linked to data transfer to the central processor. Depending upon the trigger rate and using new transfer protocols reaching 320 MBytes/s one may also transfer all the events without dead time for offline analysis. It appears reasonable to assert that trigger rates of about 1 MHz are attainable simply by scaling the old DAQ with transfer speeds now 10 times faster. Such performance improvement will soon be confirmed preparing the Hall A Compton DAQ for coming experiments at 6 and 12 GeV in which this system will be fully implemented.

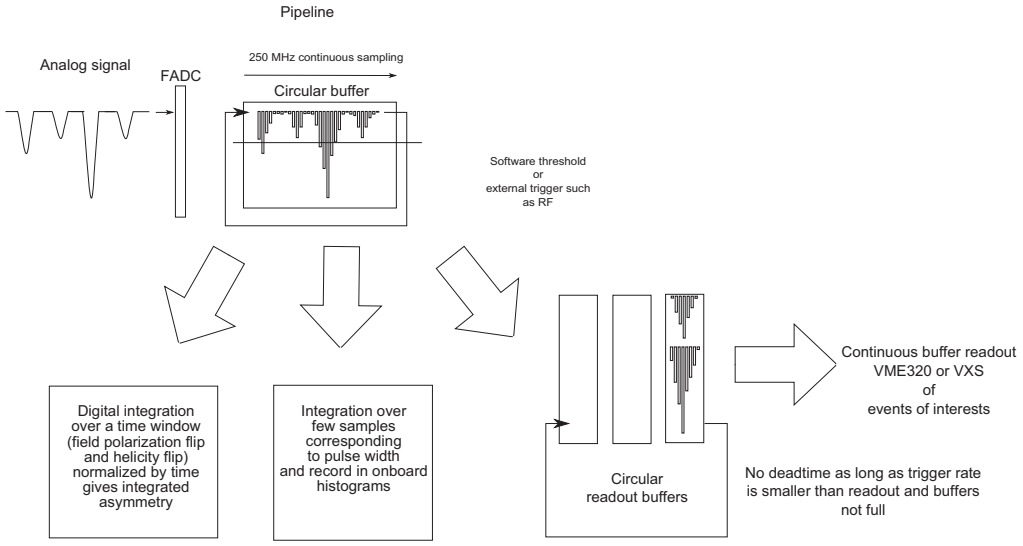

Figure 8. Schematic of the proposed data acquistion system.

As illustrated in Fig. 8, the system will allow several methods of measurement. First, as an integration measurement it has the advantage of being free of threshold effects, insensitive to pile-up and will work at any rate at the expense of energy information. Second, implemented for online histogramming it is also free of dead time and provides the energy dependence of the asymmetry at any rate, although the systematics due to pile up and thresholds must be studied to determine the optimal balance between statistical uncertainty and systematic error. This method should also be able to reach a 1 MHz event rate. Finally, event by event readout provides the greatest quantity of information without dead time provided events are read faster than written. For example, to record 20 samples for each event and transfer 200 MByte/s naively requires a rate of 1 MHz. The challenge is the large amount of data generated, so it may prove more practical to implement this third method with a pre-scaler for systematic studies. Practically, an operational system could be developed in about 6 months taking advantage of existing projects, for example, the Hall A Compton and Moller polarimeter DAQ upgrades and

Hall D is already commissioning a comparable system. The final system will operate simultaneously the three data acquisition methods.

7 Timeline

We propose a 2 year plan to perform this proof-of-principle experiment, complete the Ph.D. Thesis of Jonathan Dumas and publish our results. The following timeline outlines a plan we believe will allow us to successfully perform this experiment.

December, 2009

- Following the 2nd year Ph.D. Thesis Review of Jonthan Dumas we received support by the Accelerator Division Associate Director to proceed and submit a Letter of Intent to PAC35 for this proposed experiment at CEBAF.

January - February, 2010 (Scheduled Accelerator Down)

- Collaborators seek PAC approval so that we may have official support of JLab, and to develop a Memorandum of Understanding (MOU) with DESY (Compton transmission polarimeter) and Princeton University (collection solenoid and spectrometer) to loan hardware for this experiment.
- Survey and assess region for positron experiment and segmentation.

March - June, 2010 (Nuclear Physics Program)

- LPSC to loan Compton transmission polarimeter from DESY, acquire analyzing magnet power supply, develop data acquisition system, test photon calorimeter, integrate systems.
- JLab to loan solenoid and spectrometer from Princeton University, acquire magnet power supplies, make functional, map and/or develop magnetic model for simulation.
- Develop detailed layout to add new electron beam line to injector at 0L02 (lowest MeV) region, with suitable optics and diagnostics to deliver/control beam at conversion target. Fabricate and acquire components for new beam line "spigot".

July - August, 2010 (Scheduled Accelerator Down)

- Early opportunity to install new beam line "spigot": new vacuum chamber and isolation valve.
- Perform final measurements to prepare for the injector segmentation.

September 2010 April 2011 (Nuclear Physics Program)

- Complete integrated design of the experiment with full simulations, scattering chamber, targets, collection optics, dumps, detectors and shielding.
- Fabricate and test beam line components.
- Fabricate injector segmentation.

- Transfer Compton transmission polarimeter from LPSC to JLab.
- Prepare for experiment installation.

May - October 2011 (Perform Experiment)

- 1 month to install segmentation, experimental apparatus and commission segmentation.
- 3 months to commission and perform experiment.
- 1 month to un-install segmentation, remove and return experimental apparatus to DESY and Princeton University.
- 1 month advance recovery in preparation of CEBAF operations.

November - December 2011 (Nuclear Physics Program)

- Experiment and analysis are completed.
- Jonathan Dumas to defend Ph.D. Thesis and publish results.

8 Summary

This letter proposes an experiment at the CEBAF injector to demonstrate and measure the longitudinal polarization transfer from a highly spin polarized electron beam to positrons via the polarized bremsstrahlung and subsequent pair-creation processes in radiator and pair production targets, respectively. It requires a new dedicated injector beam line and experimental apparatus. A strategy which implies the segmentation of the MeV region of the injector from the remaining CEBAF complex has been proposed to perform this experiment during the 6-month shutdown (May-October, 2011) of the 12 GeV Upgrade.

This experiment is designed to have a small physical and radiation footprint. By using a 1-10 μA electron beam low power targets and minimal shielding is intended. The positron (and electron beam) polarization will be measured via the Compton transmission method. The expected positron yield is low $\sim$pA but yet demanding in terms of data acquisition performances. We should benefit from the current developments for Hall A and Hall D to guarantee a powerfull operation of this device.

In addition to this unique *proof-of-principle* experiment, this represents the first accelerator physics experiment at Jefferson Lab aimed at a production mechanism for positrons in the CEBAF accelerator. This R&D issue has been discussed for many years and through two workshops, most recently at the International Workshop on Positrons at Jefferson Lab in March, 2009 [21]. The results of this experiment would provide valuable information for the potential development of a higher intensity polarized positron source for CEBAF, and may prove useful for opportunities in the context of the ILC.

References

[1] G. Alexander *et al*, Phys. Rev. Lett. **100** (2008) 210801.

[2] H.A. Olsen, L.C. Maximon, *Phys. Rev.* **114** (1959) 887.

[3] T. Omori *et al*, Phys. Rev. Lett. **96** (2006) 114801.

[4] J. Dumas, J. Grames, E. Voutier, *AIP Conf. Proc.* **1149** (2009) 1184.

[5] W.H. McMaster, *Rev. Mod. Phys* **33** (1961) 8.

[6] B.A. Mecking *et al.*, *Nucl. Inst. Meth.* **A 503** (2003) 513.

[7] E.G. Bessonov, A.A. Mikhailichenko, *Proc. of the* V^{th} *European Particle Accelerator Conference*, Barcelona (Spain), June 10-14, 1996.

[8] A.P. Potylitsin, *Nucl. Inst. Meth.* **A 398** (1997) 395.

[9] J. Grames *et al.*, *Proc. of the 2007 Particle Accelerator Conference*, Albuquerque (New Mexico, USA), June 25-29, 2007.

[10] J. Dumas, J. Grames, E. Voutier, *AIP Conf. Proc.* **1160** (2009) 120.

[11] S. Agostinelli *et al*, Nucl. Inst. Meth. **A 506** (2003) 250.

[12] P. Perez, A. Rosowsky, *Nucl. Inst. Meth.* **532** (2004) 523

[13] A.P. Freyberger, *AIP Conf. Proc.* **1160** (2009) 101.

[14] G. Alexander *et al*, Nucl. Inst. Meth. **A 610** (2009) 451.

[15] M. Fukuda *et al*, Phys. Rev. Lett. **91** (2003) 164801.

[16] R. Dollan, K. Laihem, A. Schälicke, Nucl. Inst. Meth. **A 559** (2006) 185

[17] http://hallaweb.jlab.org/compton/Documentation/Technical/1997/note.perf.acq.dg.ps.gz

[18] http://hallaweb.jlab.org/parity/prex/mollfadc.pdf

[19] http://hallaweb.jlab.org/ rom/fadcspec.pdf

[20] http://www.jlab.org/Hall-D/daq_wfest/daq_wfest.ps

[21] Proceedings of the International Workshop on Positron at Jefferson Lab, Edts. L. Elouadrhiri, T.A. Forest, J. Grames, W. Melnitchouk, and E. Voutier, *AIP Conf. Proc.* **1160** (2009).

Titre :

Etudes de faisabilité d'une source polarisée de positrons basée sur le rayonnement de freinage d'électrons polarisés

Résumé

Les communautés de la physique nucléaire et des hautes énergies ont montré un intérêt croissant pour les faisceaux de positrons intenses et hautement polarisés. Des photons polarisés durs peuvent produire des positrons dans le champ atomique par création de paire, l'électron et le positron ainsi produits portent une partie de la polarisation de la particule initiale. Les récentes avancées dans le domaine des sources d'électrons à courants intenses (1 mA) et hautement polarisés au Jefferson Lab offrent la perspective de créer des positrons polarisés à partir d'électrons de faible énergie. Cette thèse se propose de discuter les transferts de polarisation aux positrons dans la perspective d'une optimisation du design d'une source de positron polarisée. L'expérience PEPPo, visant à mesurer la polarisation de positrons par un faisceau d'électrons de basse énergie ($<$10MeV) mais de basse intensité est discutée. Une démonstration concluante de cette technique fournirait une méthode alternative de produire des positrons polarisés de basse énergie et des informations utiles pour optimiser le design d'une source dans la gamme d'énergie inférieure au GeV.

Mots-clefs : Polarisation...

Title:

Feasability studies of a polarized positron source based on the bremsstrahlung of polarized electrons

Abstract

The nuclear and high-energy physics communities have shown a growing interest in the availability of high current, highly-polarized positron beams. A sufficiently energetic polarized photon or lepton incident on a target may generate, via bremsstrahlung and pair creation within a solid target foil, electron-positron pairs that should carry some fraction of the initial polarization. Recent advances in high current ($>$ 1 mA) spin polarized electron sources at Jefferson Lab offer the perspective of creating polarized positrons from a low energy electron beam. This thesis discusses polarization transfer from electrons to positrons in the perspective of the design optimization of a polarized positron source. The PEPPo experiment, aiming at a measurement of the positron polarization from a low energy ($<$ 10 MeV) highly spin polarized electron beam is discussed. A successful demonstration of this technique would provide an alternative scheme for the production of low energy polarized positrons and useful information for the optimization of the design of polarized positron sources in the sub-GeV energy range.

Keywords: Polarization...